Authorization

In presenting this thesis in partial fulfillment of the requirements for an advanced degree at Idaho State University, I agree that the Library shall make it freely available for inspection. I further state that permission for extensive copying of my thesis for scholarly purposes may be granted by the Dean of the Graduate School, Dean of my academic division, or by the University Librarian. It is understood that any copying or publication of this thesis for financial gain shall not be allowed without my written permission.

Signature ______________________

Date __________________________

A Novel Submerged Oscillating Water Column (SOWC) Energy Harvester

by

Mohammadamin Torabi

A dissertation

submitted in partial fulfillment

of the requirements for the degree of

Doctor of Philosophy in the Department of Civil and Environmental Engineering

Idaho State University

Spring 2021

Committee Approval

To the Graduate Faculty:

The members of the committee appointed to examine the thesis of Mohammadamin Torabi find it satisfactory and recommend that it be accepted.

Bruce Savage, Ph.D., P.E., Professor and Chair
Major Adviser

Marco P. Schoen, PhD, P.E., Professor
Graduate Faculty Representative

James Mahar, Ph.D., LPG, PG- Senior lecturer
Committee Member

Chikashi Sato, Ph.D., P.E., Professor
Committee Member

Mustafa Mashal, Ph.D., P.E., Associate Professor
Committee Member

Thomas Baldwin, Ph.D. - Visiting Professor
Committee Member

THIS DISSERTATION IS DEDICATED TO MY DEAR FAMILY IN IRAN

Acknowledgments

I would first like to express the deepest appreciation to my Advisor, committee chair, Professor Bruce Savage, whose expertise was invaluable in formulating the research questions and methodology. Your insightful feedback pushed me to sharpen my thinking and brought my work to a higher level. Many thanks to the Department of Civil and Environmental Engineering at Idaho State University for providing me with limitless opportunities to pursue my areas of interest.

I also would like to thank the support and help given by my committee members, each of whom has provided patient advice and guidance throughout the research process and proposal defense and a special thanks to Dr. Thomas Baldwin for his professional helps and support in running the servo motor. I express my deepest and most heartfelt appreciation to my dear parents and siblings for their support, words of encouragement, motivation, and love from afar.

Table of Contents

LIST OF FIGURES

LIST OF TABLES

LIST OF SYMBOLS

h	Height of cylinder
H	Wave height
H_{inside}	Oscillation inside the cylinder
d	Water depth
d_1	Driving depth
D	Diameter
T	Wave period
L	Wave length
ϕ	Velocity Potential
k	Wave number
σ	Wave angular frequency
η	Water surface profile
w	Water particle velocity in vertical direction
u	Water particle velocity in horizontal direction
a_x	Water particle acceleration in x direction
a_z	Water particle acceleration in y direction
ε	Vertical components of the particle position
ζ	Horizontal components of the particle position
e	Conversion rate
p	Pressure
P_w	Wave power

C	Damping coefficient
C0	Damping coefficient at the start side of the sponge layer
C1	Damping coefficient at the end side of the sponge layer
S	The distance in downstream direction of the sponge layer
U_e	The conversion rate error
U_d	The error of depth measurements
U_T	The error of wave period measurements
U_{Cr}	The error of conversion rate
d_r	Relative depth error
f	Friction factor

A Novel Submerged Oscillating Water Column (SOWC) Energy Harvester

Dissertation Abstract — Idaho State University (2021)

Wave energy converters (WEC) are hydraulic structures that are used to harvest energy from oceans. Different types of WECs technology were reviewed and presented. The weakness of many of the technologies include low efficiency, ocean view aesthetics, and durability in severe weather. This research proposes a new concept of a WEC termed a Submerged Oscillating Water Column (SOWC) that may address the last two issues. The SOWC device consists of two submerged chambers that are connected to allow airflow between the chambers as waves pass; ideally spaced at half a wavelength. As waves move over the SOWCs, the pressure fluctuates and the water level inside the chambers oscillates. By using a power take-off system, motion energy can be transformed into electrical energy. The device maybe capable of connecting and syncing multiple of them together and creating an energy harvesting farm. Numerical simulations using the Computational Fluid Dynamics (CFD) code Flow-3D and physical model tests were carried out at Idaho State University to assess the validity and conversion rate of the proposed device. Thirty-seven numerical tests and eighty-four experimental tests were carried out and compared. The key component of this study is to determine the conversion rate; the ratio of the water fluctuation inside the cylinder relative to the wave oscillations. The efficiency of the whole system and the detail of the power take-off system (PTO) is not in the scope of this research. Numerical and experimental tests are compared. The results showed the conversion rate in the range of 30%-95%. The key factors in conversion rates were the wave characteristics including height, depth, and period. Other important variables include the location of the SOWCs' openings.

Keywords: Submerged oscillating water column (SOWC), wave tank, wave energy

CHAPTER 1. INTRODUCTION

The oceans are one of the largest but least discovered renewable energy sources on earth. Oceans are a potential great source of naturally renewable and reliable energy around the world. Different strategies are employed to harvest that energy. The main sources of ocean energy are:

- Tidal streams
- Ocean currents
- Tidal range (rise and fall)
- Waves
- Ocean thermal energy
- Salinity gradients

Ocean energy offers several significant advantages over other sources of renewable energy. Unlike wind and solar, ocean currents and waves are predictable, reliable and more promising (Lewis et al. 2015). The endless flows and waves crash into our shoreline and create a reliable source for future energy. On the other hand, moving water is 832 times denser than moving air, and it can lead to a more efficient harvesting system.

Minimal use of land and less visual pollution can be another significant advantage of ocean energy devices. In many regions, land is a scarce and valuable resource. Other renewable sources of energy such as wind and solar require a huge farm to harvest energy. However, subsea ocean energy technologies such as the proposed device in this dissertation are hidden under the water, out of sight and do not compete for land space.

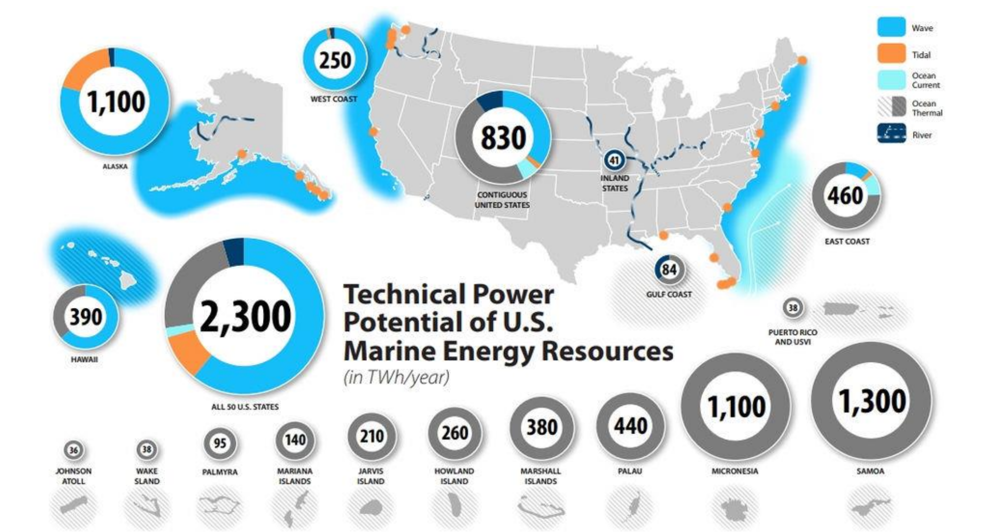

Figure 1:Technical power potential of U.S. marine energy resources (Kilcher et al. 2021)

The National Renewable Energy Laboratory (NREL) reports that the amounts of total potential marine energy resources in the 50 states are 2,300 TWh/yr which is equivalent to approximately 57% of U.S. generation in 2019 (Kilcher et al, 2021) (Figure 1). However, only a small fraction of this is obtainable at the moment and it depends much on future technology developments. The International Energy Agency has projected that in 2040, ocean energy, and not just wave energy, will contribute 51-144 TWh, which is less than 0.4% of the overall production of electricity (Ulvgard, 2017). So, there is still a long path to go.

Although a significant amount of research projects have been done on wave energy converters in past decades, there is still no consensus on the best and most efficient device, not even in theory. There are some advantages and disadvantages for every device that need to be considered based on needs. Maintenance cost, survivability in different sea states (like storms) concerning lifetime, and obtaining maximum energy per unit cost are the ultimate goal of each project. On every wave energy converter project, the first piece of the puzzle is the characteristic of the target location.

In oceans, the direction of the waves, peak wave period and wave height can be obtained by statistical methods. The results are usually shown with a wave rose diagram. The wave rose diagram indicates the probability of different waves in every direction. It also indicates the probability of different wave heights and wave periods. An example of a wave rose diagram with significant wave heights and peak wave periods is shown in Figure 2.

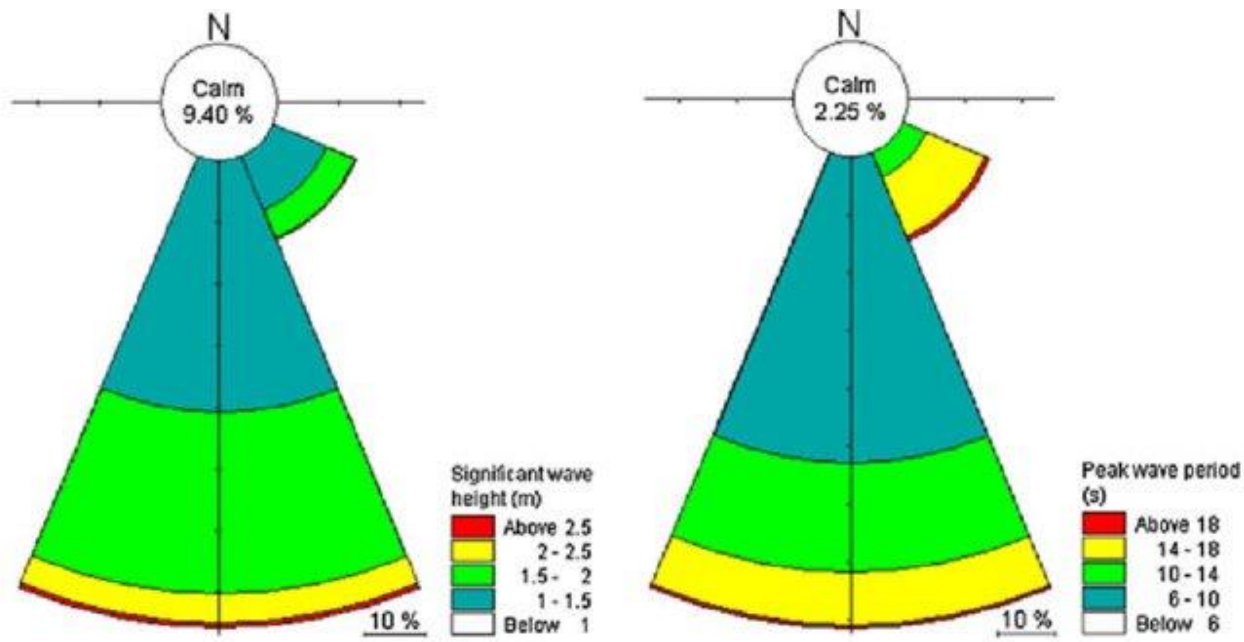

Figure 2: An example of wave rose diagram with significant wave heights and peak wave periods

This dissertation proposes a new concept for a wave energy convertor device, consisting of two submerged cylinders connected with a pipe. The concept is inspired by pressure differential energy converters and point absorber devices, considering the simplicity and linkability. Figure 3 shows a schematic sketch with key parts labeled. As it can be observed, an air pocket is entrapped in cylinders. The cylinders are placed half a wavelength in the direction of waves. Although waves direction can vary, usually 70-80% of the time waves are in a given direction. As waves pass over the device, an air pocket starts to travel back and forth between cylinders. The float in each cylinder which separates the air and water, oscillates by same frequency of waves. The floats are connected to a dual pump and from its oscillation the pump can send water in a high-pressure transmission line to a turbine. The advantages of the proposed device over other devices are being close to the shore which ease the maintenance, can be constructed using inexpensive material, the ability to sync the cylinders together and no visual pollution. The details of the device are explained more in detail in “Chapter 3: Conceptual proposed device”. To test the proposed concept, numerical modeling and experimental tests have been carried out at Idaho State University.

Deploying and testing the full scale of the proposed device and generating the energy, requires more than a concept for converting ocean waves to electricity. Due to lack of resources, the power takes off system is not studied in this research. This dissertation addressed the feasibility of the concept, the conversion rate of the cylinders and the methods to achieve the maximum conversion rate of the device. Conversion rate is defined as the ratio of water level oscillation amplitude inside the cylinder to wave height.

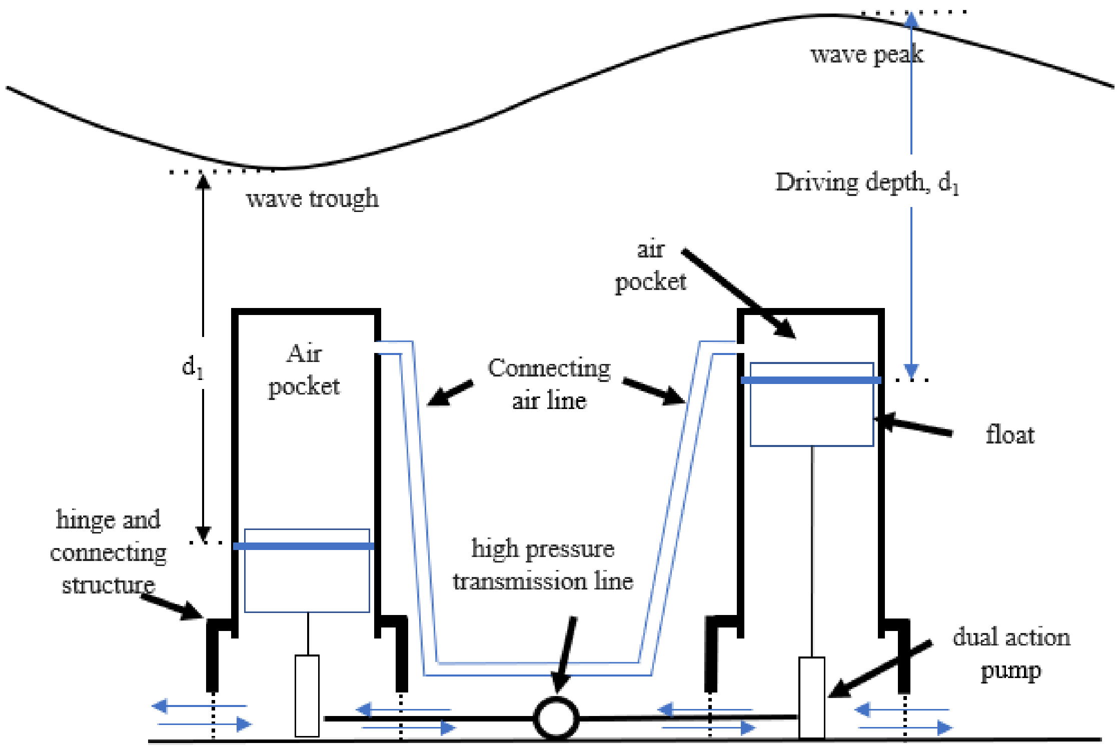

Figure 3: Schematic proposed new wave energy harvester

1.1 Research Statement, Goals and Methodology

This dissertation proposed a new wave energy harvester device that can capture energy nearshore. To prove the concept, seventeen different numerical simulations were completed by varying the cylinder height, h; water depth, d; cylinder diameter, D; and wave period, T. An additional 27 simulations were designed to improve the conversion rate by changing the SOWC opening dimensions and geometry. In addition, 84 experimental tests for three pairs of cylinders were carried out at the ISU Physical Science lab. Different cylinders with different diameters were used to evaluate the effect of size on the conversion rate. For a given diameter and constant water depth, four to five different wave periods were generated and the data for each wave period were recorded. After that, water depth was increased and the same tests were repeated. This process continued for each cylinder diameter. At the end, the numerical and experimental tests were compared. A summary of the numerical and experimental test matrix is shown in Table 1. The numerical and experimental test setup was identical to Figure 4. The effect of different materials making up the cylinder has not been studied; however, a variety of materials could be used.

Table 1: Summary of numerical and experimental tests matrix

Numerical		Experimental	
Variables	**Range (cm)**	**Variables**	**Range (cm)**
Cylinder height, h	61, 91.4	Cylinder height, h	20.32
Water depth, d	120-244	Water depth, d	24.5-31.5
Cylinder diameter, D	15.2	Diameter, D	5.08, 7.62, 10.16
Wave period, T	1.75-3 (sec)	Wave period, T	1-2.5 (sec)
# of cylinder openings	5	Wave length, L	120- 360
Total # tests	**44**	**Total # tests**	**84**

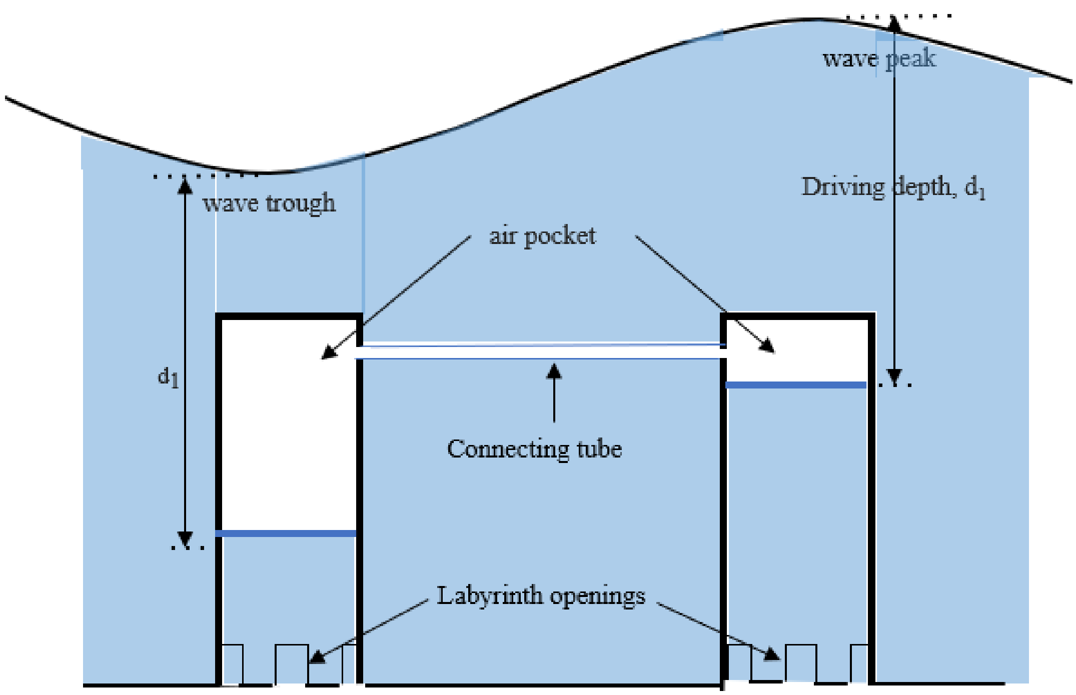

Figure 4: Proposed new wave energy device

This dissertation addresses the following points:

1- The feasibility of the proposed device.
2- The conversion rate of the system before connecting to a Power Take Off (PTO) system.
3- Improving the conversion rate and maximum achievable efficiency.
4- The best location for the device.

Although the dissertation is separated to answer the above points which seem detached, the whole purpose is getting one step closer to enabling Wave Energy Converter (WEC) operation. Building a WEC prototype is a multidisciplinary task that requires detailed technical knowledge. This dissertation tries to cover important pieces of this puzzle, with a focus on the behavior of the WEC in different depth and measuring water oscillation inside the cylinders.

Regarding the first point, numerical and experimental tests have been designed to see the possibility of water oscillation inside the cylinders. However, the motion depends on ocean waves, WEC size and damping behavior of the PTO. To predict the behavior, different models with different openings and sizes are used to represent the WEC. The methodology of testing and improving the prediction of the device is to measure the amplitude of water oscillation inside the cylinders and compare it to the amplitude of incident waves.

The efficiency of the WEC device is including the efficiency of the power take-off (PTO) system and conversion rate. In another word, conversion rate is the ratio of water oscillation inside the cylinder over the wave height. This research tries to come up with a relation for conversion rate and methods for maximizing this efficiency which covers the second and third points.

Regarding the last point, the lessons learned from this research were used to suggest a general location for placing and using the WEC device, considering the ease of maintenance, accessibility and highest conversion rate. The location needs to satisfy all these requirements. The results of this research ended up with two papers and a provisional patent.

1.2 Research Outlines

The dissertation is structured in three separate sections including a literature review and history of WECs, numerical modeling and experimental modeling. The literature review and history chapter provide the theory of waves and introduction to all other WEC devices. Numerical and experimental chapters (Chapter 4 and Chapter 5) gather the affiliated method and results. In continue, Chapter 6 brings the results and discussion on numerical and experimental tests and compare them. Finally, a summary of all works done are brought in Chapter 7.

CHAPTER 2. BACKGROUND

This chapter reviews the research and development accomplished on wave energy converter devices. It starts with an overview of wave generation, the theory of waves and the classification of waves. The chapter continues by identifying different types of wave energy converter devices and outlines the research on different converter types.

2.1 Wave Generation

Waves can be generated for a variety of reasons, including winds, earthquakes, tides, boats, etc. The most common waves are the surface waves generated by winds. Surface waves are created by the friction between wind and water surfaces. As the wind continuously blows over the surface of the ocean or a lake, the continual disturbance creates a wave crest. Waves created by winds are an example of surface gravity waves.

Surface gravity waves are created when the surface of a column of water is vertically disturbed or raised and gravity pulls to return the water surface to the equilibrium position. The inertia of the body of water with gravity as a body force cause oscillation, which disturbs the adjacent water surfaces and propagates waves. As a wave propagates, because of the interaction of gravity and mass inertial force of the column of water, the oscillatory motion in the wave continues. Generated waves have different periods and heights. Waves in stormy oceans typically look unorganized and chaotic. Wave characteristics include frequency, period, wavelength, amplitude, etc. These characteristics can be determined by three factors in a wind-induced wave creation event. The fetch, the strength of the wind, and the duration that the wind blows are the three factors. The distance that the wind blows without a change in direction or duration is called fetch. The wind velocity and duration can potentially limit the created wave characteristics. If all three of these factors are satisfied, waves reach maximum height limitation before breaking. This nature is described as “fully developed” (Jarocki and Wilson, 2010).

Irregular waves in a fully developed sea generated by wind are composed of multiple regular waves having different heights and periods. Figure 5 and Figure 6 show how the irregular waves consist of different regular waves.

Figure 5: Irregular sea state (Jarocki and Wilson, 2010)

Holmes in the manual for wave simulation state that:

> “The seaway is the superposition of a large number of sinusoidal waves of variable period, amplitude, direction and phase, as shown in Figure 6. Theoretically these wave

parameters can all vary randomly to each other but in practice the amplitudes in the irregular signal are found to have a Gaussian distribution."

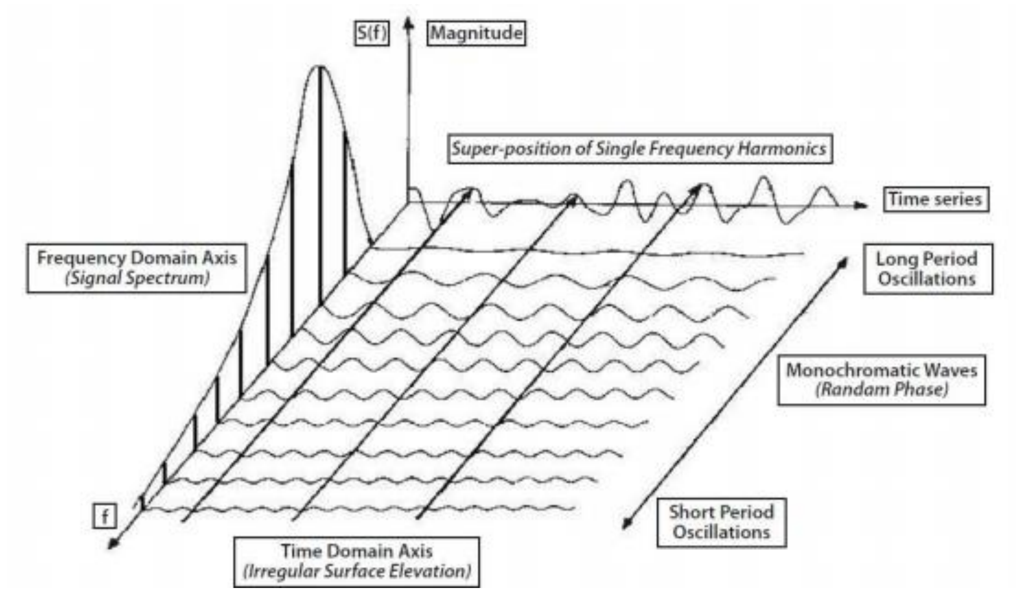

Figure 6: Super-position of sine waves to generate an irregular signal, (Holmes, B., 2015).

The simplest theory to define waves is the two-dimensional small-amplitude or linear wave theory. The equations in this theory provide most of the kinematic and dynamic properties of the surface gravity waves and predict wave behavior for most circumstances.

2.1.1 Small-Amplitude Wave Theory

Small-amplitude wave theory is developed by linearizing the equations that define the free surface boundary conditions. This theory was initially defined for two-dimensional, freely propagating and linear periodic waves. Considering all these and the boundary conditions, a velocity potential (ϕ) is sought to satisfy the requirement for irrotational flow. The velocity potential is required to define various wave characteristics (e.g., surface profile, pressure field, particle velocities). However, the velocity potential is not valid at the bottom and thin boundary layers at the air-water interface. The assumptions for this theory are (Sorensen, 2005):

- The water is homogeneous and incompressible and surface tension is negligible
- Flow is irrotational so there is not any shear stress at the boundaries. (air-sea interface and bottom)
- The velocity potential ϕ must satisfy the Laplace equation shown as Eqn (1).

$$\frac{\partial^2 \phi}{\partial x^2} + \frac{\partial^2 \phi}{\partial z^2} = 0 \tag{1}$$

where x and z are the horizontal and vertical coordinates, respectively.

- The bottom is stationary horizontal, impermeable and is not adding or removing energy from the flow.
- The air pressure is constant at the interface.
- Small wave height compared to the wavelength and water depth. Because particle velocities are proportional to wave height and wave celerity (L/T) is related to the wavelength and water depth, small wave height means particle velocities be smaller than wave celerity.

The parameters and sine wave terminologies are shown in Figure 7. Figure 8 shows a wave traveling at a wave celerity C in the x direction. The x-axis is still water level and the z-axis is opposite of the gravity direction, so z=-d shows the bottom and z=η indicate the wave surface. In defining waves, some useful dimensionless parameters can be defined as follows:

wave number (k)	$k = 2\pi / L$	(2)
wave angular frequency(σ)	$\sigma = 2\pi / T$	(3)
wave steepness	H/L	(4)
relative depth	d/L	(5)

Where H is wave height, L is the wavelength, d is water depth and T is wave period.

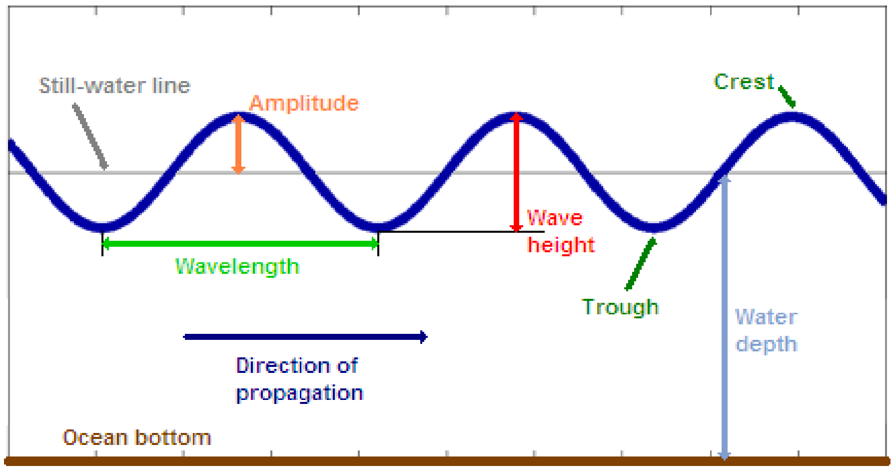

Figure 7: Sine wave terminology (Jarocki and Wilson, 2010)

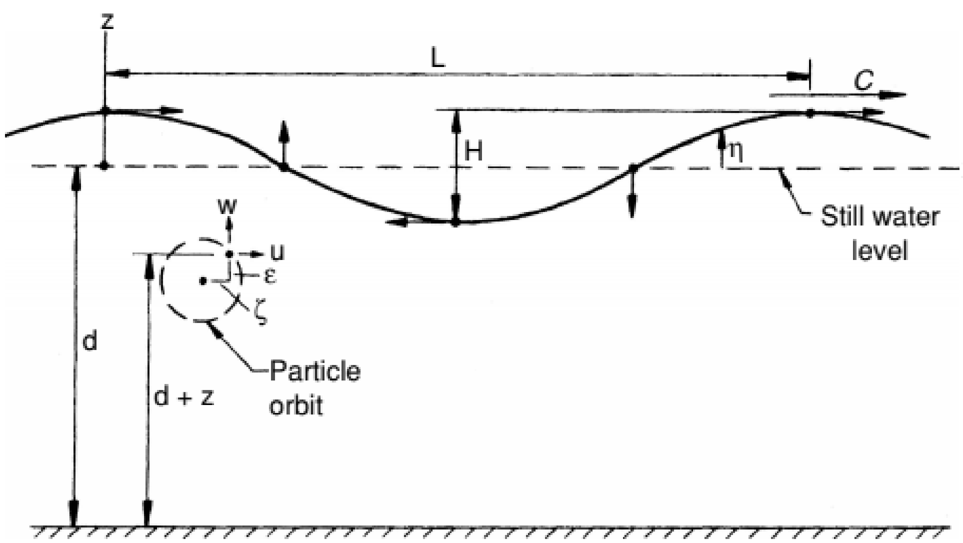

Figure 8: Water particle movements (Sorensen, 2005)

By developing the velocity potential equation (Eqn 1) and considering the boundary conditions, the following equations can be obtained. There are two boundary conditions for the bottom and top. The boundary condition for the bottom (BBC) is free-slip with no perpendicular velocity (Eqn 6). At the free surface, a kinematic surface boundary condition (KSBC) is considered (Eqn 7). Finally, the Bernoulli equation for an unsteady irrotational flow (Eqn 8) must be considered to find the velocity potential (Eqn 9):

$$w = \frac{\partial \phi}{\partial z} = 0 \quad at \quad z = -d \tag{6}$$

$$w = \frac{\partial \eta}{\partial t} + u\frac{\partial \eta}{\partial x} \quad at \quad z = \eta \tag{7}$$

$$\frac{1}{2}\left(u^2 + w^2\right) + \frac{p}{\rho} + gz + \frac{\partial \phi}{\partial t} = 0 \tag{8}$$

$$\phi = \frac{gH}{2\sigma}\frac{\cosh k\left(d+z\right)}{\cosh kd}\sin\left(kx - \sigma t\right) \tag{9}$$

Where g is the gravity, P is pressure and ρ is the water density. The pressure at the surface water is zero and the term P/ρ in equation ((8) can be eliminated. By inserting the velocity potential into this equation and equation (7), wave surface profile can be obtained as equation (10) (Sorensen, 2005):

$$\eta = \frac{H}{2}\cos\left(kx - \sigma t\right) \tag{10}$$

And wavelength would be:

$$L = \frac{gT^2}{2\pi}\tanh\frac{2\pi d}{L} \tag{11}$$

2.1.2 Wave Classification

The waves can be classified based on the ratio of water depth over wavelength which is called relative depth (d/L). The relative depth can define whether the desired place is located in deep water, shallow water, or transitional. Figure 9 shows the relative depth. Deep water can be interpreted as d/L>0.5, shallow water as d/L<0.05 and transitional is between these two numbers. By propagating a wave from deep water to shallow water the wavelength decreases.

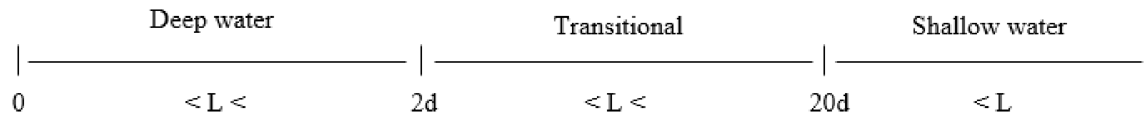

Figure 9: Water depth classification

2.1.3 Wave Theory

Wave theories have been developed to describe natural wave behaviors. Small amplitude wave theory is deficient in satisfactorily defining all types of wave characteristics specifically for large steepness waves (Sorensen, 2005).

Figure 10 indicates a graph that classifies the wave theories for different wave characteristics. In this figure, the x-axis is relative depth (d/gT^2) and the y-axis is wave steepness (H/gT^2). The appropriate theory, depending on the wave of interest, can be identified and serve as a model of study. However, the sinusoidal waveform (small amplitude) is the most popular to describe wave behavior due to its simplicity. It most covers the deep and intermediate water and not steep waves. For steep waves in deep and intermediate water depth, the Stokes wave theories are the most suitable. For shallower water, a Cnoidal wave theory is suggested. Cnoidal wave theory is the analytical wave theory obtained in terms of elliptical integrals. Breaking line of H/d equal to 0.78 shows where the waves break. Figure 11 shows the different wave forms explained. For more detail of these theories please refer to (Karadeniz, 2013).

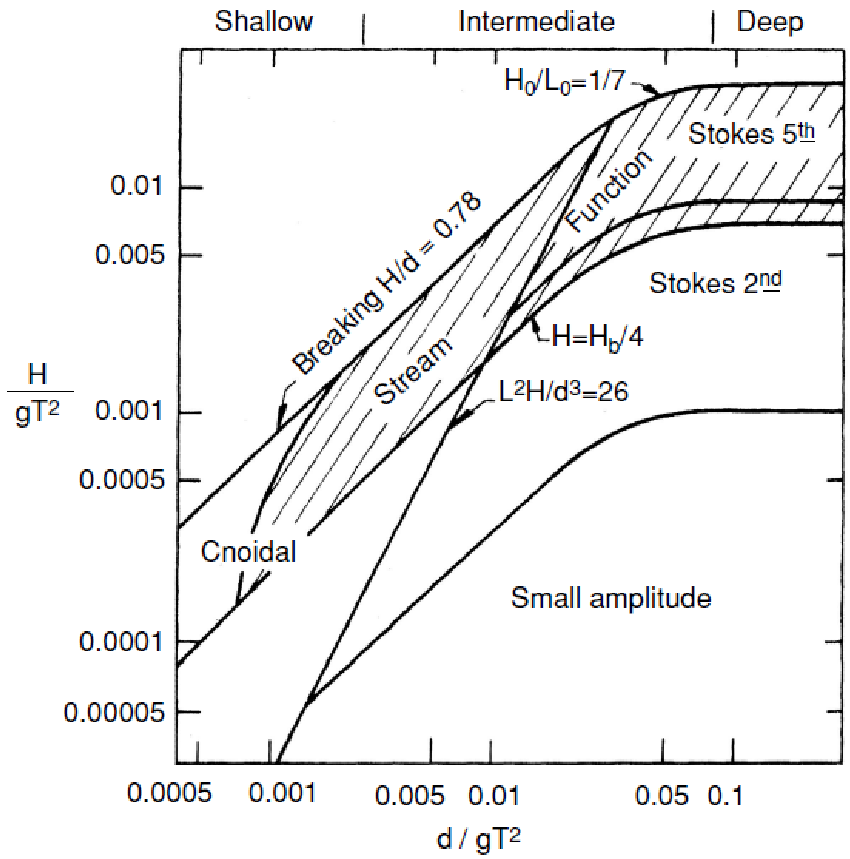

Figure 10: Recommended wave theory selection (Sorensen, 2005)

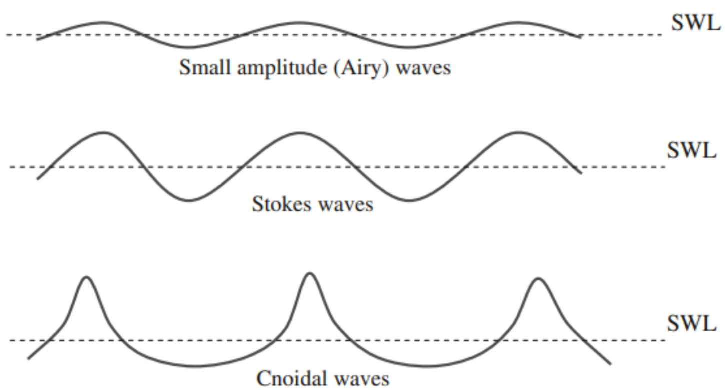

Figure 11: Different wave forms (Karadeniz, 2013).

2.1.4 Wave Kinematic and Pressure

Calculating wave conditions need a method to find water particle velocities and acceleration as well as the pressure field in a wave.

Wave kinematic

The horizontal and vertical component (u and w respectively) of water particle velocity can be determined with the following formula.

$$u = \frac{\partial \phi}{\partial x}, \quad w = \frac{\partial \phi}{\partial z} \tag{12}$$

After inserting the ϕ in the equation (12) and doing some algebraic manipulation it yields equations (13) and (14):

$$u = \frac{\pi H}{T}\left[\frac{\cosh k(d+z)}{\sinh kd}\right]\cos(kx-\sigma t) \tag{13}$$

$$w = \frac{\pi H}{T}\left[\frac{\sinh k(d+z)}{\sinh kd}\right]\sin(kx-\sigma t) \tag{14}$$

These equations give the velocity components at the point (x, -z) as a function of time as different water particles pass. Each velocity component in equation (13) or (14) consists of three parts:

1- The surface deep water particle speed πH/T

2- the terms in brackets account for particle velocity variation over the vertical water column at a given location and for particle velocity variation caused by the wave moving from deep to shallow water

3- phasing term depends on the location in the wave and time

Note: d+z is the distance measured up from the bottom as demonstrated in Figure 8.

The horizontal component of particle acceleration a_x can be written as equation (15):

$$a_x = u\frac{\partial u}{\partial x} + w\frac{\partial u}{\partial z} + \frac{\partial u}{\partial t} \tag{15}$$

Which the first two terms on the righthand side are the convective acceleration and the third term is local acceleration. The magnitude of the first two terms (convective acceleration) for a small amplitude wave theory is the square order of wave steepness (H/L). Since the wave steepness is significantly smaller than unity, the convective acceleration term can be neglected. By neglecting the higher-order convective acceleration term, the acceleration a_x and a_z yields to equation (16) and (17):

$$a_x = \frac{2\pi^2 H}{T^2}\left[\frac{\cosh k\left(d+z\right)}{\sinh kd}\right]\sin\left(kx-\sigma t\right) \tag{16}$$

$$a_z = -\frac{2\pi^2 H}{T^2}\left[\frac{\sinh k\left(d+z\right)}{\sinh kd}\right]\cos\left(kx-\sigma t\right) \tag{17}$$

The water particle orbits around a mean position shown in Figure 8. The vertical and horizontal components of the particle position (ε and ζ respectively) can be found by integrating the particle velocity components with respect to time. It yields to equation (18), (19):

$$\varepsilon = \frac{H}{2}\left[\frac{\sinh k\left(d+z\right)}{\sinh kd}\right]\cos\left(kx-\sigma t\right) \tag{18}$$

$$\zeta = -\frac{H}{2}\left[\frac{\cosh k\left(d+z\right)}{\sinh kd}\right]\sin\left(kx-\sigma t\right) \tag{19}$$

H/2 indicates the orbit radius for a particle at the wave surface in deep water.

By propagating a wave from deep water into shallow water, the particle orbit geometries undergo the transformation depicted in Figure 13, from circular to elliptical. In deep water throughout the water column, the orbits are circular but gradually decrease in diameter with increasing the distance below the surface (Figure 12); approximately die out at half a wavelength distance.

It is important to understand that waves do not transport any volume of water in their direction of propagation. Imagine a ball a few yards out to the sea. As waves propagate toward the shore, the ball will not come toward the beach, it just goes up and down perpendicular. However, it may eventually come to the shoreline due to the tides, wind, or current, but the waves will not carry the ball.

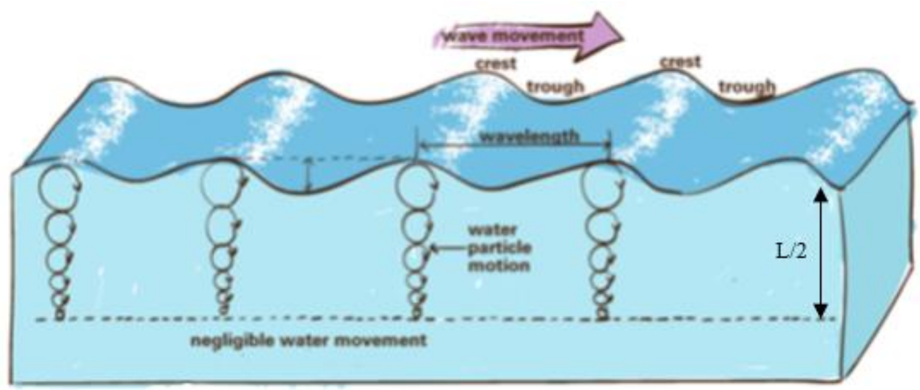

Figure 12: Water particle motion in deep water (Jarocki and Wilson, 2010)

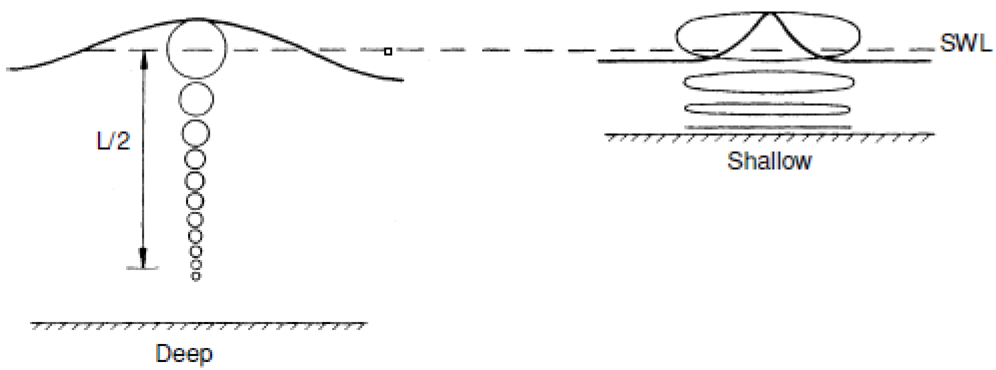

Figure 13: Deep and shallow water surface and particle orbits (Sorenson, 2005)

In transitional to shallow water depth, the elliptical orbits become flattered, especially near the bottom. Near the bed, the particles follow a horizontal path, oscillating back and forth (Figure 13).

In equations (13) to (16), it is advantageous to consider the term in brackets for the deep and shallow water limits to:

Deep water:
$$\frac{\cosh k\left(d+z\right)}{\sinh kd}=\frac{\sinh k\left(d+z\right)}{\sinh kd}=e^{kz} \tag{20}$$

Shallow water:
$$\frac{\cosh k\left(d+z\right)}{\sinh kd}=\frac{1}{kd} \tag{21}$$

$$\frac{\sinh k\left(d+z\right)}{\sinh kd}=1+\frac{z}{d} \tag{22}$$

<u>Pressure field</u>

Substituting velocity potential Eqn (9) into the linearized form of equation (8) (neglecting the velocity squared terms) yields the following equation (23) for the pressure field.

$$p=-\rho gz+\frac{\rho gH}{2}\left[\frac{\cosh k\left(d+z\right)}{\cosh kd}\right]\cos\left(kx-\sigma t\right) \tag{23}$$

The first term on the right side (ρgz) is the normal hydrostatic pressure variation and the second term is the dynamic pressure. The dynamic pressure is due to wave-induced particle acceleration. Figure 14 shows the static and dynamic pressure distribution under a wave peak and trough. For a wave peak, the dynamic pressure increases the total pressure up to the SWL. In the trough, the total pressure is decreased. At a depth of Z=-L/2 the dynamic pressure due to the wave motion approaches zero and the total pressure only consists of the static pressure.

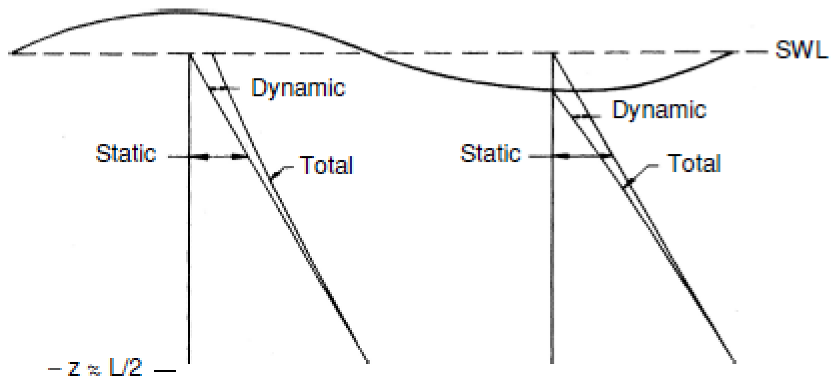

Figure 14: Deep water wave vertical pressure distributions (Sorenson, 2005)

The oscillating dynamic pressure is created by the particles under the crest accelerating downward and under the trough accelerating upward. Between the crest and trough, the acceleration is only horizontal so the vertical pressure is hydrostatic. The equation (23) is not valid above the still water line (SWL).

A pressure gauge at a depth of L/2 or below would measure the static pressure from the SWL. The period of the pressure fluctuation is the same as the wave period.

2.1.5 Wave Energy Resources

The total energy in a surface gravity wave is the sum of the kinetic and potential energies. By considering a small column of water and integrating over one wave length, the kinematic energy can be obtained. Equations (24) to (26) show the kinetic energy, potential energy, and total energy, respectively (Sorensen, 2005).

$$E_k = \int_0^L \int_{-d}^0 \frac{1}{2} \rho dxdz \left(u^2 + w^2\right) = \frac{\rho g H^2 L}{16} \tag{24}$$

$$E_p = \int_0^L \rho g \left(d + \eta\right) \left(\frac{d + \eta}{2}\right) dx - \rho g L d \left(\frac{d}{2}\right) = \frac{\rho g H^2 L}{16} \tag{25}$$

$$E = E_k + E_p = \frac{\rho g H^2 L}{8} \tag{26}$$

2.1.6 Wave Energy Potential Along US Coast

More than 50% of the US population lives within 50 miles of coastlines ("Marine and Hydrokinetic Resource Assessment and Characterization", 2021). There is a great potential to provide local renewable energy to a large share of the US population using marine and hydrokinetic (MHK) technologies. MHK technologies include waves, tidal streams, ocean currents, river currents and ocean thermal gradients can be a great source of energy production. Table 2 shows the estimated U.S. resource and hydrokinetic potential to obtain energy.

Table 2: U.S. marine resource potentials ("Marine and Hydrokinetic Resource Assessment and Characterization", 2021)

Resources	Potential
Waves	*Theoretical:* 1,594–2,640 TWh/year *Technical:* 898–1,229 TWh/year
Tidal streams	*Theoretical:* 445 TWh/year *Technical:* 222–334 TWh/year
Ocean currents	*Theoretical:* 200 TWh/year *Technical:* 45–163 TWh/year
River currents	*Theoretical:* 1,381 TWh/year *Technical:* 120 TWh/year

Theoretical energy is defined as the maximum available energy whereas technical energy is a portion of the theoretical resource that can be captured by specific devices. Roughly 90,000 homes can be powered by 1 TWh/year (Marine and Hydrokinetic Resource Assessment and Characterization, 2021).

2.2 Largest Wave Generators

Flumes and basins are traditional facilities to generate scaled waves for research studies. The waves produced by these facilities inherently have wave height restrictions because of the facility restriction. Oregon State University Wave Research Laboratory has one of the largest flumes in North America and can generate waves at a maximum height of 1.7 meters (5.6 feet). Figure 15 shows the flume.

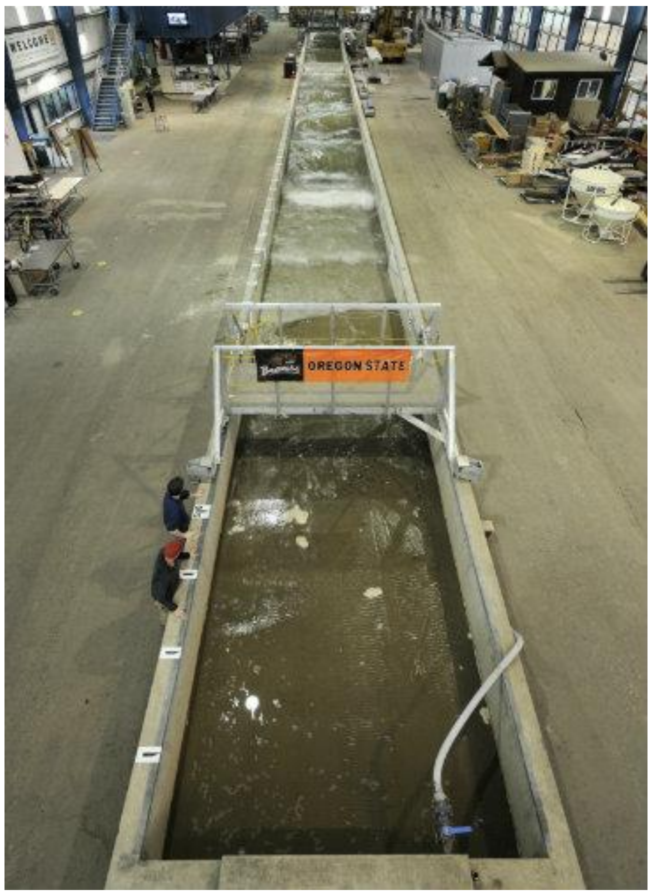

Figure 15: Large wave Flume at OSU (Robert, 2017)

The University of Texas A&M, Offshore Technology Research Center (OTRC) wave basin operates a unique model testing basin that has enabled OTRC to become a world leader for offshore technology research and testing (Figure 16-a). The OTRC model basin is capable of large-scale simulations of waves, and currents on different floating structures. The wave basin is 45.72 m (150 ft) long and 30.48 m (100 ft) wide, and 5.8 m (19 ft) deep. There are 48 individually controlled wavemaker paddles that can generate a variety of wave conditions, including unidirectional and multidirectional regular and irregular waves (Figure 16-b). Also, there are sixteen dynamic fans that can generate gusty wind conditions from any direction.

(a)

(b)

Figure 16: (a) OTRC wave basin (Offshore Technology Research Center) (b) OTRC wave paddles

Deltares Delta Flume in the Netherlands is the world's largest wave generator. Its flume is 300 meters long, 9.5 meters deep and 5 meters wide. With this length, it can simulate wave formation on gradually rising coasts. The depth makes it possible to generate waves up to 4.5 meters high. Figure 17 shows the facility.

(a)

(b)

Figure 17: Different view of Deltares Delta Flume (a) Close-up (b) Out door

2.3 Wave Energy Converters History

WECs are devices that can convert power from ocean waves into a useable form of energy, such as electricity. Waves can be a sustainable source of energy and a variety of wave energy converters (WEC) have been developed to extract energy from waves, either onshore or deeper offshore. (Wave devices, 2019). These devices can be categorized by the installation location (shoreline, near shore, and offshore) or the Power Take-Off (PTO) system. Also, most devices can be characterized as belonging to one of six types: Attenuator; Point absorber; Oscillating wave surge converter; Oscillating water column; Overtopping device; Submerged pressure differential. The history of WEC comes back to the oil crisis in the 1970s when a device was invented by Stephen Salter at the University of Edinburgh and was known as “Salter’s Duck.” And shown in Figure 18 (Thorpe, 1999). Stephen Salter is widely known as the pioneer in model testing of wave energy converters. The device was able to convert wave power into electricity. The wave impact caused rotation of gyroscopes inside a pear-shaped "duck", and an electrical generator converts this rotation into electricity with up to 90% efficiency (Thorpe, 1999; Wikipedia contributors, 2019). However, some difficulties discouraged people from the widespread use of the device. The downside of the device was high capital cost, durability in storms, environmental and navigational problems, etc. (Mcwilliams, B. 2000).

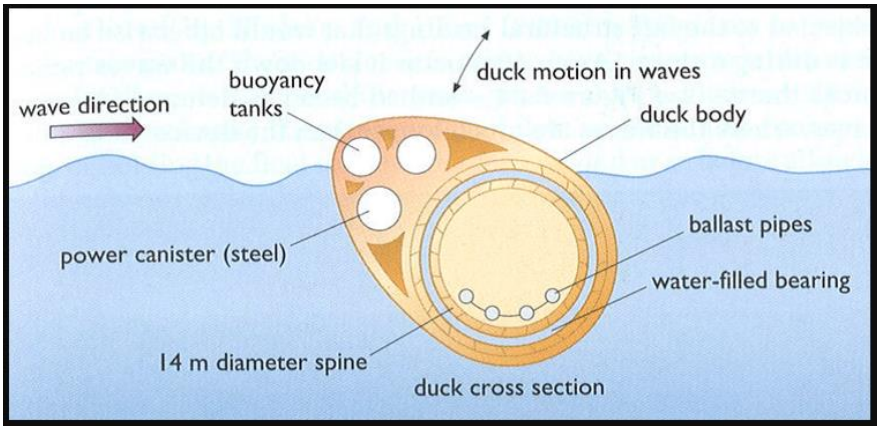

Figure 18: Salter's Duck (Thorpe, 1999)

Due to decreasing oil prices in the 1980s, wave-energy funding was drastically reduced and much of the research on WEC slowed. More recently, following the issue of climate change and oil independency, there is again a growing interest all over the world for renewable energy, including wave energy.

The first actual WEC device to produce electricity from ocean waves was the Pico Power Plant, built-in 1999 on the Island of Pico, in the Azores, Portugal (Figure 19), (Antonio, 2010). The Pico WEC was an onshore system that utilized entrapped air in an enclosed chamber to run a turbine. The incident waves cause the vertical movement of the water column inside the chamber. The water oscillation causes the air to flow in and out of the turbine. This device is known as an oscillating water column. In 2009, after some turbine modification nearly 1MWh was produced in one 48hr period alone. Currently, the plant is still operational and is managed by the Portuguese consortium called the Wave Energy Centre (WavEC). (Clément et al., 2002)

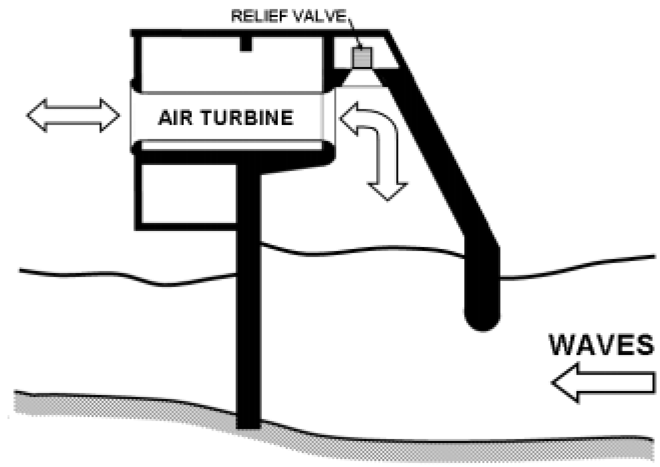

Figure 19: Cross-sectional view of an OWC (Pico plant), (Antonio, 2010)

Pelamis was the name of the first commercial WEC plant, designed and built by the Scottish company name Pelamis Wave Power, and connected to a grid to utilize electricity (Figure 20). The device was semi-submerged and consists of several cylindrical sections connected with hinged joints. Hydraulic pumps were used to utilize the bending motion inside the joints, which is caused by the passing waves. The device was held in position by a mooring system. The generation capacity of a square kilometer farm was about 30 MW. Each device is capable of generating 750 kW energy. Cost estimation for a single device (estimated in 2004) was $2 to $3 million. (Burman and Walker, 2009). However, the device had some advantages include low cost of investment and decreasing pollution, etc., there are some disadvantages include disturbance of marine life and a possible threat to navigation from a collision due to low profile above the water.

Figure 20: Pelamis (Holmberg et al., 2011)

2.3.1 Point Absorber

A point absorber is a floating structure that can absorb energy from all directions through its movements (Figure 21). The relative motion of the top buoyant to the base one converts into electrical power. Direct electrical drive PTO systems usually are using for point absorber WEC devices. This PTO system converts the mechanical motion of the heaving buoy directly to electricity. Table 3 shows different types of commercial point absorbers developed by different companies/universities.

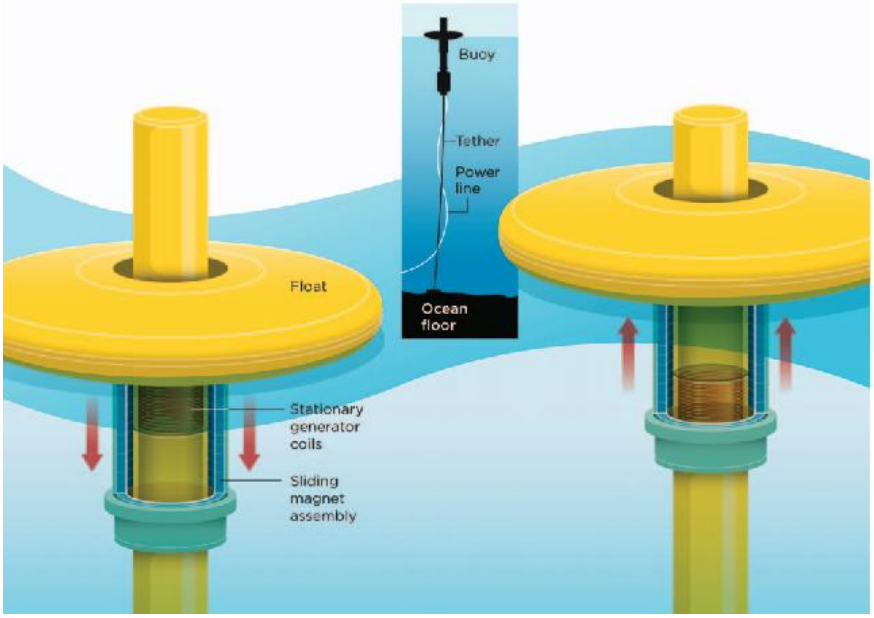

Figure 21: The power buoy- point absorber Wave Energy Converter (Brekken, 2011)

Table 3: Different types of point absorber

Developer	Power	Specifications
Columbia Power (CPT) *(Rhinefrank et al. ,2010; Brekken, 2010)*	250 kW to 1 MW	20 m dia * 25 m draft
OPT- PB 500 *(Dufera, 2016)*	500 kW	15.2 m dia* 45.7 m height
Finavera (Finavera point absorber)	250 kW	6 m dia* 2 m freeboard * 33.5 m draft
Seabased/ Uppsala Univ. *(Chatzigiannakou, 2019)*		7- 11 m height
Archimedes Waveswing *(Prado et al. ,2013)*	250 kW	48 m x 28 m x 38 m
SeaRev *(Cordonnier et al., 2015)*	500 KW	
Wavebob *(Weber et al., 2009)*	500 kW	20 m dia

So et al. in 2019 modeled a point absorber wave energy using WEC-Sim software, which is an open-source code for simulating wave energy converters. Results showed an agreement between the numerical and experimental data over most ranges of operation, except near-resonant frequencies, which the numerical over-predicted the performance.

Maloney in 2019 created a numerical model simulation within ProteusDS, a time-domain modeling software to investigate the Variable Inertia System Wave Energy Converter (VISWEC). The VISWEC is a self-reacting point absorber (SRPA) converter which by using an internal reaction mass system, is capable of changing its mechanical impedance. The reaction mass can modify its inertia and this change has the effect of creating an added inertial resistance. Shadman et al. in 2018, optimized the one-body heaving point absorber geometry located in a nearshore region of the Rio de Janeiro coast.

Devolder et al. in 2018, simulated floating point absorber subjected to regular waves numerically with CFD toolbox. Results compared with the WECwakes dataset and a good agreement with CFD is demonstrated for the WEC's heave motion.

Beatty et al. in 2019 carried out experimental and numerical comparisons of the performance of two self-reacting point absorbers in irregular waves. The experimental model consisting of a 1:25 scale model tests and a feedback-controlled power take-off system. A time-domain numerical model generated and validated by the experimental results in terms of power and capture width matrices, and mean annual power production. Results indicate 41% improvement in mean annual energy production for the point absorber with damper plate compare to the wave energy converter design with streamlined reacting body at a representative location near the West Coast of Vancouver Island, British Columbia, Canada.

2.3.2 Oscillating Wave Surge Converter (OWSC)

The primitive generation of Oscillating Wave Surge Converter (OWSC) consisted of a hinged paddle suspended from above the water surface. The pivot axis was approximately parallel to the wave crests. (Folley et al. 2004). The next generation of OWSC was the bottom-hinged Oscillating Wave Surge Converter (OWSC) that is improved the efficiency because it matches the motion of the water particles better. This is due to the larger circular rotation of water particles near the surfaces where the paddle also has the largest rotation. Oscillating wave surge converter (OWSC) concepts are well designed to weather severe wave climate since they are hinged to the seabed with a submerged flap penetrating the water surface. During the storm, they can be laid flat on the ocean floor. Oyster is a commercial name formed by Aquamarine Power Ltd in 2005 that uses this concept (Holmberg et al., 2011; Whittaker and Folley, 2012). Figure 22 shows the concept of this device.

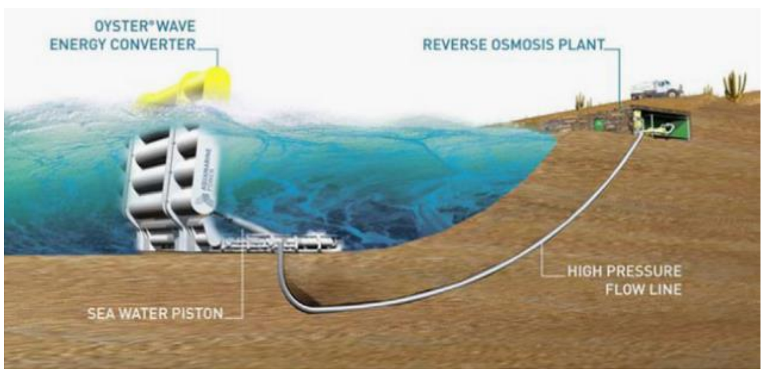

Figure 22: Oyster, OWSC (Whittaker and Folley, 2012)

Whittaker and Folley in 2012 investigated the nearshore oscillating wave surge converters (OWSC) and the development of Oyster. They discussed different variables of the OWSC and their effects on capture width, frequency bandwidth response and power take-off characteristics. In 2019, four different OWSC concepts were hydrodynamically analyzed and compared by Gunawardane et al. The four concepts were; an isolated flap, a flap with a wall in front, a flap inside a caisson with an isolated water chamber behind the flap and a flap inside a caisson with a water chamber behind the flap that is linked to the water outside with a gap under the flap. The (dis)similarities between the different models were identified and discussed.

Henny et al. in 2018 investigated a conceptual model, (seabed-mounted, bottom-hinged, flap-type) of the hydrodynamics of an OWSC. Their conceptual work was validated with the numerical program WAMIT and compared with the physical modeling. WAMIT® is an advanced set of tools for analyzing wave interactions with structures, vessels, or offshore platforms. They concluded that to maximize the capture factor at the tested specific location (North Atlantic site), the flap should be approximately 20–30 m wide, pivoted close to the seabed, with large diameter rounded side edges and the top edge penetrating the water surface.

Loh and Young in 2018 assessed wave-structure interaction for OWSC using a CFD software package. They used OpenFOAM® to predict and analyze the behavior of an OWSC subjected to various types of wave conditions in a Numerical Wave Tank (NWT). They showed that OpenFOAM® can provide an understanding of the complex hydrodynamic analysis. The OWSC simulation with the software can have a reliable prediction of highly nonlinear wave structure interactions. Zhang et al. in 2018 used the numerical smooth particle hydrodynamics SPH method to investigate the hydrodynamic characteristics of a bed hinged OWSC. Their results showed that the active power of the OWSC strongly depends on both the wave periods and the PTO damping coefficients.

2.3.3 Attenuator

Attenuators are types of wave energy converters that are typically floated in parallel to the wave direction. The attenuator devices are relatively lengthy (up to 150m) consisting of different buoyant segments hinged together and articulated by crossing the waves. Each segment should be smaller than ¼ wavelength; otherwise, the segment will start counteracting itself (Holmberg et al., 2011). The energy can be extracted from the relative movement of each segment, usually through the hydraulic PTO system. An attenuator can be designed for a specific wave climate ranging from small to large wavelengths. Pelamis (Figure 20) was an example of this type and due to its size, mostly used for longer waves Te > 7s with acceptable performance for the North Atlantic sea. The other type of attenuator was the Anaconda wave energy converter, which instead of hinged segments, the device was made up of one large rubber tube filled with water and anchored to the bed. The water enters through the stern and returns to the sea at the bow. The passing wave causes changes in pressure along the tube, creating a "bulge". As the bulge travels through the tube it grows and can be used to drive a standard low-head turbine located at the bow (Koca et al. 2013). Sea Power, Wave Star and Oceantec are the other types of an attenuator.

Yang et al. in 2018 numerically simulated an attenuator using a one-fluid formulation. Taniguchi et al. in 2018 experimentally investigated motions and loads characteristics of an attenuator wave energy converter (AWEC). The device was consisting of a set of cylindrical floats with two degrees of freedom joints. The AWEC's simulation model with a commercial code, the Orcaflex, was simulated and the results were compared to the prototype. The model reasonably explained measured loads on the AWEC. Awang et al. (2018) experimentally investigated unidirectional waves with different wave conditions and model configurations were conducted to assess the wave energy loss on a porous cylinder. The influences of water level, wave steepness, wave number and porosities were studied. The test results showed that by lowering the percentage of porosity, more wave energy can be dissipated, which decreases the transmitted wave heights. The other type of attenuator wave energy converter was M4 which originally consists of three in-line buoys increasing in diameter and draft from bow to stern.

Moreno and Stansby (2018) carried out an experimental test for a six-float system for irregular unidirectional waves. They showed that the power capacities similar to wind turbines were possible to achieve with similar electricity costs.

2.3.4 Oscillating Water Column (OWC)

An oscillating water column (OWC) is a hollow structure partially submerged, in the form of a blowhole. The submerged structure is open at the front facing the sea. On top, a column of air is entrapped with an air turbine (Figure 23). As the wave approaches the device, the wave impact causes the water column inside the device to oscillate up and down which compresses and decompresses the air column, causing the air turbine to rotate. This trapped air is in direct contact with the atmosphere via an air turbine, by rotating the turbine regardless of the direction of the air flow, electricity can be generated (Heath et al., 2012). Islay LIMPET (Land Installed Marine Power Energy Transmitter), Oceanlinx, Pico, Sakata and Mighty Whale are examples of OWC devices (Rusu and Onea, 2018).

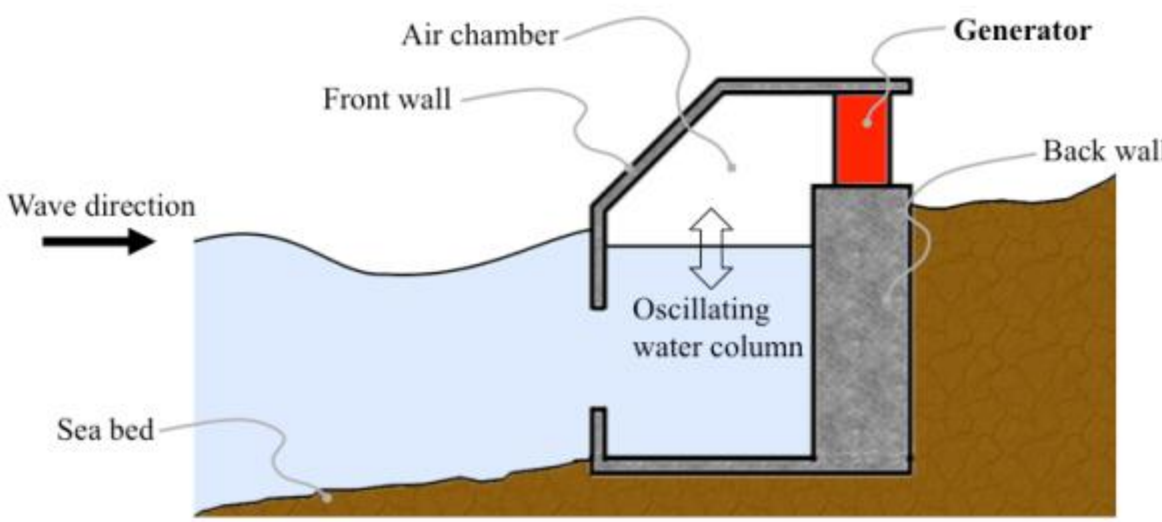

Figure 23: Bottom-fixed oscillating water column (Vertechy et al. 2013)

Ning et al.in 2019 numerically and experimentally investigated the wave dynamics of a dual-chamber OWC device. Based on the potential-flow theory and time-domain Higher-Order Boundary Element Method (HOBEM), they developed a fully nonlinear numerical wave flume to simulate the interaction between air, fluid (wave), and the dual-chamber OWC device. They also tested the device in the wave-current flume at the State Key Laboratory of Coastal and Offshore Engineering, Dalian University of Technology. Results of the numerical and experimental data were compared. Connell et al. (2018) presented the development of CFD models to simulate OWC free heaving buoy with non-linear power take-off. They applied a range of regular waves and compared the responses of heaving and the chamber pressures with experimental data, which showed an excellent correlation.

2.3.5 Overtopping Device

Overtopping or terminator devices can convert energy to electricity by capturing waves as they overtop into a storage reservoir. There are two types, offshore and onshore overtopping devices. The offshore overtopping device is a large, floating reservoir with reflectors, ramps and a reservoir, which include a turbine at the bottom of the reservoir. Onshore or coast base devices are equipped with the same low-pressure hydroelectric power station with a reservoir and a turbine. The reservoir is fed by waves that are guided by reflectors and trapped by a wide opening channel that connects the sea to the reservoir. Norwegian TAPCHAN is an example of this device (Figure 24). This method can be effective where there is only a limited tide and water does not recess (Bevilacqua and Zanuttigh, 2011).

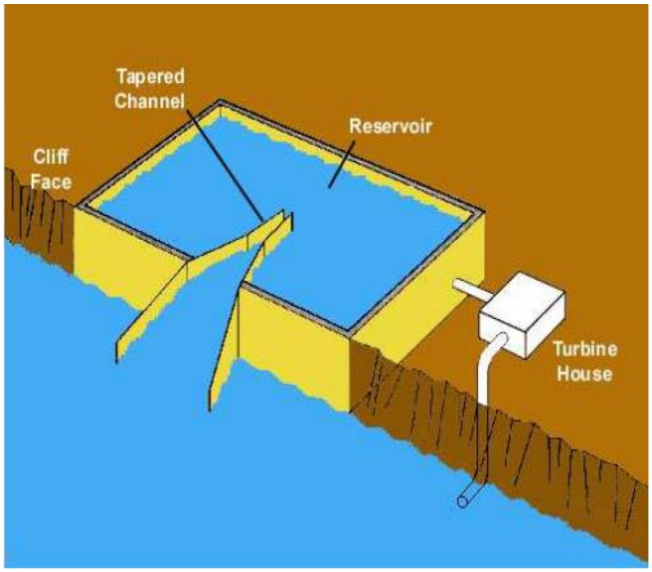

Figure 24: TAPCHAN WEC (Bevilacqua and Zanuttigh, 2011)

The wave dragon device shown in Figure 25 is the name of the most widely known offshore overtopping device. The size of the device is 260X150 m and 16 m in height. Depending on the wave activity each unit can generate 4-10 MW energy.

Figure 25: Frontal view of wave dragon (Bevilacqua and Zanuttigh, 2011)

By using a pair of large curved reflectors, this device directs waves into the central receiving part, where they flow up a ramp and overtop into a raised reservoir, where water is returned to the sea via several low-head turbines (Bevilacqua and Zanuttigh, 2011).

Different researchers worked numerically and experimentally on overtopping devices. Barbosa et al. (2019) utilizing OpenFOAM and fluent code performed 2D numerical analyses of near-shore overtopping devices to investigate the effect of the curvature of the platforms on water discharge. Results showed that numerical models are matched and comply with the expected characteristics determined with mathematical classical equations. Hubner et al. (2019) numerically evaluate the realistic and regular waves over an overtopping device. The regular wave was generated by a User Defined Function (UDF) also the realistic wave was produced by imposing the realistic components velocities from transient discrete values, named Table Data (TD) in FLUENT software (Cappietti et al., 2019).

2.3.6 Submerged Pressure Differential

Submerged pressure differential Wave Energy Converter devices are typically sitting on the seabed and located near the shore. The waves passing overhead causes the water level to rise and fall, inducing a pressure difference in the device. The Archimedes Wave Swing (AWS) is one of the examples of this type. The AWS is a fully submerged offshore point absorber WEC. Two main parts are a bottom-fixed air-filled cylindrical and a movable upper floater. The floater heaves due to changes in wave pressure. When the wave peak is at top of the AWS the floater moves down compressing the air inside the AWS. When the wave trough crosses the AWS, pressure decreases and consequently the air expands and the floater moves up (Valerio et al., 2007).

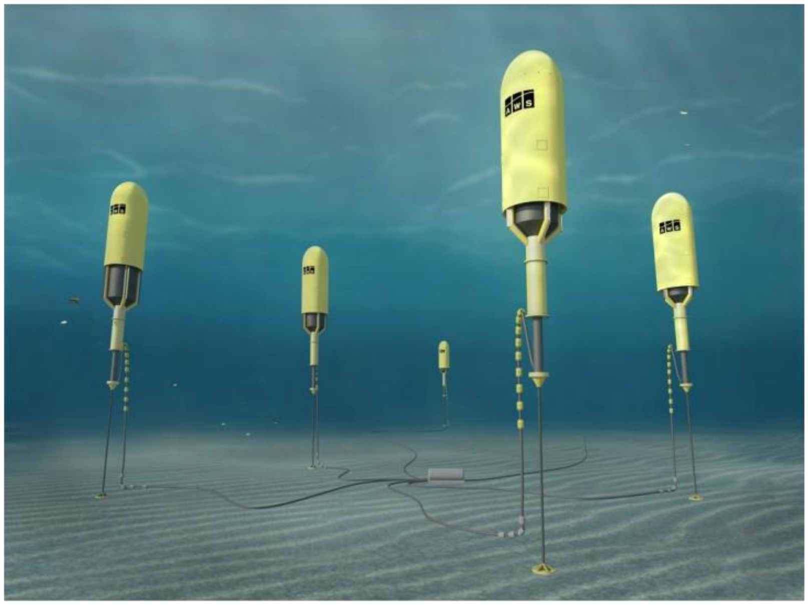

Figure 26: Archimedes Wave Swing (AWS)

Barbarit et al. in 2017 investigated the energy absorption rate on a fixed-bottom pressure differential wave energy converter. As shown in Figure 27 two different sets of chambers were assumed. One moving surface was in the bottom the other was on the top. Their results showed the moving surface on the top can be better tuned with a natural frequency.

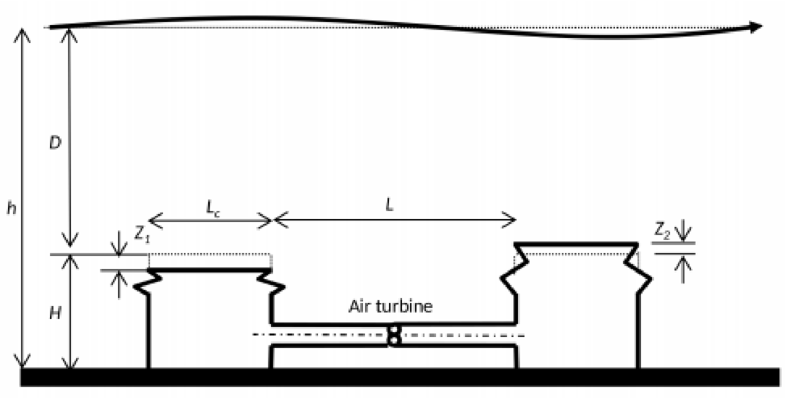

Figure 27: Cross-section of top moving surface wave energy converter (Babarit et al., 2017).

Another research team in 2018 investigated the scouring and morphology evolution induced by submerged pressure differential energy converter. They explored different methods to mitigate the scouring, including permeability and relative elevation to the seabed (Lomonaco et al.)

Lehmann et al. (2014) at Berkley university investigated a wave energy conversion device called Wave Carpet. The wave carpet is another submerged pressure differential WEC device composed of linear springs and generators. The device is omnidirectional, sits under the water surface and can endure severe storms. since the device is submerged it is highly survivable against the storm waves, while at the same time is eco-friendly. They presented a basic analytical model and experimental tests to develop and optimize the device. The results endorsed the wave carpet's capability to convert wave energy efficiently in different wave conditions.

2.4 Efficiency of Wave Energy Converters

In this section the efficiency of the WEC is explored, however since the absorbed power for the proposed device is not available, The efficiency of the OWC device (which is the closest concept) is explained. The efficiency of the WEC device is the ratio of the generated energy to the total available energy (CF = P_p/P_w). Wave energy per unit time in the direction of the wave is called the wave power P. The dynamic pressure, which is total pressure minus hydrostatic pressure, provides the wave force and the flow velocity in the horizontal particle velocity. The term in parentheses in equation (27) shows dynamic pressure. By inserting dynamic pressure term from equation (23) and velocity from equation (13) into equation (27) and integrating lead to Equation (28), which shows the total available wave power (Sorensen, 2005).

$$p_w = \frac{1}{T}\int_0^T \int_{-d}^0 \left(p + \rho g z \right) u\,dz\,dt \tag{27}$$

$$p_w = \frac{\rho g H^2 L}{16T}\left(1 + \frac{2kd}{\sinh 2kd}\right) \tag{28}$$

After finding the denominator of the efficiency (Eqn (28), the nominator, which is the absorbed potential energy of WEC, needs to be obtained. The pneumatic power per unit width of the OWC converter can be calculated by equation (29) (Lopez and Iglesias, 2014).

$$p_p = \frac{1}{bt_{\max}} \int_0^{t_{\max}} Q\Delta p dt \tag{29}$$

Where b is the chamber width, Δp is pressure drop between the chamber and atmospheric pressure, Q is the air flow-rate through the hole and t_{max} is the duration of the test.

Different researchers have studied the efficiency of wave energy converters in different locations. In 2014 Rusu assessed and compared the wave power resources in different locations. He compared the performances of three WEC types (Aqua Buoy, Pelamis and Wave Dragon) in the three different coastal environments location. The results showed that only the evaluation of the wave energy in a certain location is not sufficient. The important key is the correlation between the power matrix of a WEC and the scatter diagram. Chen et al. (2019) investigated the force and efficiency of different buoys in low-wave energy density. Their results showed that the common responses occurred both in the hemispherical and cylindrical buoys. The efficiency of the submerged plate wave energy converter was experimentally assessed by Orer and Ozdamar (2007). They obtained that the efficiency of the submerged plate wave energy converters can reach up to 60%.

The effect of the mooring system on efficiency was also investigated by Cerveira et al. (Cerveira et al, 2013). They analyzed the mooring system effects on the dynamics and efficiency of an arbitrary floating WEC device and assessed in terms of wave-induced motions and absorbed power. They presented the results for the transfer functions, expected annual absorbed energy and the statistics in selected stationary sea-states. Lopez and Iglesias (2014) presented a novel approach that considers the influence of the chamber or the turbine and the tidal level. They developed a virtual laboratory to determine the pneumatic efficiency of an OWC under specific wave conditions (wave height and period), tidal level and turbine damping. The efficiency of the OWC chamber is quantified by the ratio of the absorbed power and the available wave energy. Babarit et al. in 2017 investigated the energy absorption performance of a fixed-bottom pressure-differential wave energy converter (WEC). They considered two versions of the technology, one with the moving surfaces on the bottom and the other on the top of the air chambers. By developing numerical models in the frequency domain, the power absorption of the two versions is assessed and observed that the moving surfaces on the top respond better with the natural period of the system.

CHAPTER 3. CONCEPTUAL PROPOSED DEVICE

This study explores a novel submerged oscillating water column (SOWC) device that can be classified in the category of submerged pressure differential. The concept combines the existing technology of point absorbers with oscillating columns under completely submerged conditions. The guidelines that were used to develop the idea included minimizing environmental and aesthetical impacts (visual pollution), located it near shore facilitate operation and maintenance, locate it on the ocean floor to improve the ability of the device to weather severe weather events, and make it modular and scalable.

The proposed idea consists of two hollow cylinders that are capped at the top end, with the two cylinders connected near the top with a pipe/tube that allow air motion between the cylinders. The cylinders are mounted vertically to the seabed with openings near the bottom to allow water in and out. A pocket of pressurize air is maintained in the top of the cylinders providing an air/water surface interface for floats. An embedded float/buoy can be placed inside the cylinders to be used for the power-take-off (PTO) to convert the buoy motion into power.

By itself, one cylinder would be nothing more than a pressurized bubble under the ocean surface. However, by connecting the air reservoirs of multiple cylinders, it allows a constant pressure to be maintained between the SOWCs. The pressure within the SOWC is similar to the wave surface with constant pressure. Figure 28 shows a simplified conceptual model. As waves move across the ocean surface, peaks and troughs create oscillating hydrostatic pressure differentials throughout the water column. Ideally, by placing SOWCs one-half of a wavelength apart, one SOWC experiences an increase in pressure, while the other SOWC sees a decrease in pressure. Connecting the air reservoir between the two SOWCs allows the air to move between the devices, with the increased pressure raising the water surface inside one column while the decreasing pressure lowers the water surface in the other column. The floats inside the SOWC will use the principle of buoyancy to drive a shaft connected to a pump, converting wave energy to mechanical energy. Simply stated, a buoyancy force is applied to a submerged body equal to the specific weight (γ) of the displace fluid times the displaced volume(V); $Fb = \gamma V$. While testing the PTO device is not part of this study, a potential PTO could consist of a dual pump that pressurizes water both on the rising and falling of the buoys. The pressurize water could be sent via a high-pressure transmission line to a turbine on the shoreline. Modular SOWCs could be connected together to increase the flow rate and hence power production. The main goal of this research was to the test the concept of the SOWC and quantify and maximize the conversion rate of the oscillating water column inside the cylinders with the wave free surface. To complete the research, Computational Fluid Dynamics (CFD) and a small-scale physical model were used for proof of concept. For the numerical model, a solid model was constructed using CAD and import into a commercially available CFD code, Flow-3D®. Chapter 4 explains the numerical simulation in detail. For experimental tests, 3 pairs of model SOWC cylinders with different diameters were constructed and tested with waves of differing amplitudes and wavelengths. The physical model details are outlined in Chapter 5.

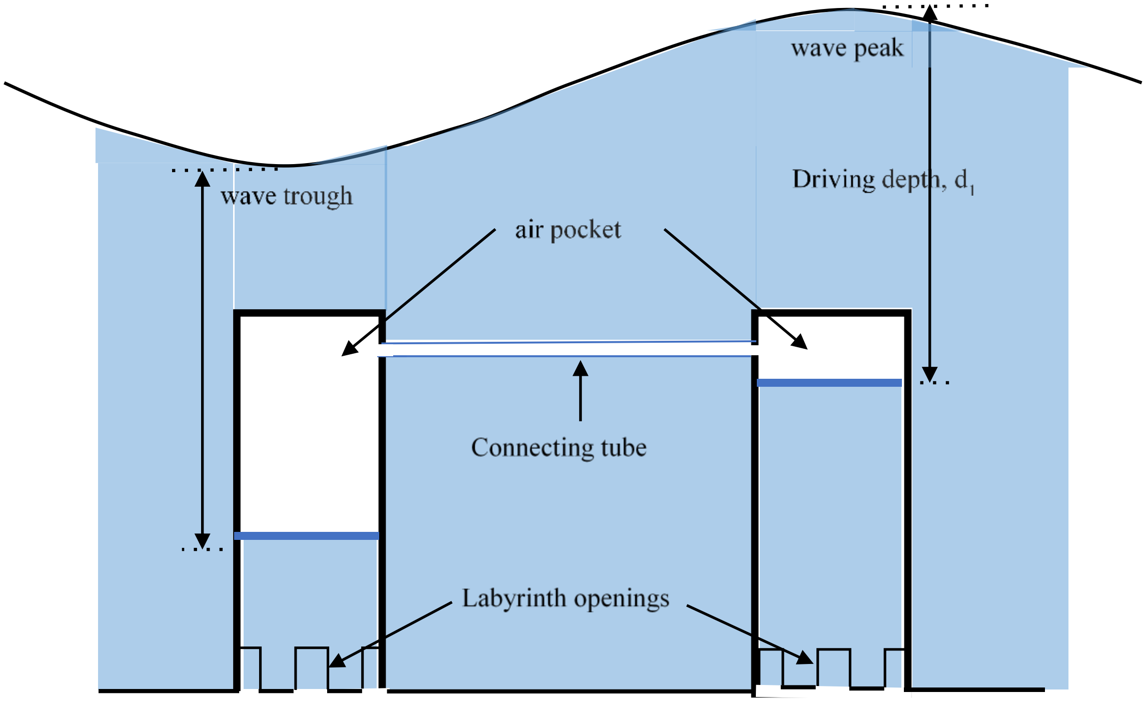

Figure 28: Proposed new wave energy device

CHAPTER 4. NUMERICAL MODELING

To validate the proposed conceptual device, numerical tests were designed to test the concept at prototype scale. Seventeen different numerical simulations were completed by varying the cylinder height, h (61 cm and 91.44 cm) (two and three feet); water depth, d (1.2– 2.44 m) (four-eight ft); cylinder diameter, D (15.24 cm) (constant at 0.5 foot); wave period, T (1.75 s-3.0 s).; and wavelength, L. Another variable in the numerical test setup is the opening in the SOWCs. The different openings were evaluated to test the entrance effect on the conversion efficiency. Five different openings at the bottom of the cylinders were used with additional tests, bring the 27 additional simulations. The different test scenarios with the results are shown later in Table 5.

This chapter outlines the Computational Fluid Dynamic (CFD) method and the governing equations of fluid flow. The commercial software, Flow-3D and details of the setup including the turbulence model are explained. The results from the simulations are reported with the conversion ratio and discussed.

4.1 Computational Fluid Dynamics

Computational fluid dynamics (CFD) is a branch of fluid mechanics that analyzes and solves problems involving fluid flows using numerical analysis. The general process is outlined in Figure 29 (Zuo, 2005). To solve a fluid problem, the physical properties of the fluid are identified using basic principles from fluid mechanics. Then mathematical equations can be used to describe the principles. The Navier-Stokes equations are the governing mathematical equations of CFD. By time-averaging, the NS equations it is transformed into what is known as Reynolds-Averaged Navier-Stokes (RANS) equations, the most common form of the equations.

The partial-differential RANS equations consist of three momentum equations, the continuity equation and ofttimes the energy equation is included. While simplified boundary conditions can allow an analytical for a few simple geometries, most problems require a numerical solution. To solve this equation by computer, the flow domain is discretized into a numerical mesh. Different numerical techniques use specific discretization methods, such as Finite Difference, Finite Element and Finite Volume methods (Zuo, 2005).

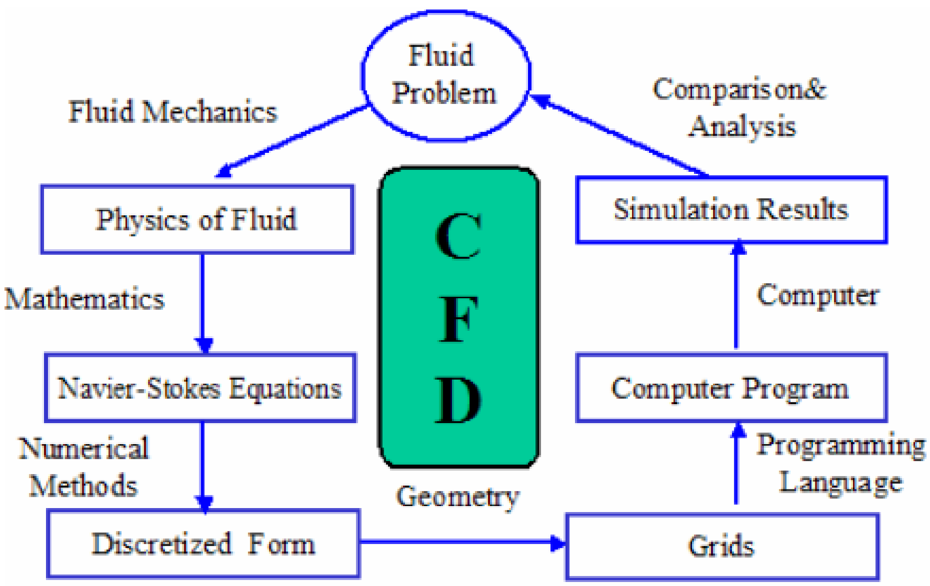

Figure 29: Process of CFD (Zuo, 2005)

In the CFD, the computational domain can be discretized into a grid of cells. Fluid flow parameters, including pressures, velocities, etc. are calculated as a function of time at each cell node. The cells are fixed cuboids. On each side of the computational domain, a boundary condition needs to be defined. Boundary conditions are usually a layer of hypothetical cells at the simulation's perimeter that reflect a state of interest for each side.

Flow-3D is commercially available software that can model free surface flows and ocean wave behavior and solve fluid flow based on the RANS equations. FLOW-3D differs from other

CFD applications in tracking the location of fluid surfaces. Special numerical methods are used by the software to track the surfaces and apply the correct dynamic boundary conditions at those surfaces. In FLOW-3D, the Volume of Fluid (VOF) technique is used to model-free surfaces. FLOW-3D was selected to complete the numerical modeling based on its successful treatment of free surfaces.

The numerical method in FLOW-3D is based on solving the Reynolds-averaged Navier-Stokes (RANS) equations and the continuity equation from cell to cell. The time step is controlled by various stability criteria associated with fluid flow. If there is significant flow in a cell with a wide-open face area and a small volume, the program restricts the time step to small values. (FLOW-3D Cast FAQ, 2009).

4.2 Governing Equation

The numerical method in this study was based on solving the Reynolds-averaged Navier–Stokes (RANS) equations with a finite-volume method. Breaking the flow variable (like velocity *u*) into the mean (time-averaged) component (ū) and the fluctuating component (u’) is called Reynolds decomposition. As mentioned before the conservation equations for fluid flow are based on the principles of conservation of mass, momentum and energy and are known as the Navier-Stokes (NS) equations (Cebeci and Cousteix, 2005).

Continuity and momentum, equations (30) and (31), respectively, govern the motion of the fluid.

$$\frac{\partial}{\partial x}\left(uA_x\right)+\frac{\partial}{\partial y}\left(vA_y\right)+\frac{\partial}{\partial z}\left(wA_z\right)=0 \tag{30}$$

$$\frac{\partial U_i}{\partial t}+\frac{1}{V_F}\left(U_j A_j \frac{\partial U_i}{\partial x_j}\right)=-\frac{1}{\rho}\frac{\partial P'}{\partial x_i}+g_i+f_i \tag{31}$$

Equation 31 with its vector notation represents the momentum equation in each coordinate direction. The variables *u, v* and *w* are velocities in the x, y, and z directions; V_F is the fluid volume fraction in each cell and can be empty, full, or partially filled with fluid that gives the value of zero, one, or between zero and one. A_x, A_y, and A_z shows the fraction of open area in the x, y, and z directions; ρ is the density; P' is the pressure, and g_i is the gravitational force. The variable f_i represents the Reynolds stresses (Savage and Johnson, 2001).

4.3 Turbulence Model and Adiabatic Bubble

Turbulence was modeled using the Renormalized Group (RNG) Theory. The Renormalized Group (RNG) k-ε model (Yakhot & Orszag 1986, Yakhot & Smith 1992) is an improved version of the standard two-equation k-ε model. It extends the capabilities of the standard k-ε model and provides better coverage of transitionally-turbulent flows and mass transfer. Generally, RNG has wider application versus the k- ε equations (Flow3D user manual, 2017).

Since a volume of air is contained within the top region of the SOWCs, the air was modeled as a void region using an adiabatic bubble with an assigned void pressure rather than modeling as a second fluid. Computationally, this is an advantage because it significantly reduces the computational time. The other reason that the adiabatic bubble model can be successfully used when there is a small change in pressure and no heat transfer. In essence, Flow-3D treats the airflow as a confined adiabatic bubble. The bubble model evaluates the void region pressure based on the volume by using the isentropic model of expansion/compression in which PV^{γ} is constant. Where P is pressure, V is volume, and $\gamma = C_p/C_v$. C_p is specific heat for constant pressure and C_v is specific heat for a constant volume.

4.4 Computational Mesh

Flow-3D solves the fluid equations of motion at the cell nodes specified by the user-defined mesh. The mesh discretizes the simulation into small rectangular cells (grid), and each cell has multiple nodes (grid points and center) where the averaged values of flow parameters such as pressure and velocity are evaluated. To accurately model fluid flow behavior, the mesh needs to be sufficiently refined. However, as the mesh size becomes more refined, the simulation becomes more computationally intensive because of the additional cells. The total computational time to complete a simulation is a function of the computing power and optimized mesh size (FLOW-3D user manual, 2021). Figure 30 shows an example of the numerical grid that was constructed to test the SOWCs. The grid domain is subdivided with three linked and one embedded mesh block. The total cell numbers in all mesh blocks is over 487,500. Linked mesh blocks are defined as mesh blocks that share common boundaries, and an embedded mesh block is defined as being nested inside another larger block. Embedded mesh blocks are generally used to increase the accuracy of the flow domain at a given location by using more cells to compute the flow parameters. The total flow domain was greater than four times the wavelength (4λ). A wave absorber is placed at the end of the domain to damp the waves, otherwise, the Water Surface Level (WSL) will start to artificially change in depth due to the reflecting waves (detailed in section 4.5.3.1). Mesh blocks, wave absorber and all 4 buoys are shown in the following Figure 30. The embedded mesh referenced as mesh 2 in the figure, is refined to include at least 4 cells across the connecting pipe cross-section (Figure 31). Four cells are the minimum required number of cells that can capture the flow inside the pipe.

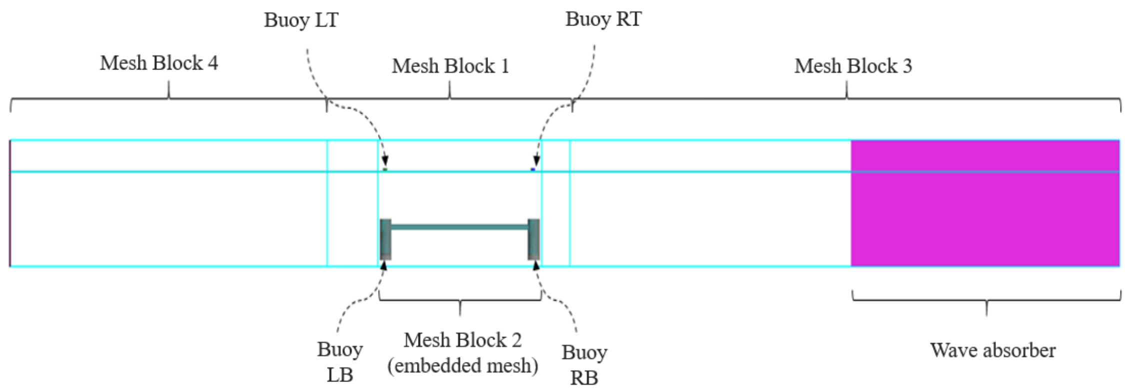

Figure 30: Mesh blocks, Buoys and wave absorber

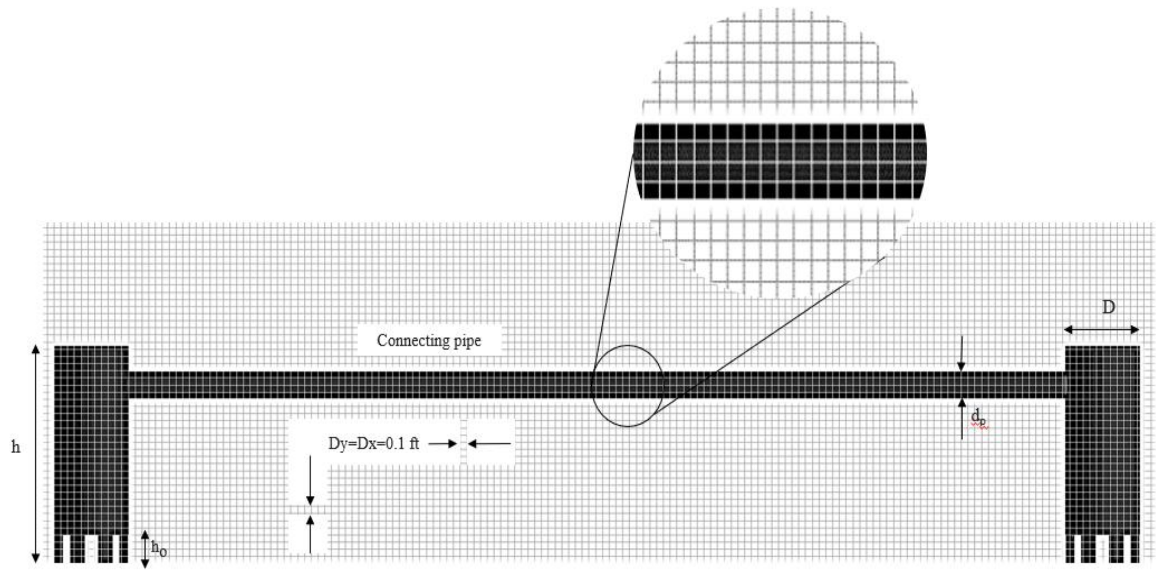

Figure 31: SOWC Meshing

4.5 Modeling and Solid Geometry

AutoCAD software was used to create a 3D solid model for the proposed device with different cylinder shapes and openings. Cylinders with two different heights were constructed. Because of the complexity and details of the SOWC shape, it is imported into Flow-3D as a baffle, so the thickness is does not playing any role in mesh size. Baffles are an infinitely thin surfaces that does not require a refined mesh to define the surface. The baffle defines the shape by blocking the flow. It also significantly helps in the computational time since a coarser grid can be chosen. The cylinders are 60.96- 91.44 cm (2 and 3 feet) tall with diameters of 15.24 cm (half a foot). Also, shapes with different openings as shown in section 4.10.1 and Table 5 are created to investigate the effects of openings.

In the computational domain, cylinders were placed far enough from the inlet boundary so there is enough space for waves to develop, pass over the structure and die out. A total computational domain of 30.48 m (100 ft) length and 1.83 m (6 ft) width and 3.66 m (12 ft) deep was considered for this purpose. The following sub-sections detail the setup required for modeling, including the general moving objects (GMO) model for modeling buoys and the Fractional-Area-Volume Ratio (FAVOR) for tracking the surface, fluid surface modeling using the Volume-of-Fluid (VOF) algorithm and boundary conditions.

4.5.1 General Moving Objects (Buoys)

In a FLOW-3D simulation, a general moving object (GMO) is a rigid body with a motion that can be either user-prescribed or dynamically coupled with fluid flow. There are six degrees of freedom or motion constraints such as a fixed axis/point. Each degree of freedom on a GMO can be restrained or prescribed under coupled motion. To track the water surface movement of the fluid inside the tubes and in the flume, floating buoys are placed on the water surface with a mass density of less than one to stay floating on the water surface. The General Moving Objects (GMO) model is used to specify rigid body motion during the simulation. All six degrees of freedom can be allowed or restricted. In this simulation, the buoys are allowed to move freely in the vertical direction to track the water surface oscillation.

4.5.2 Fluid Surface

In the Volume of Fluid (VOF) method, a value of zero is assigned to regions without fluid, and a value of one to the cells filled with fluid. Based on the percentage of the cell filled by fluid, a value between zero and one is assigned to cells. The free surface is described with a 3D plane dependent on the neighboring cells and the fraction of water in each one. The VOF method determines the free surface with respect to time and location, allowing the planes to adjust as the water surface changes (Johnson and Savage, 2001).

4.5.3 Boundary Conditions

Boundary conditions are critical parts of numerical simulations. The boundary conditions that were used for the numerical simulations are indicated in Figure 32. The sidewalls (y-direction) are defined as symmetry boundaries; the top boundary (z-max) as a pressure boundary with atmospheric pressure equal to one atmosphere (2116 lbf/ft^2); the bottom boundary as a wall (W); the left upstream inlet side (x-min) as a wave boundary (WV) (Figure 33 a); and the downstream (x-max) as an outflow (O) with a non-moving wave absorbing layer (Figure 33 d) to prevent wave reflections back into the model. A wall boundary condition is a rigid surface with fluid velocities at that boundary set at zero. It is a no-slip condition with no wall shear stresses. Free-slip means as surfaces having zero tangential stresses. Symmetry boundary conditions (S) are a free-slip condition that mirror everything. An outflow boundary condition (B.C) guarantees smooth steady flows pass across the boundary by allowing the flow to come back in the domain. The wave absorber dampen the fluid fluctuation due to the wave before exiting the domain. This is done to keep the water surface level constant. A pressure boundary condition (P) is defined as stagnation in top boundaries (z-max). In this boundary, fluid can pass out but nothing can come back in and pressure set to atmospheric absolute pressure. A wave boundary is based on linear wave theory and assumes waves with specified length, depth, height and period enter the simulation domain from the boundary, which is mentioned in-detail in follows.

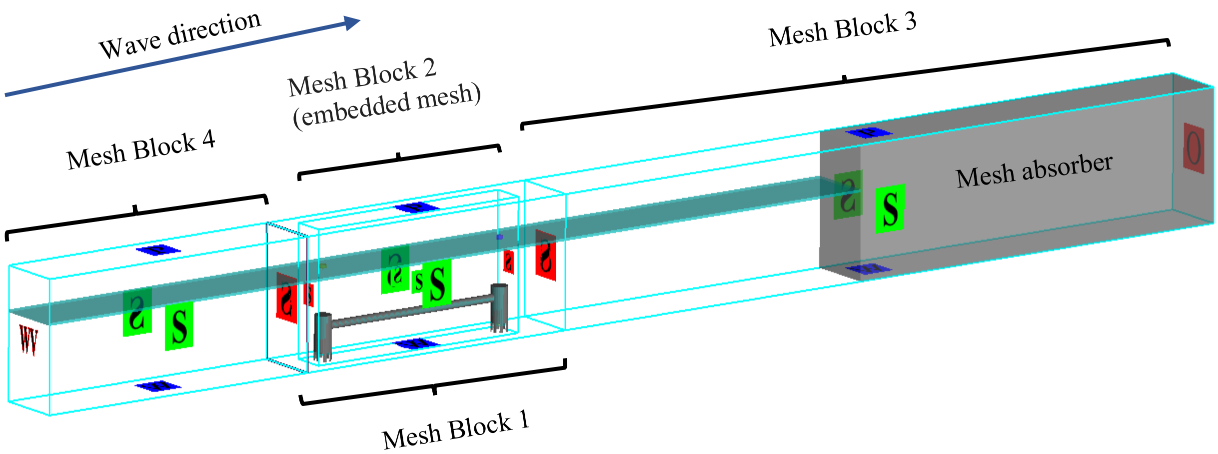

Figure 32: Boundary conditions for each mesh block

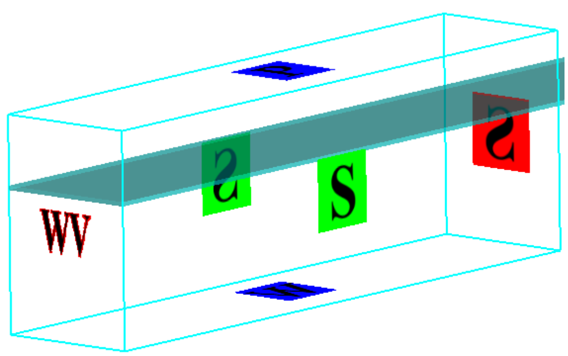

(a) Mesh block 4

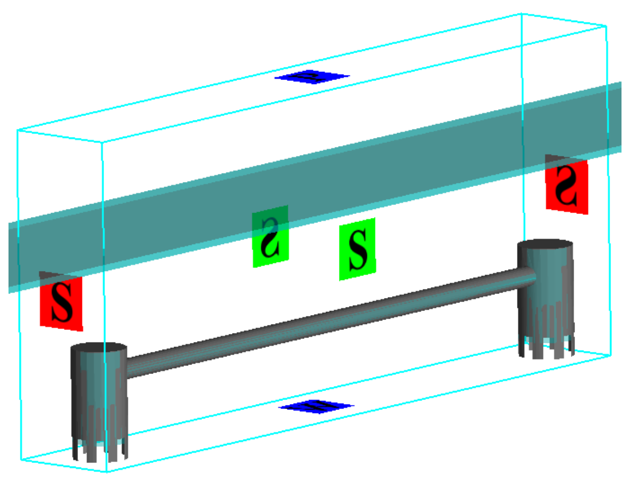

(b) Mesh block 2 (embedded mesh)

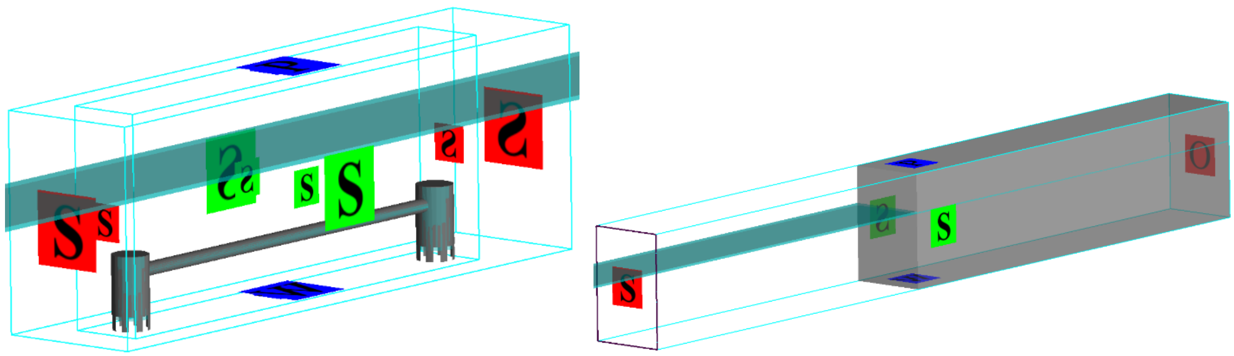

(c) Mesh block 1 (d) Mesh block 3

Figure 33: Details of boundary condition for each mesh blocks (a) mesh block 4. (b) mesh block 2-embedded mesh. (c) mesh block 1. (d) mesh block 3.

4.5.3.1 Wave Absorbing Layer at Open Boundary

In numerical simulation propagated waves need to be artificially dampened out in order to reduce the wave reflection and prevent the accumulation of the fluid in the domain. For long simulated test durations, the accumulation of water due to reflected waves back into the model may cause a significant deviation from the initial water level. In this regard, an absorbing sponge layer and absorbing boundary condition can be used.

The absorbing layer or sponge layer method is a technique to reduce the reflection of waves and dampening them. The absorbing layer is a region with additional damping characteristic to dissipate wave before it reaches the outflow boundary.

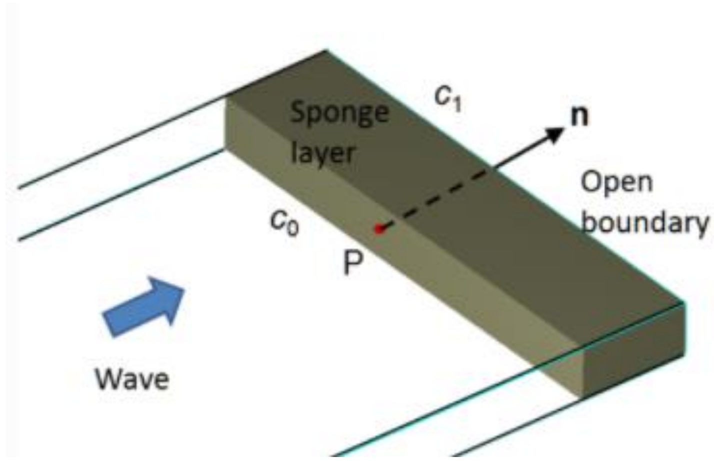

Figure 34: Wave absorbing layer (FLOW-3D user manual, 2021).

While sponge layer is completely open to fluid flow. Damping coefficients can be applied as a constant or varied value inside the absorbing layer. In the varied damping version, the damping coefficient increases linearly with distance from the starting side of the absorbing layer in the downstream direction (FLOW-3D user manual, 2021). The damping coefficient C is evaluated by

$$C = C_0 + S * \frac{C_1 - C_0}{d} \tag{32}$$

- C_0 and C_1 are damping coefficient at the start and end side of the sponge layer.
- S is the distance in downstream direction of the sponge layer
- d is the thickness of the layer in downstream direction.

Choosing the absorbing boundary type will connect the wave absorbing sponge layer component within the computational domain to the boundary face in which the wave-absorbing boundary condition is applied. A minimum length of one wavelength is recommended by the software for the sponge layer component of the wave absorber. (Flow3D user manual, 2021).

4.6 Linear and Stokes Wave Simulation

Different linear waves with varied amplitude and period are considered for this study. There are several types of waves that can be numerically generated including Linear, Stokes (Fenton's 5th order theory), Stokes and Cnoidal (Fourier series method), Solitary and Random. "Stokes and Cnoidal" waves in this study are used to generate waves. The reason for not using linear waves is the restriction and warning for big waves in the software. The assumption for linear or small amplitude waves is that the amplitude of waves compared to the mean water depth and wavelength are relatively small. So, to model waves with large amplitudes "Stokes and Cnoidal" theory is recommended. As it is shown in Figure 35, using a linear wave boundary gives a warning, which is the software recommendation to use another wave theory. However, it does not mean that linear wave theory is wrong but to use it with caution.

```
***********************************************
            warning
Xmin mesh boundary for block    1
Wave amplitude times wave number =    1.571E-01
The upper limit for linear wave is    2.000E-02
Wave is nonlinear
Recommend Stokes wave or Fourier Series method
***********************************************
```

Figure 35: Flow3D warning for using linear wave with big wave height

The Linear and Stokes waves are very similar. In linear waves, the input parameters are wave amplitude, wave period and mean fluid depth. In the Stokes model, the inputs are wavelength and mean fluid depth. Defining the wavelength for the software increases the accuracy of the simulation since the wavelength can be fixed exactly at twice the cylinders distance. But if only the period is defined as per Linear waves, the software calculates the wavelength and it might not be the exact wavelength as desired. Figure 36 and Figure 37 show the differences between linear and stokes waves. In each simulation, a wave travels from left to right in a body of water with a constant depth and approaches a wave absorbing component to damp the waves to prevent waves from reflecting back from the boundary.

A 3D simulation is required for this study because a 2D simulation is not sufficient for modeling of the OWC shape and wave refraction effects. Also, in the Y-direction (perpendicular direction of the approaching waves), the computational domain needs to be wide enough to allow the water to pass around the obstacle without any sidewall interference. For this purpose, the width of the domain is considered 4 times the SOWC diameter. This effectively creates a valid 3D model that has a minimum computational domain. For each wave, the wavelength was calculated and the distance between the SOWCs set at half of a wavelength. The SOWCs were drawn in CAD and connected with a pipe. For each simulation, the whole system was imported into Flow-3D as an STL file. Four buoys were placed inside and above each cylinder to obtain water surface oscillation. The buoys were constraint to move only in the vertical direction. A minimum run time of 30 sec was used for all simulations.

The Flow-3D simulations are set up as follows. Water with the density of 1000 kg/m^3 (1.94 slug/ft^3) was specified as an incompressible fluid with a free surface interface with a gravitational constant of 9.81 m/s^2 (32.2 ft/s^2) in the negative z-direction. The Renormalized

Group model was used as the turbulence model. The RNG model covers a wide range of turbulent flow conditions and is well suited for oscillation flow.

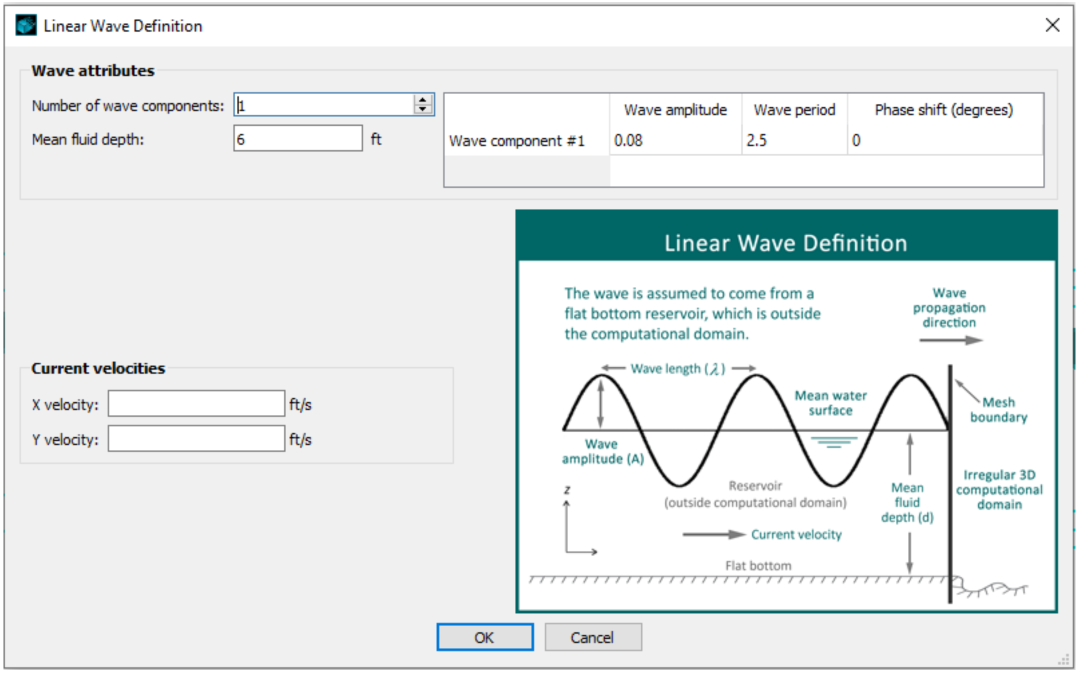

Figure 36: Linear waves settings in Flow3D

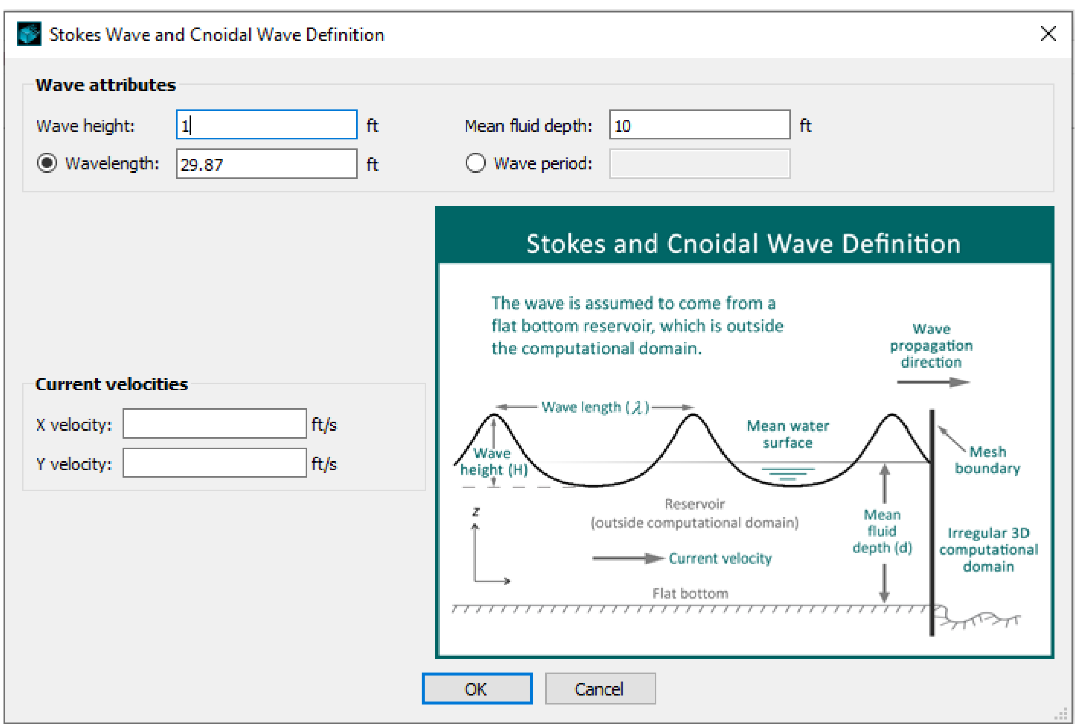

Figure 37: Stokes waves settings in Flow3D

4.7 Initial Fluid

The flow domain is initialized with a mean water depth. An initial fluid needs to be defined the same as the mean water depth in wave boundary condition. Also, to simulate entrapped air, the fluid inside the cylinder need to be removed. In this regard, the inside shape of the SOWCs was drawn in CAD and imported as a STL file to software in initial fluid section and used to remove the fluid. Figure 38 shows the fluid removed from the SOWCs (green region).

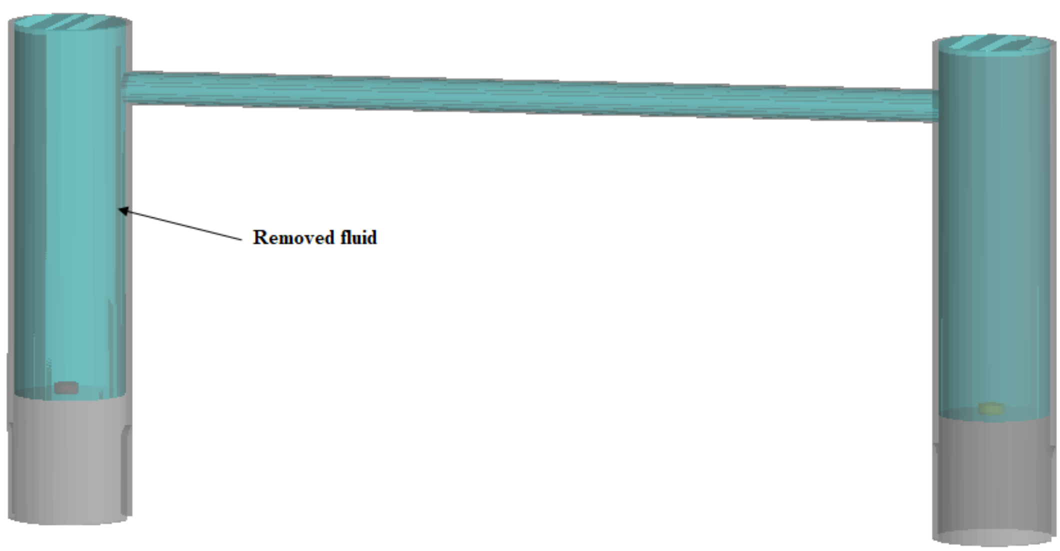

Figure 38: Removed fluid section

4.8 Numerical Results

Computational Fluid Dynamics (CFD) and a small-scale physical model were used for proof of concept. A dual 3.4 GHz quad-core computer had 64 GB RAM was used to complete the simulations. A typical simulation took between 6 to 24 hrs to complete 30s of simulated flow time. Floating buoys were placed inside and directly above each SOWC to track the water surface movement (Figure 39). The buoys were constrained to only move in the z-direction. After reaching a quasi-steady state, the raw data of buoys' motion over time was exported to a MATLAB code (Appendix E) to analyze and plot (Figure 40). The MATLAB code finds the peaks and troughs and calculate the difference between adjacent points which are the wave heights (or WSL oscillation) and average them. Small lag time can be observed in Figure 40, which were studied for other simulations and it was negligible, less than tenth of a second. A conversion rate (e) was calculated by dividing the relative movement of subsea buoys to the surface floated buoys and defined as:

$$e = a_c/a_i \tag{33}$$

where a_c is the amplitude of water surface inside the cylinders and a_i is the amplitude of incident waves.

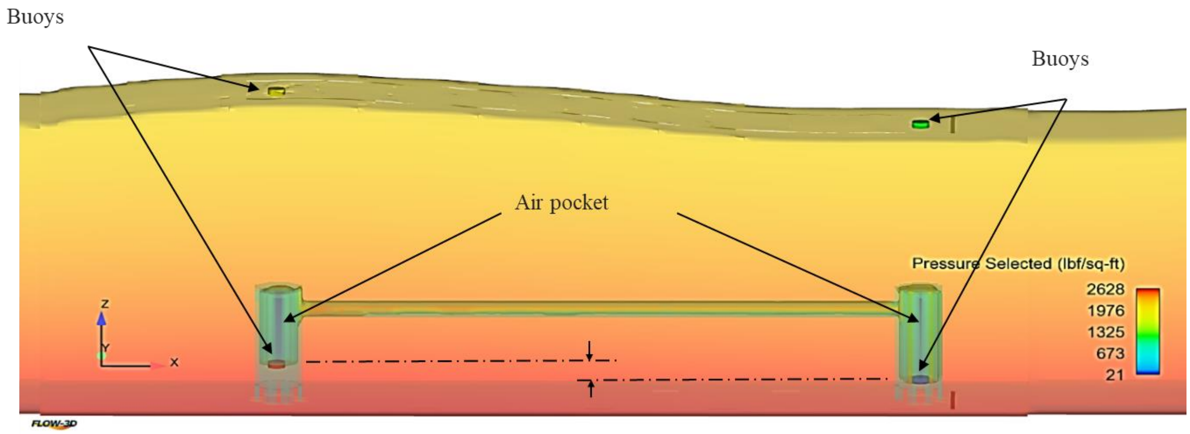

Figure 39: Simulated SOWC device (Torabi and Savage, 2019 and 2020)

The CFD modeling provided realistic results for the SOWC simulations. By increasing the relative movement of the water surface inside the cylinders to wave height, the efficiency of the device increases.

Table 4 shows the 17 different simulations with the model variables of d, L, H, L. The generated wave parameters (T, L), dimensionless relative depth (d/gT^2), and average conversion rate of left and right subsea buoys and total average are also shown. The diameter of the cylinders was set at 15.24 cm (0.5 ft) and the height were 60.96, 91.44 cm (2 or 3 ft); mentioned in Table 4. The opening at the bottom was a labyrinth shape. Test No#6 in Table 4 has the highest conversion rate of 82% and test no#11 has the lowest of 30%. The reason is the shallow relative depth; by increasing the depth the conversion rate would decrease which is observable by the downward trending line in Figure 41. Figure 41 shows the dimensionless relative depth parameter (d/gT^2) versus the average conversion rate of the buoys. The results of Table 4 indicate that the SOWC device is located in an intermediate water depth ($0.05<d/L<0.5$). It shows a correlation of $R^2=0.96$ between relative depth and conversion rate in the intermediate water depth.

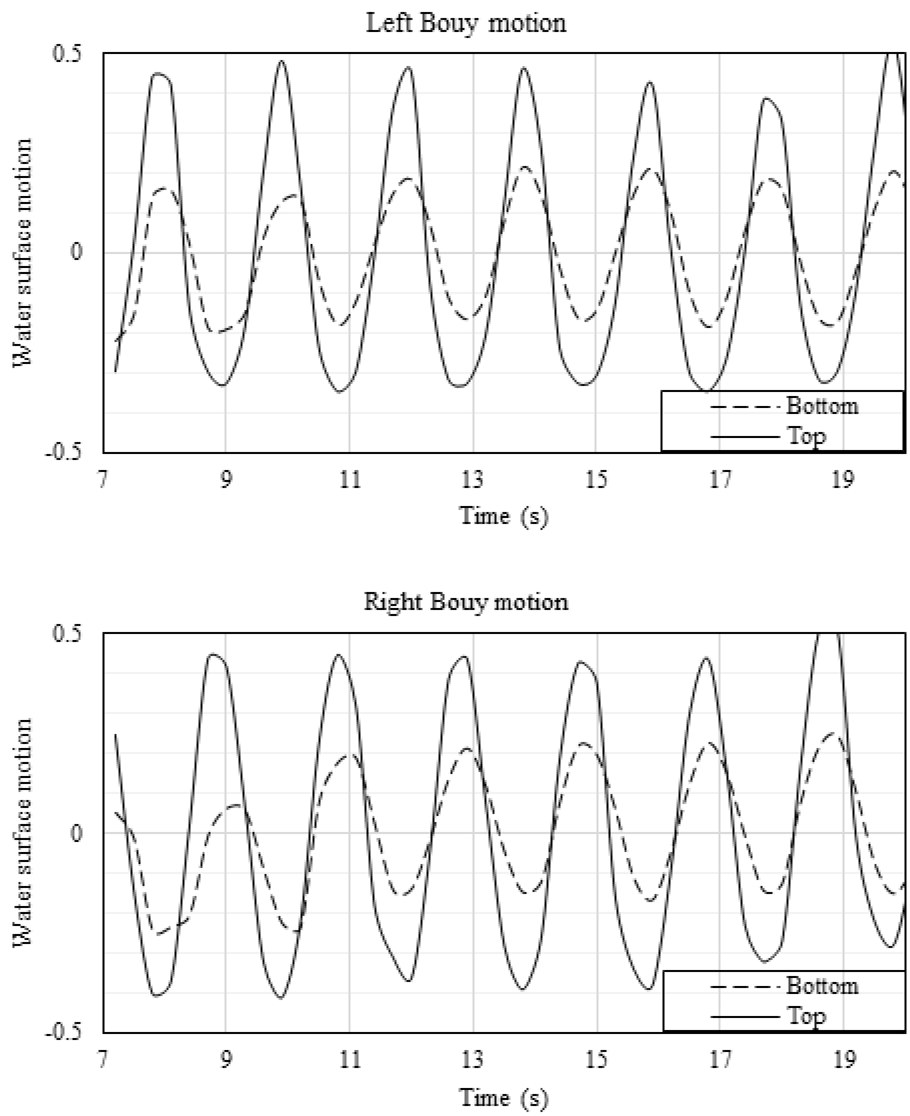

Figure 40: Analysis of buoy motion to water surface motion

Table 4: Numerical Result analysis of the tests

Test #	Cylinder height, h (m)	Water depth, d (m)	Period, T (sec)	Wave length, L (m)	d/L	d/gT^2	Left Buoy	Right Buoy	Ave
1	0.61	1.22	1.75	4.48	0.272	0.041	55.3%	58.6%	57.0%
2	0.61	1.22	2.00	5.51	0.221	0.031	61.4%	65.2%	63.3%
3	0.61	1.22	2.25	6.53	0.187	0.025	65.9%	70.7%	68.3%
4	0.61	1.22	2.50	7.51	0.162	0.020	74.6%	75.5%	75.0%
5	0.61	1.22	2.75	8.48	0.144	0.016	80.0%	75.6%	77.8%
6	0.61	1.22	3.00	9.43	0.129	0.014	85.1%	79.0%	82.1%

7	0.61	1.52	2.00	5.8	0.263	0.039	47.6%	51.0%	49.3%
8	0.61	1.83	2.00	5.98	0.306	0.047	42.6%	42.5%	42.5%
9	0.61	2.13	2.00	6.01	0.350	0.054	39.6%	40.2%	39.9%
10	0.61	2.44	2.00	6.16	0.396	0.062	32.8%	31.1%	32.0%
11	0.91	1.83	1.75	4.71	0.388	0.061	29.8%	30.2%	30.0%
12	0.91	1.83	2.00	5.98	0.306	0.047	41.0%	46.0%	43.5%
13	0.91	1.83	2.25	7.26	0.252	0.037	50.6%	53.4%	52.0%
14	0.91	1.83	2.50	8.52	0.215	0.030	63.0%	61.0%	62.0%
15	0.91	1.83	2.75	9.76	0.187	0.025	70.0%	74.0%	72.0%
16	0.91	1.83	3.00	10.97	0.167	0.021	78.0%	82%	80.0%
17	0.91	2.44	2.50	9.1	0.268	0.040	52.0%	48.0%	50.0%

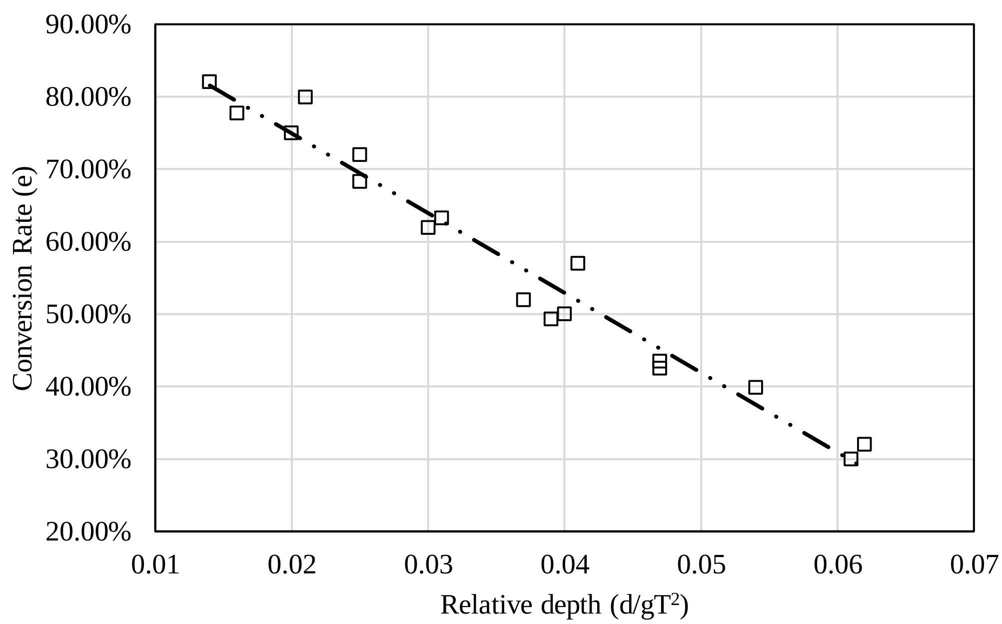

Figure 41: Relative depth to efficiency graph for numerical tests

4.8.1 Conversion Rate Improvement

One of the goals for the proposed device is to maximize the conversion rate. In this section, the effect of varying bottom openings of the SOWC cylinders is numerically investigated. Thirty-two different numerical simulations were completed. Stokes-Cnoidal waves were used with varying the wave heights, wavelengths and depths. Five different general shapes were used to investigate the effects of the SOWC's bottom opening on the conversion rate of the devices. The test configurations are shown in Table 4 with the results. Configuration #1 has a labyrinth shape with eight small openings at the bottom. The openings are rectangular in shape, spaced at a rotation of 21^{o} which gives a total open area of 46.7%.

Configuration #2 has eight opening slots which with a spacing of 32^{o}, with 71.1% of open area. Configuration #3 has a 50% opening but the opening is located only on seaside. Configuration #4 has two openings in the flow direction and has a total of 42.1% opening and the last configuration has 100% opening.

Table 5: Wave conditions for each configuration and the conversion rate

Test #	Configuration	Shape	d (m)	L (m)	H (cm)	H calc (cm)	H buoy (cm)	e %
1	#1		1.83	8.53	15.2	14.3	11.0	77%
2			1.68	8.53	15.2	14.8	12.4	84%
3			1.52	8.53	15.2	14.8	12.6	85%
4			1.83	6.10	15.2	12.2	7.2	59%
5			1.83	4.71	30.5	24.5	7.0	29%
6			1.83	5.98	30.5	23.8	11.4	48%
7			1.83	7.26	30.5	27.2	13.8	51%
8			1.83	8.52	4.9	4.9	3.4	70%
9			1.83	9.76	30.5	27.9	20.2	73%
10			1.68	8.53	7.6	7.3	5.7	78%
11			1.52	8.53	7.6	8.1	6.4	79%
12	#2		1.83	8.53	15.2	14.1	11.4	81%
13			1.68	8.53	15.2	14.8	11.4	77%
14			1.52	8.53	15.2	15.1	12.5	83%
15			1.83	6.10	15.2	12.5	8.9	71%
16			1.52	8.53	7.6	8.0	6.1	76%
17	#3		1.83	8.53	15.2	14.0	11.7	84%
18			1.68	8.53	15.2	14.8	12.7	87%
19			1.52	8.53	15.2	14.6	14.5	99%
20			1.83	6.10	15.2	13.2	10.4	79%

21			1.52	8.53	7.6	7.6	6.3	82%
22	#4		1.83	8.53	15.2	14.5	11.1	77%
23			1.68	8.53	15.2	14.7	12.0	82%
24			1.52	8.53	15.2	14.7	12.2	83%
25			1.83	9.75	15.2	13.5	10.2	75%
26			1.83	6.10	15.2	12.8	8.6	68%
27			1.52	8.53	7.6	8.1	6.3	78%
28	#5	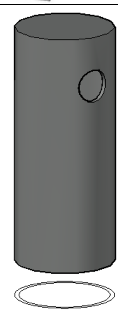	1.83	8.53	15.2	14.0	10.3	73%
29			1.68	8.53	15.2	14.4	12.0	83%
30			1.52	8.53	15.2	14.6	12.1	83%
31			1.83	6.10	15.2	11.9	9.7	81%
32			1.52	8.53	7.6	7.9	6.6	84%

As noted, Table 5 indicates the conversion rate of 5 different shapes versus depth, wavelength and wave height. In this table “d” indicates depth, “L” indicates wave length, “H” shows the input wave height and “H calc" shows the obtained wave height. “H buoy” shows the obtained wave height oscillation inside the cylinders and the “e%” is the conversion rate which is the ratio of H buoy over H calc.

Results show, generally for each shape, by increasing the depth the conversion rate decreases because of the decrease in water particle movements in deeper water, and by decreasing the wave height in a constant depth, the conversion rate decreases. The following results also can be drawn:

- Configuration #2 improved the conversion rate because of the increase in the open area comparing to configuration #1.
- In configuration #3, half of the bottom part is open and the other half is close which drastically increases the conversion rate. And has the best conversion rate among all the shapes. The opening is on the seaside and the closed half area is on the lee side. This configuration captures the translational velocity of the waves and ramps water up into cylinders thereby increase the wave motion. The cons for this shape are the low stability and the potential for entrapping debris and sedimentation inside.
- Configuration #4 produces results similar to #3. The only benefit for this shape is prevention from sedimentation and capturing debris because it is open and the flow can go through.
- The last configuration is completely open from every direction, in the prototype it will have four legs which help to sit on the bed. The results also confirm that by decreasing the depth the conversion rate increases.

Figure 42 shows that by increasing the depth at the same wavelength the conversion rate decreases and by increasing the wavelength the conversion rate increases. Comparing tests # 3, 14, 19, 24 and 30 which is for the same wave condition with a depth of 1.52 m (5ft), a wavelength of 8.53 m (28ft) and wave height of 15.24 cm (0.5 ft), indicated the conversion rate can be improved up to 15%.

Figure 43 shows the relative depth versus conversion rate for different configurations. The graph also verifies previous results and indicates that configuration #3 has the highest conversion rate among the others. 17 previous tests in Table 4 were plotted in this graph, the data are in line with Conf 1.

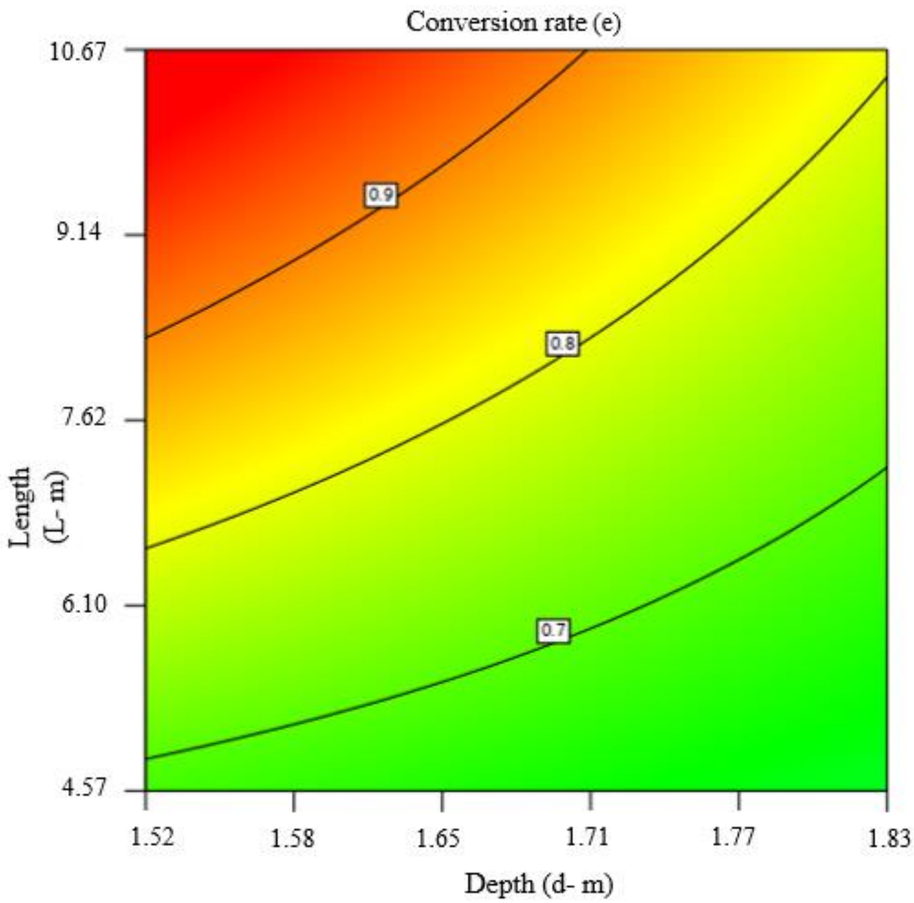

Figure 42: The average conversion rate for depth versus length

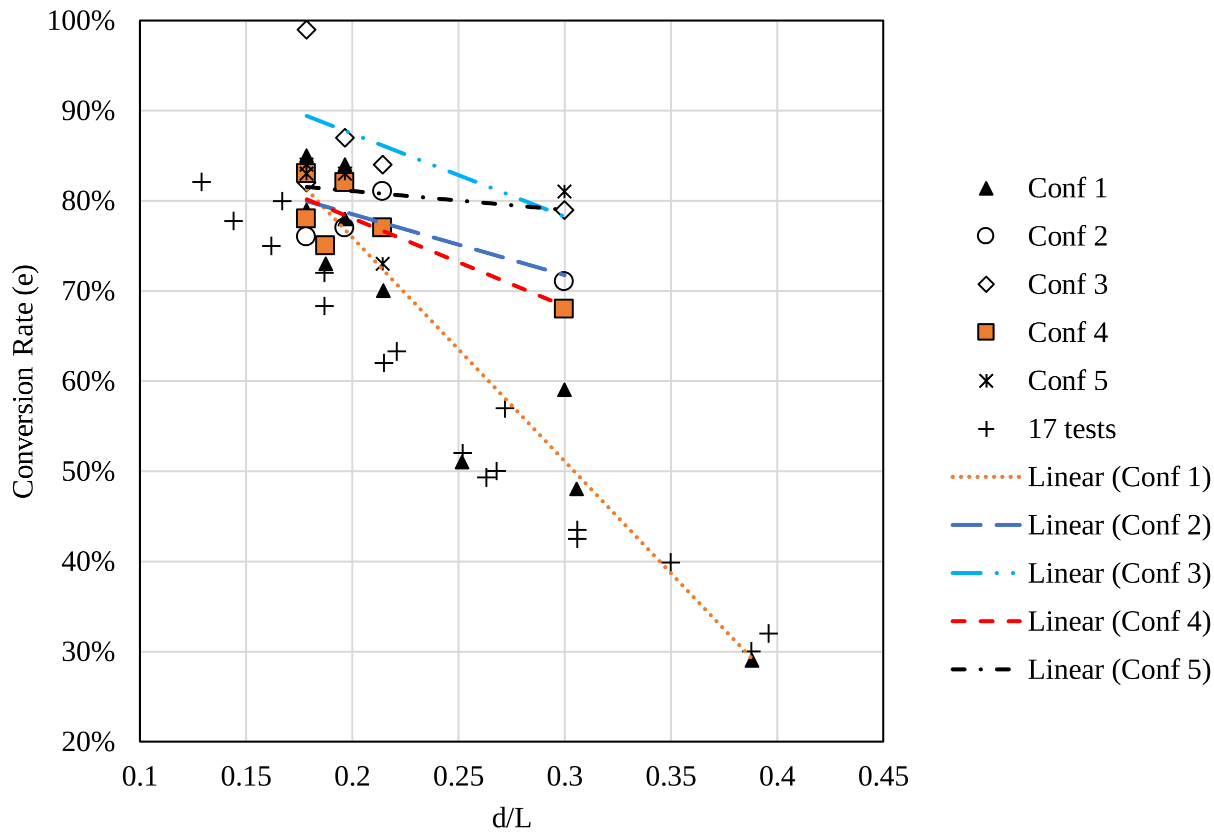

Figure 43: Comparing relative depth vs. conversion rate for different configuration

CHAPTER 5. EXPERIMENTAL TESTS

Experimental testing provided physical data to compare with the numerical modeling. Three pairs of SOWCs were constructed at a model scale of 5.08 cm (2-inch), 7.62 cm (3-inch) and 10.16 cm (4-inch). Each SOWC had a common height of 8-inches. The SOWC inlet openings were varied to measure the entrance effect on the conversion efficiency. Figure 44 provides a simple view of each of the configurations.

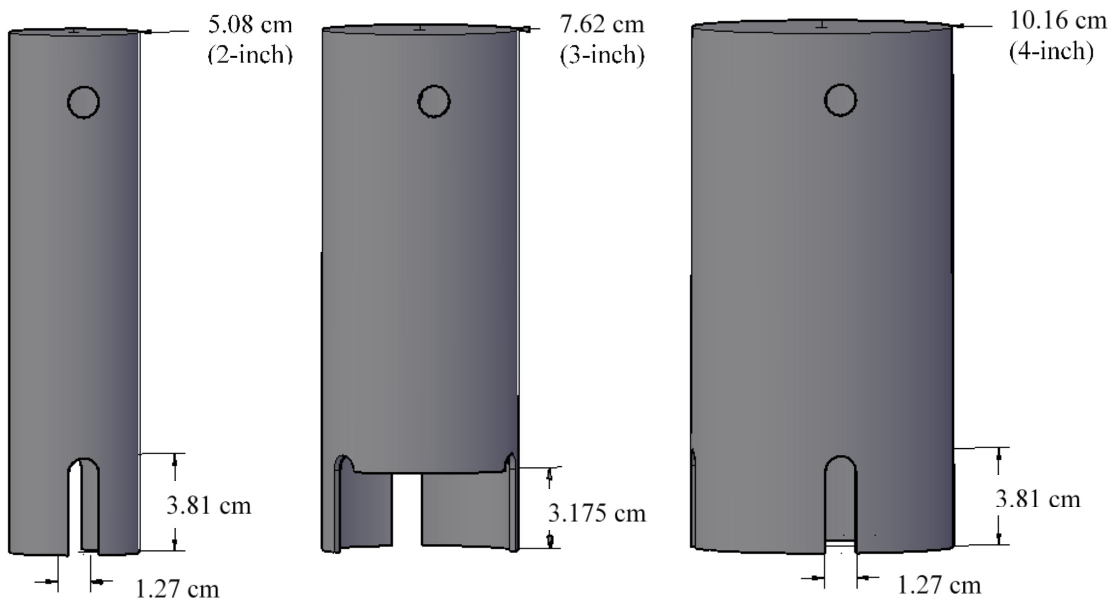

Figure 44: SOWC cylinders

Two labs with different flumes were options for completing the physical testing at Idaho State University. A 30.48 cm (1ft) deep x 30.48 cm (1ft) wide x 4.88 m (16ft) long flume is located in the physical science building. It is equipped with a flap motion bottom-hinged paddle that can generate different regular waves with different length and wave height. The flume is tiltable and can have positive or negative slopes. Another flume is located in the ERC water resource lab. The tiltable flume's original dimensions are 45.72 cm (1.5 ft) deep x 121.92 cm (4 ft) wide x 9.15 m (30 ft) long. Effort were taken to modify and upgrade the ERC flume, however due to budget and time constraints, physical testing was completed in the smaller flume. The efforts to upgrade the ERC flume are documented in section 5.1 and will provide an improved facility for future testing.

5.1 ERC Laboratory Facilities

The relatively new water resources lab in the ERC has approximately 278.7 m^2 (3000 sq. ft) of space to complete physical modeling. The lab includes the 121.92 cm (4 ft) wide flume with a water supply pump. The pump is part of a recirculating flow loop with an approximate 4500 gpm capacity. A reservoir is available with a capacity of approximately 20,000 gal.

5.1.1 Flume

The 9.15 m (30 ft) flume has the capability to test a variety of different experiments and models. However, the ability to test waves is limited by the 18-inch depth. To make the flume more conducive wave experiments, a design was developed to increase the depth to 4 ft by adding additional sidewalls inside of the flume. A steel support structure was designed and built to support the sidewalls from the lateral fluid forces (Figure 45). The support structure was attached to the body of the flume to make the extended walls an integral part of the flume. The sidewall extensions consist of 8 sheets of marine plywood with 3 sheets of plexiglass for viewing. The sidewalls extensions were placed inside of the existing side walls, attached by bolts to the frame and sealed (Figure 46) using silicone around the sides and bottom. An independent structure was designed for the motor and paddle to minimize the transferring of vibrations to the flume.

Figure 45: Sidewalls support

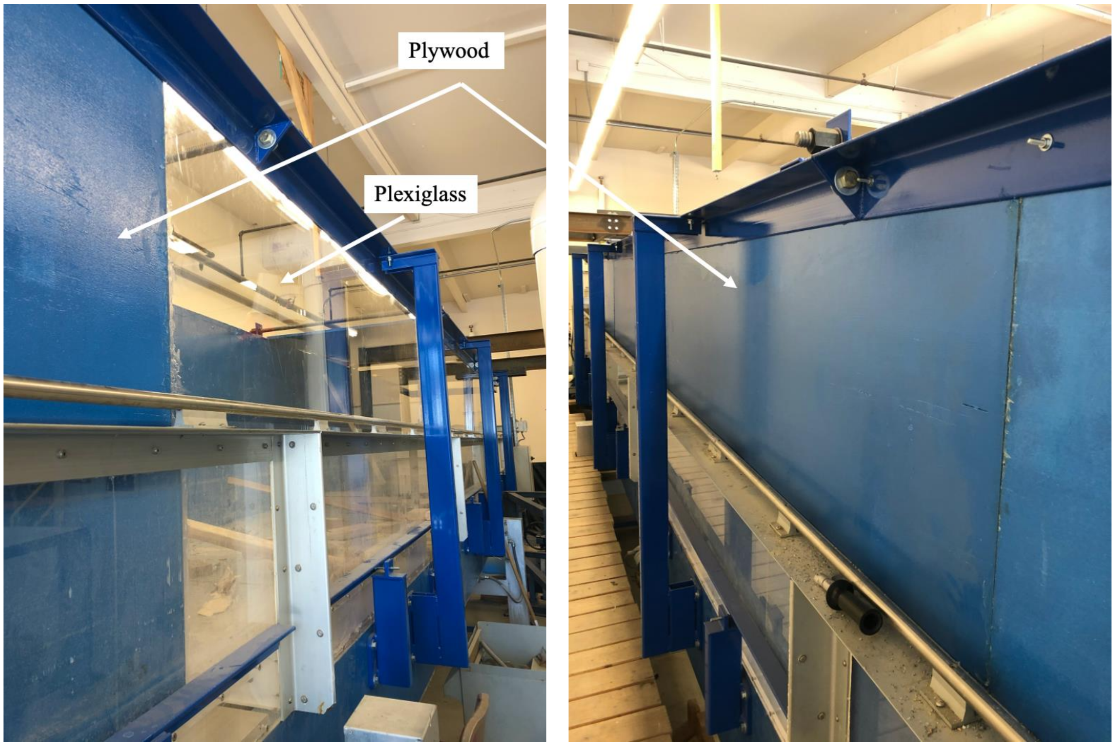

Figure 46: ERC Flume

5.1.2 Motor

To create a wave, a wave generator device is required. This device including a paddle, motor, ball screw, and a coupler. The coupler is the connection between the motor and the ball screw. The ball screw is connected to the paddle that then moves the water creating waves. The paddle is plunger type, creating waves by pushing fluid in a linear motion. In this section and the following, each one of these parts is explained.

To generate waves, design calculations showed that a 7.5 kW AC servo motor with 380V power and an AC servo driver was required (Figure 47). The structural motor is attached to the external frame thereby minimizing vibrations transferring to the flume. Figure 48 shows the schematic view of the structure and Figure 49 shows the completed frame structure. The servo motor provides accuracy of the positioning control and the ability to generate irregular waves.

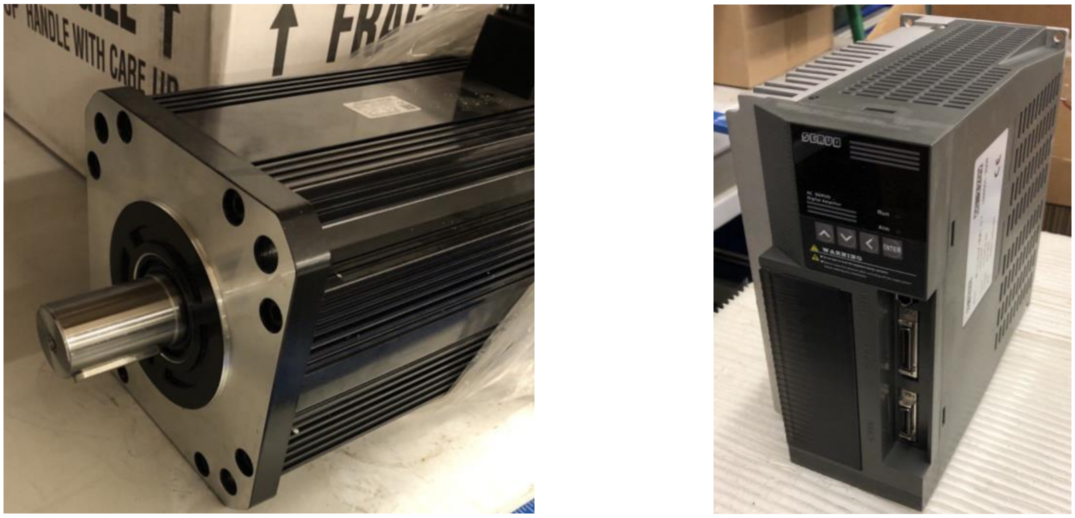

(a) (b)

Figure 47: (a) Servo motor (b) Servo driver

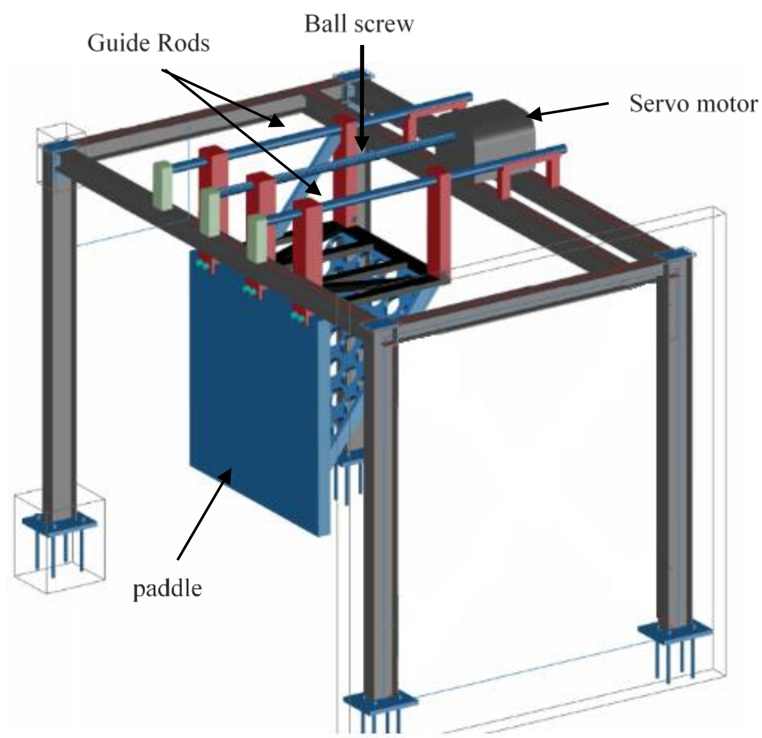

Figure 48: Schematic view of the structure and attachments

Figure 49: Completed frame structure

5.1.3 Ball Screw

The ball screw shown in Figure 48, transfers the power from the motor to the paddle. The selected ball screw has a 4 cm diameter with a 1 cm pitch. The length is 140 cm allowing for a sufficient stroke and backlash (Figure 50). Backlash is the relative axial clearance between a screw and nut without rotation of the screw or nut. The details of the selected ball screw configuration are shown in Table 6.

Table 6: Ball Screw detail

Wiper	Yes
Preload	Clearance Ball Nut
ISO Lead Accuracy Grade	T10
First End Configuration	Ezze-Mount Bearing Support
Ezze-Mount Options	Universal Double Bearing Support
Shaft Extension Option	Shaft Extension W/Keyway

End Cap Direction	Away from Thread
Second End Configuration	Ezze-Mount Bearing Support
Ezze-Mount Options	Universal Single Bearing Support
Over All Length [mm]	1400
Reference Number:	PMBS40X10R-4FW/0/T10/EK/CN/1400/0/S

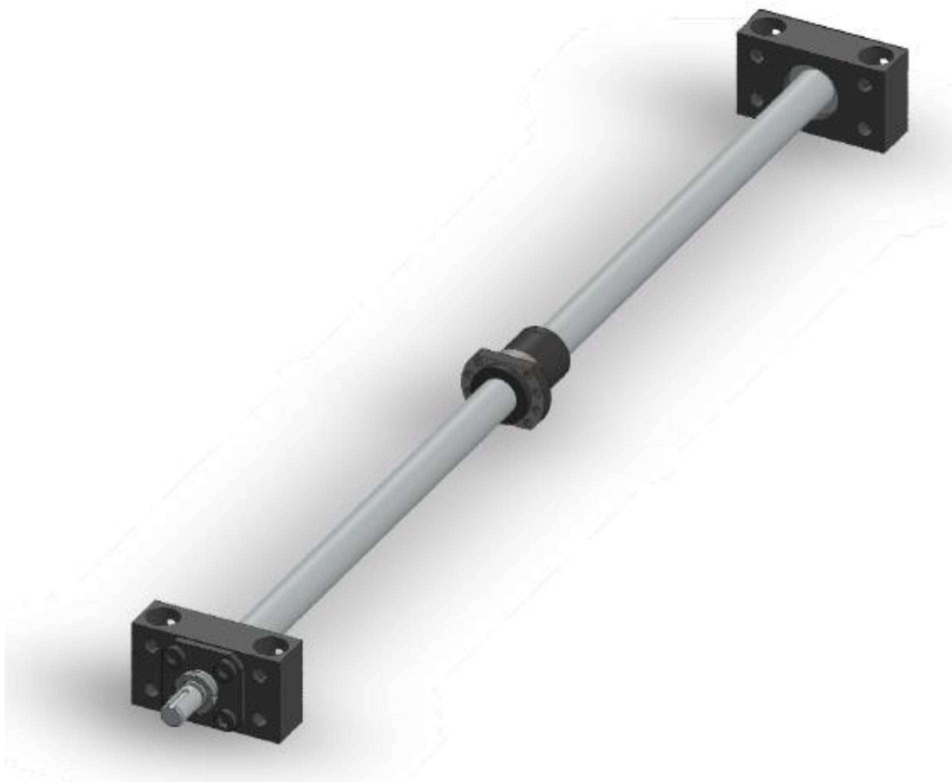

Figure 50: Ball Screw

5.1.4 Coupler

To connect the motor to the ball screw, two couplers with different jaws were purchased and used (Figure 51). Each coupler has a keyway. The keyway is a recess in the hub to receive the key and thus securely lock the components. The key within the keyway is designed to shear under extreme shear forces, thereby protecting the other components of the system. The center piece is also made from a durable composite rubber thereby reducing vibrations during starts/stops.

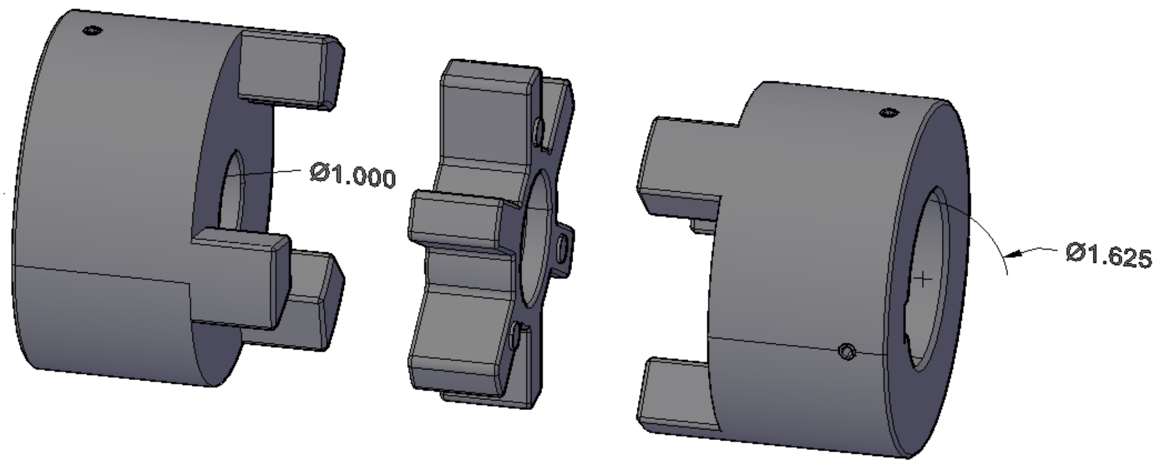

Figure 51: Coupler

5.1.5 Wave Sensor

Ocean sensors “Waves Staff” are used to measure water surface. They can be used to measure waves, tides and tank level. The physical mounting of the sensors requires no special protection from water however it should not be mounted underwater. The unit is mounted with the electronics head on the top and the staff (yellow rod) projecting down into the water. The output is a relative measurement of the height of the air-fluid interface. The cable is a weather-proof neoprene jacketed cable and it should be supported and not hang unsupported for greater than 24 in. The detail of the wave sensor is shown in Figure 52. To have accurate measurements the wave staff should be exactly vertical. The yellow part of the staff should be mounted at least 10.16 cm (4 inches) away from any metallic or grounded surface. See the detail of changing rod and other configurations in the manual (Ocean sensor system, 2020). The accuracy of the measurements can be up to a millimeter and the sensors record data every tenth of a second.

Figure 52: Wave sensor

The other required part to exchange data with a computer is Serial Communications. The Ocean Sensor Systems Wave Staff allows for data exchange and reconfiguration through RS232 communication port to a computer. For that communication, the DB9 port is used where the number refers to the number of pins (Figure 53). Only three wires are required to connect the unit to the computer. Three wires include transmit, receive and ground wires (Ocean sensor system, 2020). A synchronizer is also used as a hub to gather all the information from sensors and send it to the computer through the DB9 port (Figure 54).

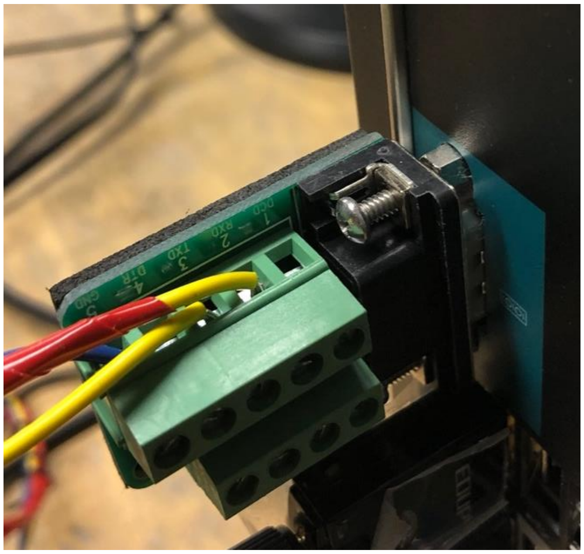

Figure 53: DB9 connector

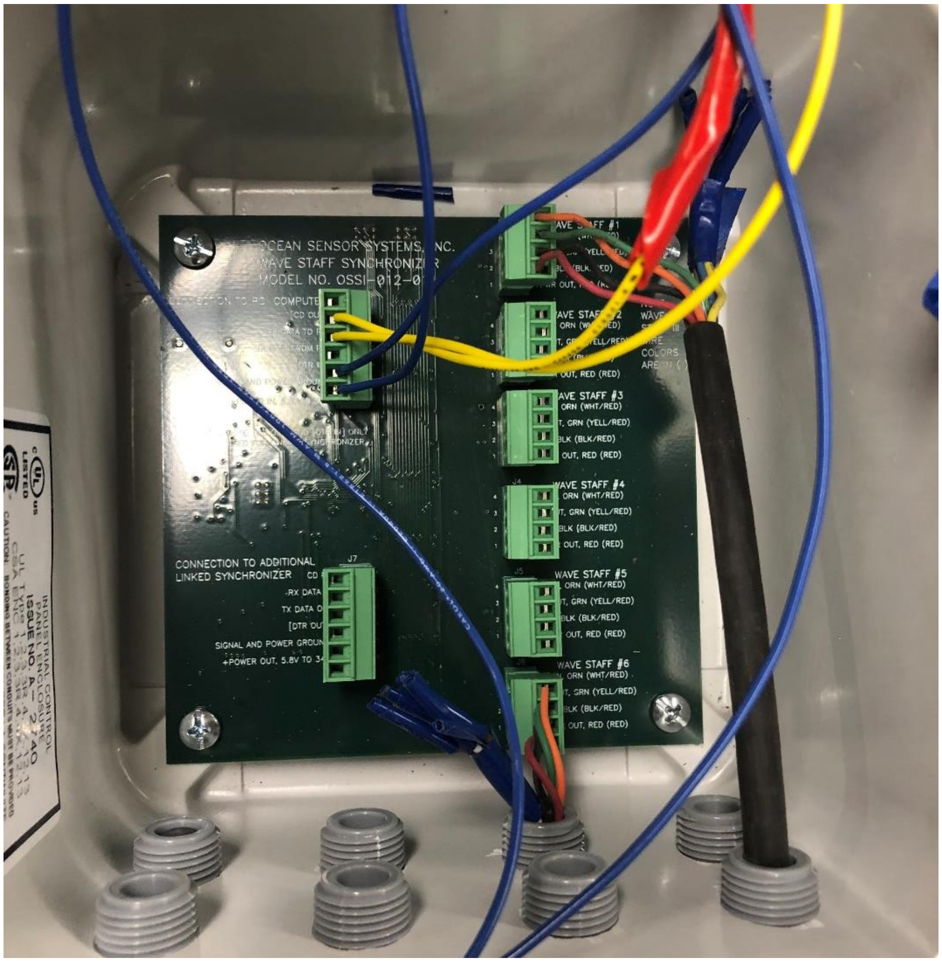

Figure 54: Synchronizer

5.1.6 Software Interface:

A software program name "Staff and Sonic Products Interface" is used to display, plot, and analyze data (Figure 55). To run the program, a "Unit Type" needs to be selected which for this project is "Wave Staff Synchronizer". In the next step, the correct "Com Port" should be selected. Finally, by putting the sensor numbers in the "Trace Device No" slots and press the Start Plotting button, the software starts to run and plot the data. In the software the oscillation can be shown in a window of 16, 64, 256 or 512 sec. By clicking on any points, the exact coordinates of the selected location can be displayed. The program is available on the Ocean Sensor Systems Web Site.

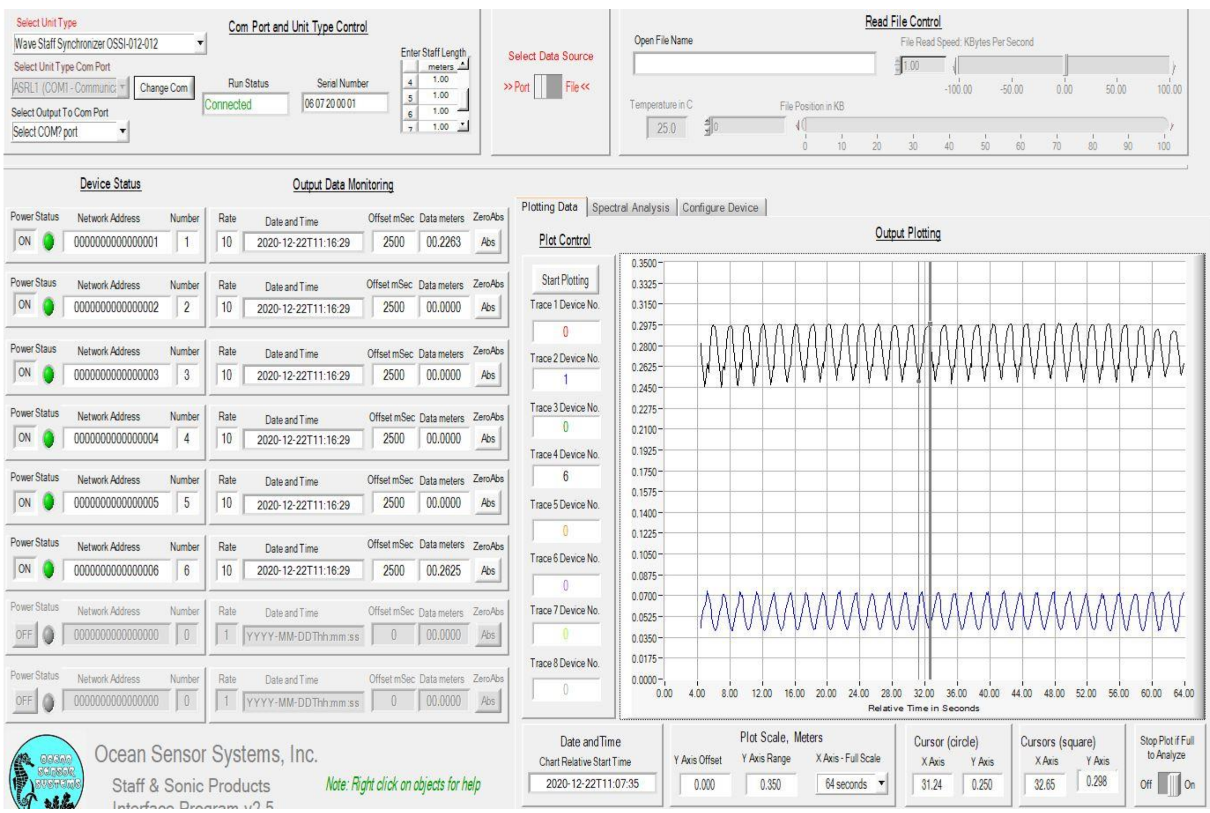

Figure 55: Wave staff software

5.2 Small Flume Lab

The physical experiments were completed in the physical science small flume lab due to a lack of time and budget to finish the ERC lab on-time. The physical science lab includes a 30.48 cm (1 ft) wide x 4.88 m (16 ft) long flume with a maximum depth of 30.48 cm (one foot) (Figure 56). The flume is equipped with a sinusoidal wave generator with the capability of making regular waves with different lengths and heights. Two wave sensors with an accuracy of 1 mm, explained in section 5.1.5, were used to measure both the wave surface and the oscillating water column in one SOWC. The sensors connected to an overhead pipe structure, allowing them to slide along the length of the flume (Figure 58 and Figure 59) at the center point. Due to the lack of a wave absorber downstream of the flume, a standing wave was created for each test. In this regard, to capture the peak and trough, the water sensors were used to identify the peak and trough and correctly locate the SOWC for each test. Two sensors were used for this project. One sensor was utilized to measure the water surface inside the SOWC cylinder. The other sensor was used to measure the wave height.

To measure the oscillating water surface inside the cylinder, a hole was drilled on the top of one of the cylinders of each pair. A 1.27 cm (1/2 inch) see-through flexible hose was attached with a connection (Figure 60-a) to the hole to isolate the sensor from the surface water. A sensor was placed through the hose and into the SOWC, keeping it dry with the exception of water in the SOWC. An airtight connection using a piece of rubber and a hose clamp was placed at the top of the hose around the sensor. This was required to trap the air in the SOWC. This kept the sensor isolated and in contact with water inside the cylinder (Figure 57-b). The other wave sensor was placed in the flume (at the peak location of the waves in each test) to measure the wave height. The sensors were connected to a wave staff synchronizer (Figure 54) to record the data. The synchronizer was also connected to a computer with a serial comm port DB9 (Figure 60-b). More details of the connections are shown in the reference (Ocean sensor system, 2020).

The WEC cylinders were constructed from plexiglass and are connected together in pairs with a connecting hose. The bottom of the cylinders are open and labyrinth-shaped to let the water in and out. In each test, two cylinders were placed approximately half of the average wavelength apart and connected by a flexible 0.95 cm (three-eighth inch) hose. The initial air pocket was blown in the system using the flexible hose. The hose allows air to travel between the SOWCs as the waves move over the cylinders.

Figure 56: Small flume lab

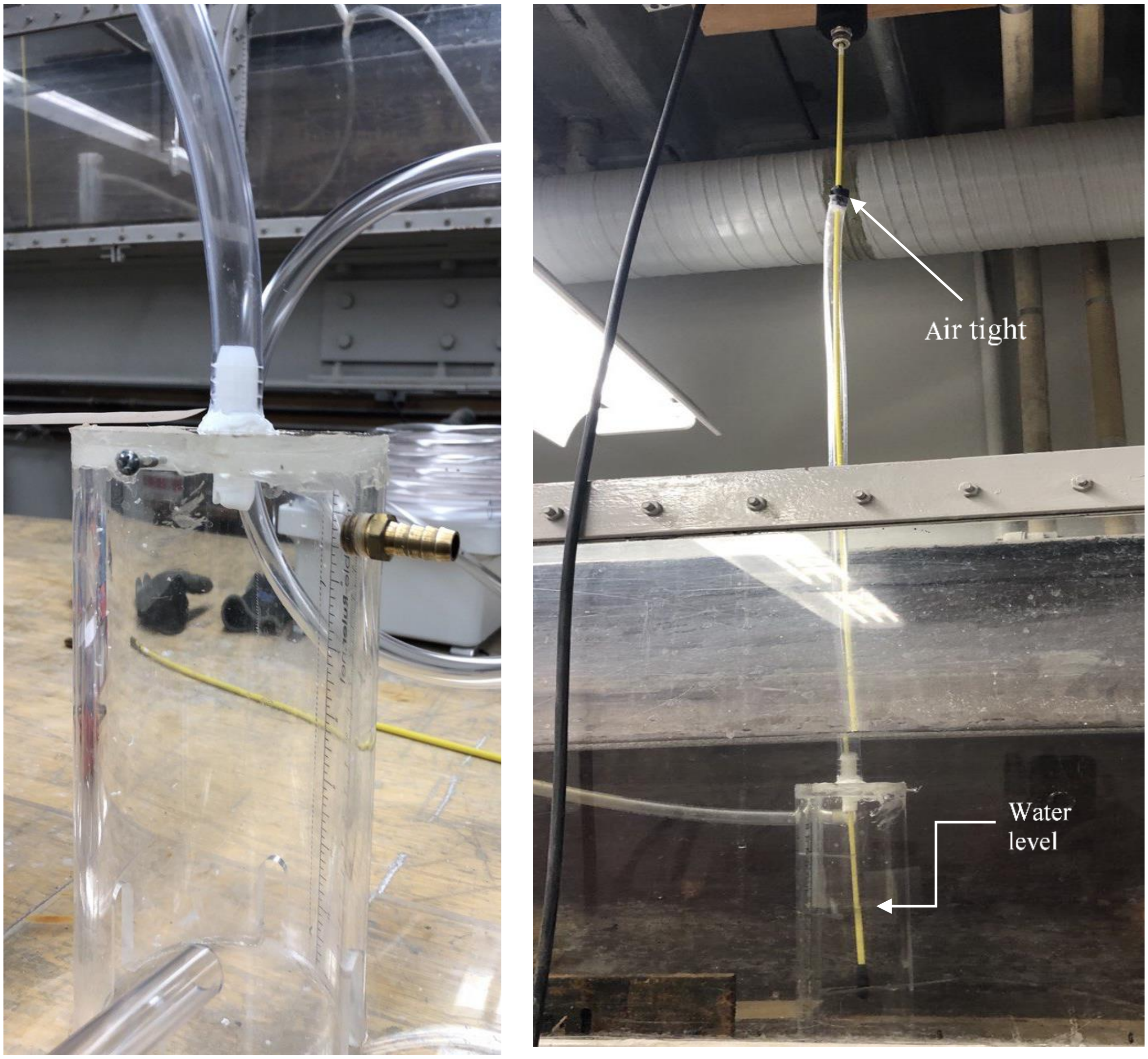

(a) (b)

Figure 57: Experimental setup (a) SOWC’s hose connections (b) Water proofing the sensor

Figure 58: Sensor guide

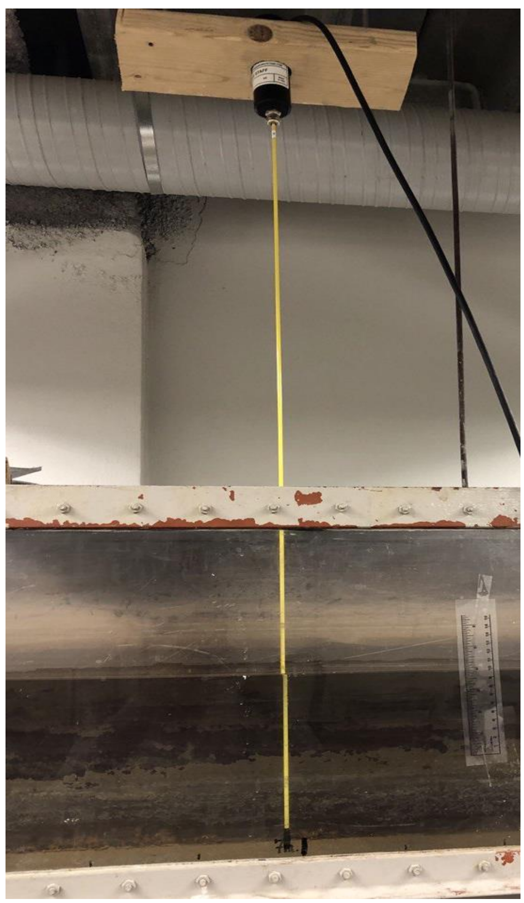

Figure 59: Wave sensor setup to measure wave height

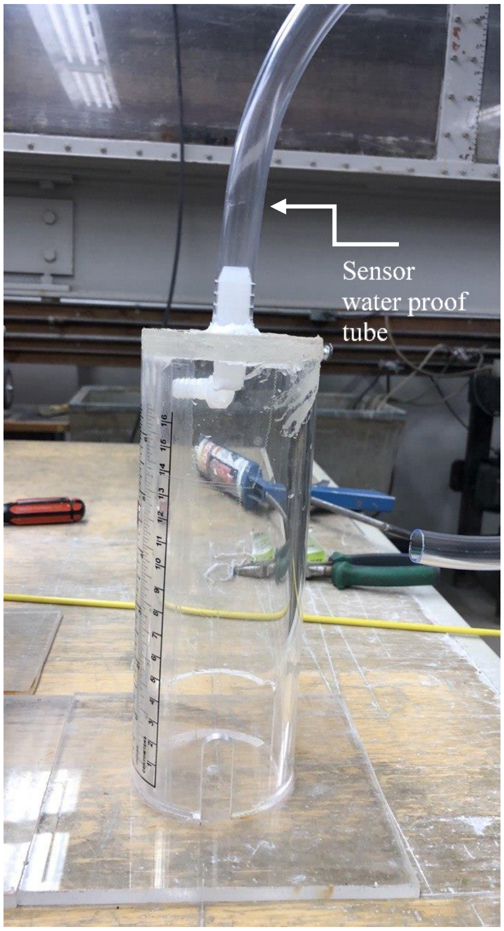

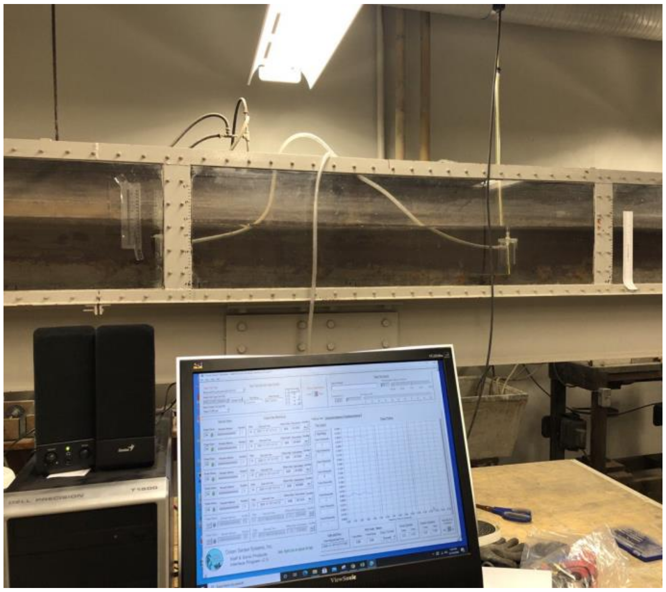

(a) (b)

Figure 60: (a) Waterproofing the sensor to measure WSL inside the cylinder (b) Computer setups for reading sensors data

5.3 Testing Methodology

The experimental tests were completed at the Idaho State University’s Physical Science small flume lab. The methodology for the experimental tests was to generate different wave heights and lengths and place cylinders half a wavelength. Different cylinders with different diameters were used to evaluate the effect of size on the measurements. For a given diameter, a water depth was set and four to five different wave periods were generated and the data for each wave period recorded. The test setup was allowed to stabilize for 5-10 minutes, before data was collected. While stabilizing the depth, sensors started to capture the oscillation of the water surfaces. As shown in Figure 55, the wave motion is plotted in real time. By clicking on each peak and trough the exact maximum and minimum weight data can be extracted. Seven or eight peaks and troughs were extracted and the differences were calculated and averaged. The difference indicates the water oscillation inside the cylinder (or wave height). To find the accuracy of this method, the raw data file for one of the tests was extracted from the software and analyzed by finding the standard deviation of wave heights. Figure 61 shows approximately 35 sec of recorded data. In this figure, peaks and troughs are separated and the wave height (difference between peaks and troughs) are calculated. The standard deviation for wave heights in this test was 0.00028 m which is insignificant.

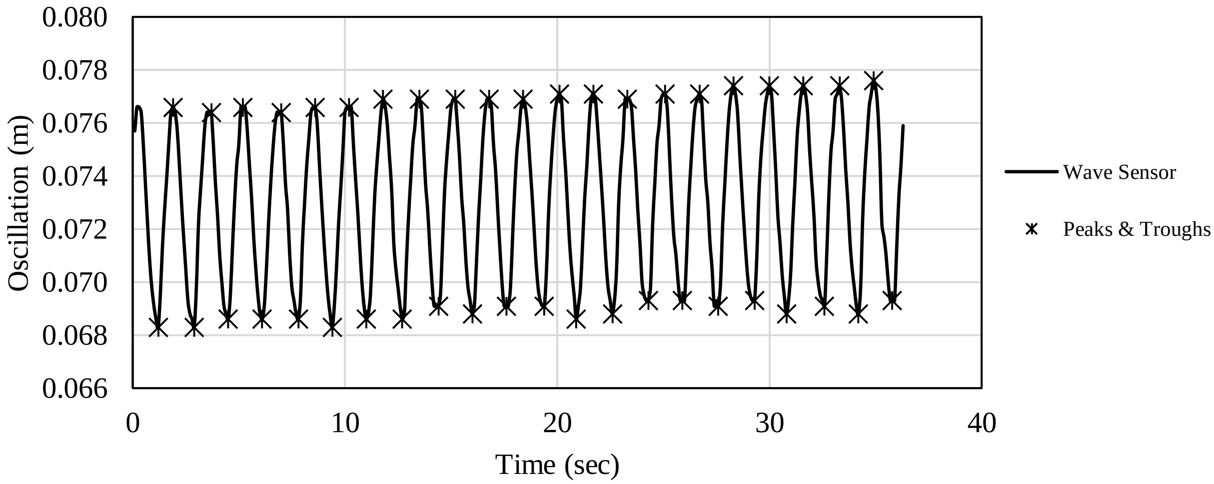

Figure 61: Wave height analysis

Test matrices including variation in wave height, wave period, water depth and three different diameters are shown in Chapter 6, Table 7.

CHAPTER 6. RESULTS AND DISCUSSION

The experimental test results are shown in Table 7. In all, eighty-four tests have been carried out for different waves, depths and geometry. The tests started with the 5.08 cm (2-inch) diameter cylinder and a water depth of 24.5 cm. For each depth, three to four waves with different period generated and water surface motion both inside the SOWC and the free surface wave motion was recorded and averaged. At that point, the depth was increased approximately one centimeter and the same tests were repeated until the depth reaches to 30.5 cm. The same process was repeated for the 7.62 (3-inch) and 10.16 cm (4-inch) SOWC cylinders. Wave heights, wavelength and the oscillation inside the cylinder (H_{inside}) were measured and conversion rate calculated. The conversion rate is defined ratio of wave oscillation inside the cylinder over the incident wave (H_{inside}/H). Additional wave-defining parameters such as relative depth (d/L, d/gT^2) and wave steepness (H/L) were computed. The experimental tests results are shown in Table 7.

Table 7: Experimental tests results

Test #	d (cm)	T (sec)	L/2 (cm)	H (cm)	d/L	H/L	d/gT^2	H_{inside} (cm)	D (cm)	Conversion Rate (e)
1	24.5	2.00	166	1.4	0.074	0.017	0.006	1.25	5.08	89.3%
2	24.5	1.68	120	4.7	0.102	0.078	0.009	3.80	5.08	80.9%
3	24.5	1.44	120	1.8	0.102	0.030	0.012	1.50	5.08	83.3%
4	24.5	1.22	71	1.8	0.173	0.051	0.017	1.50	5.08	83.3%
5	25.5	2.10	153	1.6	0.083	0.021	0.006	1.40	5.08	87.5%
6	25.5	1.64	113	3.5	0.113	0.062	0.010	3.20	5.08	91.4%
7	25.5	1.42	127	3.8	0.100	0.060	0.013	3.20	5.08	84.2%
8	25.5	1.05	69	4.0	0.185	0.116	0.024	2.80	5.08	70.0%
9	25.5	1.18	73	1.9	0.175	0.052	0.019	1.50	5.08	78.9%
10	26.5	1.18	86	2.6	0.154	0.060	0.019	1.80	5.08	69.2%
11	26.5	1.44	100	1.8	0.133	0.036	0.013	1.50	5.08	83.3%
12	26.5	1.63	117	1.5	0.113	0.026	0.010	1.30	5.08	86.7%

Test #	d (cm)	T (sec)	L/2 (cm)	H (cm)	d/L	H/L	d/gT^2	H_{inside} (cm)	D (cm)	Conversion Rate (e)
13	26.5	2.04	155	1.3	0.085	0.017	0.006	1.20	5.08	92.3%
14	27.5	2.04	166	3.1	0.083	0.037	0.007	2.90	5.08	93.5%
15	27.5	1.67	104	4.9	0.132	0.094	0.010	4.10	5.08	83.7%
16	27.5	1.22	89	2.2	0.154	0.049	0.019	1.50	5.08	68.2%
17	27.5	0.98	64	4.0	0.215	0.125	0.029	2.50	5.08	62.5%
18	28.5	0.98	64	2.6	0.223	0.081	0.030	1.70	5.08	65.4%
19	28.5	1.20	95	3.0	0.150	0.063	0.020	2.10	5.08	70.0%
20	28.5	1.67	118	1.8	0.121	0.031	0.010	1.50	5.08	83.3%
21	29.5	2.10	163	2.6	0.090	0.032	0.007	2.10	5.08	80.8%
22	29.5	1.60	123	6.0	0.120	0.098	0.012	5.00	5.08	83.3%
23	29.5	1.00	71	11.0	0.208	0.310	0.030	6.50	5.08	59.1%
24	30.5	2.30	168	5.0	0.091	0.060	0.006	4.50	5.08	90.0%
25	30.5	1.30	94	10.0	0.162	0.213	0.018	7.70	5.08	77.0%
26	30.5	1.53	139	8.0	0.110	0.115	0.013	6.80	5.08	85.0%
27	24.5	1.63	121	1.2	0.101	0.020	0.009	0.90	7.62	75.0%
28	24.5	1.51	121	1.2	0.101	0.020	0.011	1.10	7.62	91.7%
29	24.5	1.32	100	1.8	0.123	0.036	0.014	1.50	7.62	83.3%
30	25.5	1.32	94	1.8	0.136	0.038	0.015	1.30	7.62	72.2%
31	25.5	1.22	84	1.5	0.152	0.036	0.017	1.10	7.62	73.3%
32	25.5	1.10	91	1.4	0.140	0.031	0.022	0.90	7.62	64.3%
33	25.5	1.50	108	2.4	0.118	0.044	0.012	2.20	7.62	91.7%
34	25.5	1.32	108	1.9	0.118	0.035	0.015	1.40	7.62	73.7%
35	26.5	1.32	109	2.2	0.122	0.040	0.016	1.50	7.62	68.2%
36	26.5	1.72	118	1.5	0.112	0.025	0.009	1.20	7.62	80.0%
37	27.5	1.72	138	1.4	0.100	0.020	0.009	1.20	7.62	85.7%
38	27.5	1.35	118	1.8	0.117	0.031	0.015	1.10	7.62	61.1%
39	27.5	1.25	92	2.8	0.149	0.061	0.018	2.00	7.62	71.4%
40	27.5	1.14	85	5.5	0.162	0.129	0.022	2.60	7.62	47.3%
41	27.5	0.98	76	6.3	0.181	0.166	0.029	2.40	7.62	38.1%
42	28.5	2.40	168	3.5	0.085	0.042	0.005	3.00	7.62	85.7%
43	28.5	1.95	150	1.4	0.095	0.019	0.008	1.10	7.62	78.6%
44	28.5	1.57	135	3.1	0.106	0.046	0.012	2.40	7.62	77.4%
45	28.5	1.30	134	4.3	0.106	0.064	0.017	2.40	7.62	55.8%
46	28.5	1.15	80	2.4	0.178	0.060	0.022	1.10	7.62	45.8%
47	29.5	1.15	93	5.0	0.159	0.108	0.023	2.10	7.62	42.0%
48	29.5	1.30	94	6.0	0.157	0.128	0.018	3.20	7.62	53.3%
49	29.5	1.50	94	2.6	0.157	0.055	0.013	1.60	7.62	61.5%
50	29.5	2.10	170	4.1	0.087	0.048	0.007	3.60	7.62	87.8%

Test #	d (cm)	T (sec)	L/2 (cm)	H (cm)	d/L	H/L	d/gT^2	H_{inside} (cm)	D (cm)	Conversion Rate (e)
51	29.5	2.40	168	2.7	0.088	0.032	0.005	2.40	7.62	88.9%
52	30.5	1.93	168	1.7	0.091	0.020	0.008	1.40	7.62	82.4%
53	30.5	1.58	125	3.3	0.122	0.053	0.012	2.55	7.62	77.3%
54	30.5	2.00	168	6.0	0.091	0.071	0.008	4.30	7.62	71.7%
55	30.5	2.10	168	1.7	0.091	0.020	0.007	1.40	7.62	82.4%
56	30.5	1.50	122	1.9	0.125	0.031	0.014	1.20	10.16	63.2%
57	30.5	1.83	122	2.8	0.125	0.046	0.009	1.90	10.16	67.9%
58	30.5	1.05	88	3.4	0.173	0.077	0.028	1.40	10.16	41.2%
59	30.5	2.04	160	4.8	0.095	0.060	0.007	3.20	10.16	66.7%
60	27.5	2.00	172	1.3	0.080	0.015	0.007	1.00	10.16	76.9%
61	27.5	1.70	160	1.0	0.086	0.013	0.010	0.70	10.16	70.0%
62	27.5	1.23	104	2.7	0.132	0.052	0.019	1.50	10.16	55.6%
63	27.5	1.08	85	4.2	0.162	0.099	0.024	1.40	10.16	33.3%
64	28.5	2.50	180	3.7	0.079	0.041	0.005	3.00	10.16	81.1%
65	28.5	1.81	132	1.5	0.108	0.023	0.009	1.10	10.16	73.3%
66	28.5	1.53	117	5.3	0.122	0.091	0.012	2.90	10.16	54.7%
67	28.5	1.26	96	1.9	0.148	0.040	0.018	0.80	10.16	42.1%
68	28.5	1.10	83	3.0	0.172	0.072	0.024	1.40	10.16	46.7%
69	29.5	1.10	83	4.5	0.178	0.108	0.025	1.60	10.16	35.6%
70	29.5	1.24	83	3.2	0.178	0.077	0.020	1.30	10.16	40.6%
71	29.5	1.97	154	2.4	0.096	0.031	0.008	1.70	10.16	70.8%
72	29.5	2.46	175	3.6	0.084	0.041	0.005	2.90	10.16	80.6%
73	25.5	2.10	177	1.9	0.072	0.021	0.006	1.20	10.16	63.2%
74	25.5	1.66	145	1.8	0.088	0.025	0.009	1.10	10.16	61.1%
75	25.5	1.40	98	2.9	0.130	0.059	0.013	1.40	10.16	48.3%
76	25.5	1.14	83	3.7	0.154	0.089	0.020	1.30	10.16	35.1%
77	26.5	1.14	83	3.9	0.160	0.094	0.021	1.60	10.16	41.0%
78	26.5	1.43	100	1.8	0.133	0.036	0.013	1.20	10.16	66.7%
79	26.5	1.20	74	1.8	0.179	0.049	0.019	0.90	10.16	50.0%
80	26.5	1.08	85	2.1	0.156	0.049	0.023	1.00	10.16	47.6%
81	24.5	1.08	78	2.0	0.157	0.051	0.021	0.90	10.16	45.0%
82	24.5	1.25	91	4.4	0.135	0.097	0.016	2.00	10.16	45.5%
83	24.5	1.50	98	1.7	0.125	0.035	0.011	1.20	10.16	70.6%
84	24.5	2.00	122	1.0	0.100	0.016	0.006	0.70	10.16	70.0%

Some general observations or correlations can be concluded from the experimental results as follows.

- Increasing the depth with the same period decreases the conversion rate.
- Increasing the wave period improved the conversion rate.
- Increasing the relative depth, decreased the conversion rate.
- Increasing the wavelength caused a higher conversion rate.
- Decreasing the SOWC diameter leads to a higher conversion rate.

To better understand the resulting experimental data, several key dimensionless water parameters such as relative depth (d/gT^2) and wave steepness (H/L) were used to plot and evaluate the correlation of the data. For Figure 62 the conversion ratio is plotted as a function of the relative depth (d/gT^2). For Figure 63 the conversion ratio is plotted as a function of the wave steepness (H/L). Both graphs include the data for three different diameters. Based on the R^2 the results, the relative depth in Figure 62 provides better correlation coefficients ranging from 0.72 to 0.85 than the wave steepness from Figure 63 that ranges from 0.35 to 0.61.

Additional observations are supported by the data in Figure 62. As mentioned above, increasing the diameter decreases the conversion rate. There are a couple of reasons for this fact. The first reason is that a small diameter will act like a rigid piston model as noted by equation (34) (Clappi et al, 2020). Smaller diameters prevent turbulence and small waves inside the cylinder. The second reason is that a bigger cylinder cannot capture the peak. If a column of water is considered above the cylinder, the Still Water Level (SWL) for that column is larger for bigger cylinders. This reduces the average wave height across the SOWC and conversely shallower troughs.

- A bigger diameter also increases the lag time, because it requires more kinetic energy for oscillation. In higher frequency waves, the oscillation inside the cylinder does not have enough time to catch up with waves and causes a decrease in the conversion rate.
- The smaller 5.08 cm (2-inch) diameter cylinders in Figure 62 have a milder slope on the regression line compared to the other diameters. The reason is because of the shorter lag time and being more responsive. In higher wave frequency, less kinetic energy is required and causes the system to be more responsive. Stated another way, the smaller the diameter, the less it is impacted by a change in the depth, the wave height or the period. On the other side, in smaller relative depth for 5.08 cm (2-inch), the data set is not much higher than the other ones because the conversion rate cannot reach 100%.
- The R^2 of data for 5.08 cm (2-inch) to 10.16 cm (4-inch) is between 72% to 84% which shows it is in good agreement with relative depth.

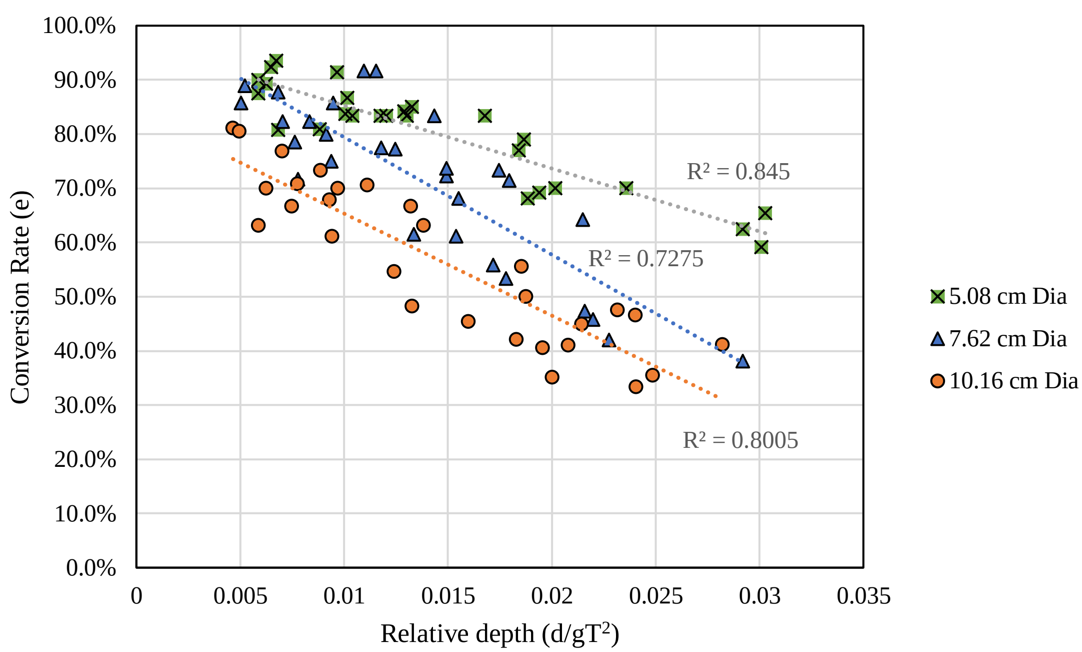

Figure 62: Conversion rate versus relative depth for different diameters

Although the second graph (Figure 63) has a relatively lower R^2, it still confirms some of the conclusions. As it is observable by increasing the wave steepness the conversion ratio decreases. The reason is that steep waves have a higher frequency, so the oscillation is not quite as responsive in higher frequencies.

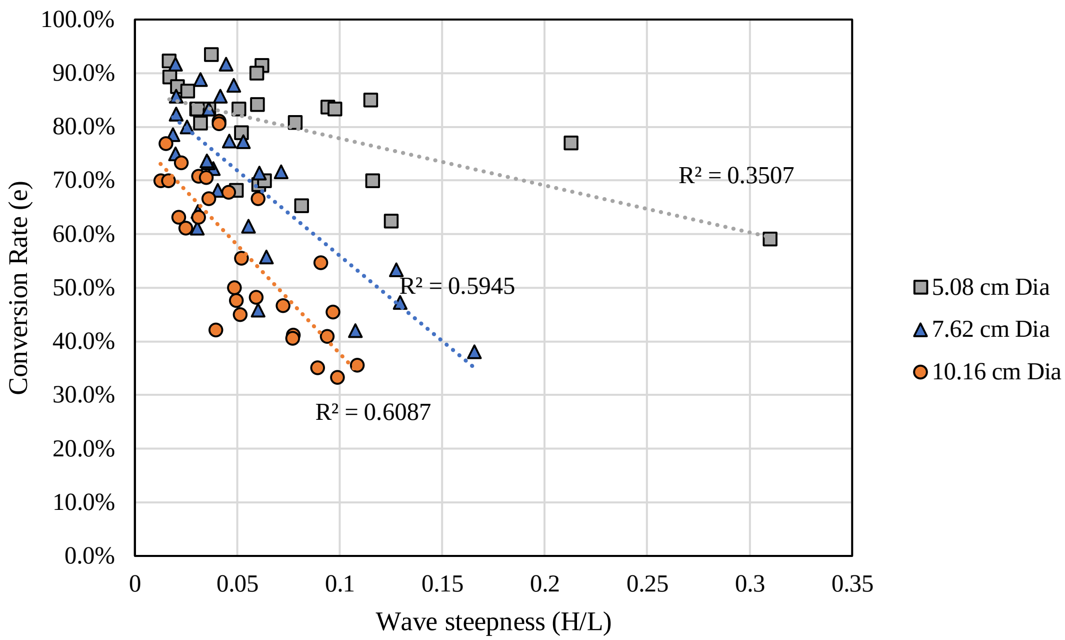

Figure 63: Conversion rate versus wave steepness for different diameters

Another parameter that was observed and measured during the experiments was the volume of entrapped air inside the cylinders. In initial tests, it was observed that by decreasing the volume of entrapped air in an experiment the efficiency improved significantly. The original thought was that the volume of trapped air can dampen the oscillation of water and increase the lag time. With this hypothesis in mind, the data was plotted to determine if this satisfies the assumption.

Figure 64 shows in 2D and 3D, changing the relative depth (d/gT^2) and amount of entrapped air versus the conversion rate. In the experiments "Air volume" axis ranges from 122 cm^3 to 892

cm^3. The axis shows the average volume of air in one cylinder. The graph shows, in smaller relative depth (d/gT^2) by changing the volume of air, the change in efficiency is not as large as in higher relative depth. Because a smaller d/gT^2 indicates a higher wave period or smaller depth, accordingly the wavelengths are longer. In that case, there is no lag time and the tube oscillation has enough time to catch up with the waves. However, in higher d/gT^2 by increasing the amount of air, the conversion rate decreases quicker. If the relative depths of 0.004 and 0.025 are compared, it can be observed that the conversion ratio changes more significantly when the relative depth is 0.025.

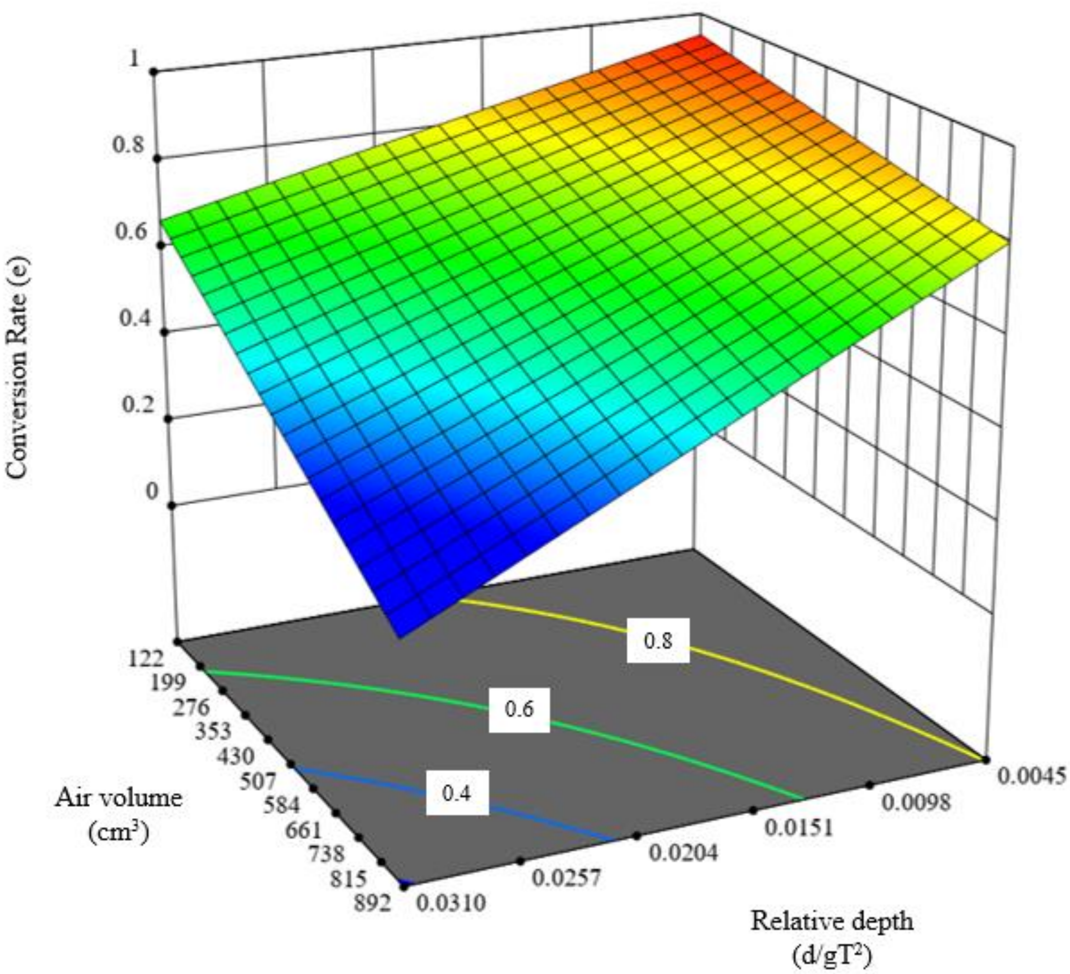

Figure 64: Graph indicates for air level

To disprove the original hypothesis that the amount of entrapped air is a significant variable, an experiment was designed. The concept of the experiment was to keep the Water Surface Level (WSL) inside the cylinder the same as the previous test but decrease the amount of air by placing a Styrofoam cylinder inside. A circular piece of Styrofoam was cut and placed at the top of the cylinder (Figure 65) removing volume of air. A hole was created at the middle of the Styrofoam to allow the sensor to pass through. Styrofoam adjacent to the hose entrance was removed to allow the air to easily flow in and out. After that, the same previous tests were repeated. Detail of result is in Appendix G.

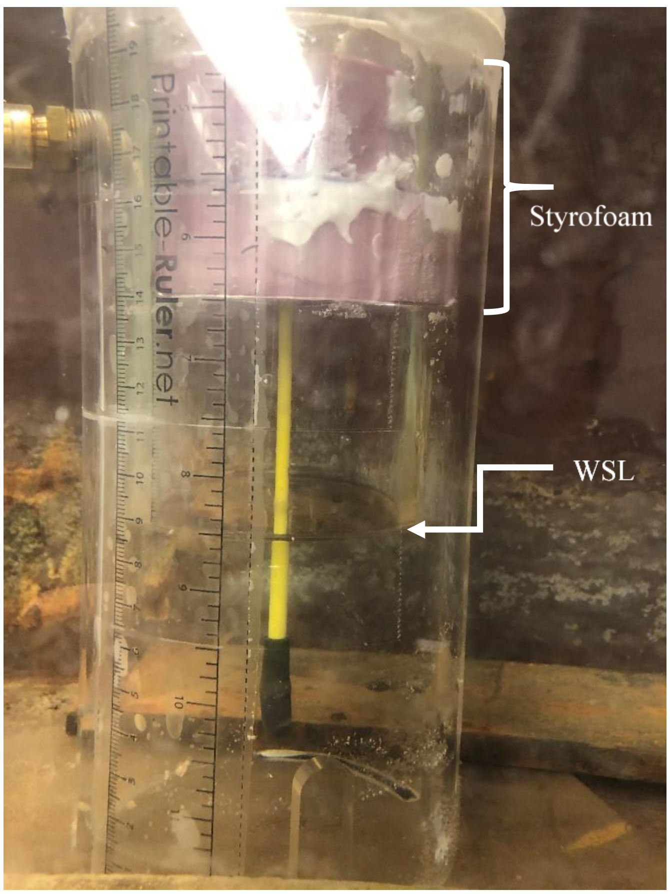

Figure 65: Cylinder with Styrofoam

Results of the Styrofoam test did not show any improvement in the conversion rate. Figure 66 shows the test results with and without the Styrofoam. As it can be observed results are in the same range and do not show any improvements. These results proved that the first assumption was wrong and the level of air is not a key factor in water oscillation inside the tube.

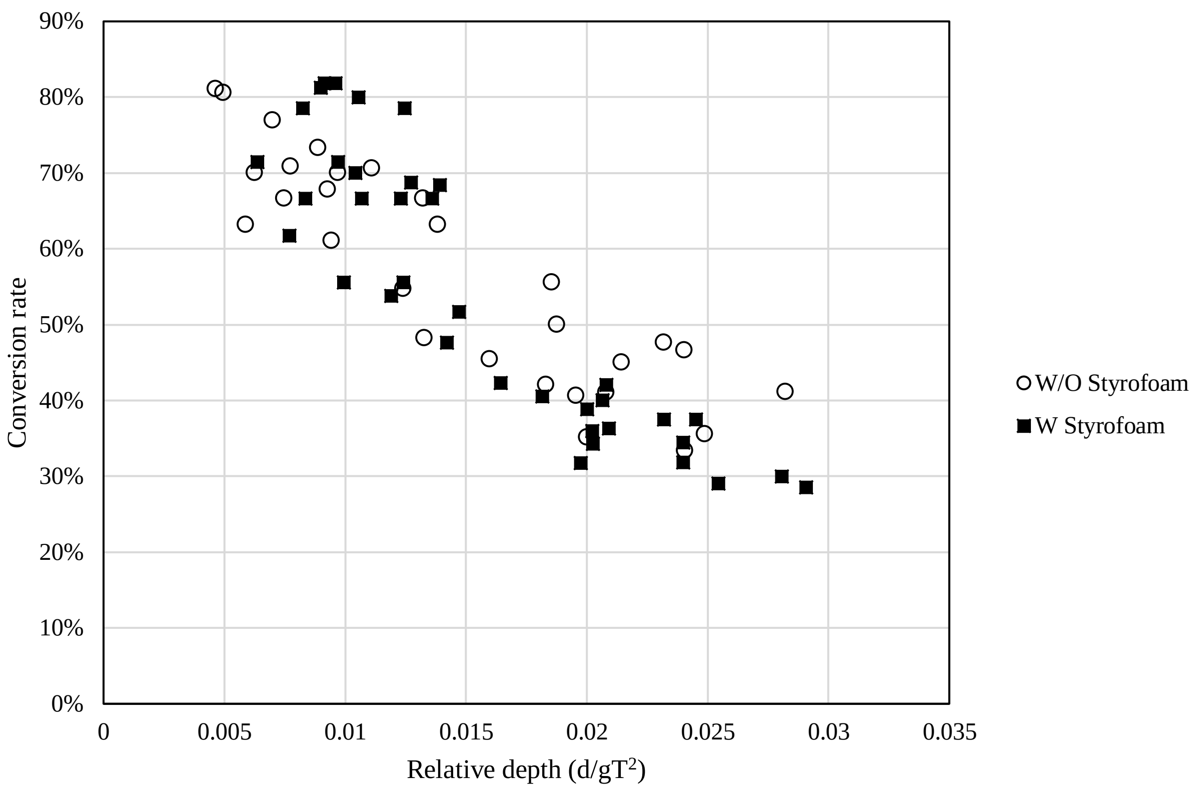

Figure 66: Experiments with and without Styrofoam

The second assumption for having different oscillation amplitude in different water surface elevations inside the cylinder was the dynamic pressure. As explained in section 2.1.4, in ocean waves, the total pressure includes hydrostatic pressure and dynamic pressure. Dynamic pressure changes in different depths. By going deeper in water, dynamic pressure decreases, up to a depth of about half a wavelength then the dynamic pressure becomes zero. But by getting closer to the surface, the dynamic pressure increases.

To prove the hypothesis that the dynamic pressure is the reason for the difference in amplitude of water oscillation inside the tube, two other tests were designed. The first test was elevating one of the cylinders within the water column to evaluate how the oscillation will change. In essence, this places the SOWC entrance higher where the dynamic pressure should have a larger effect. In each test, the conversion rate was measured with the SOWC on the flume bottom and then one of cylinders was elevated 7cm (Figure 67), and then remeasured for the conversion rate.

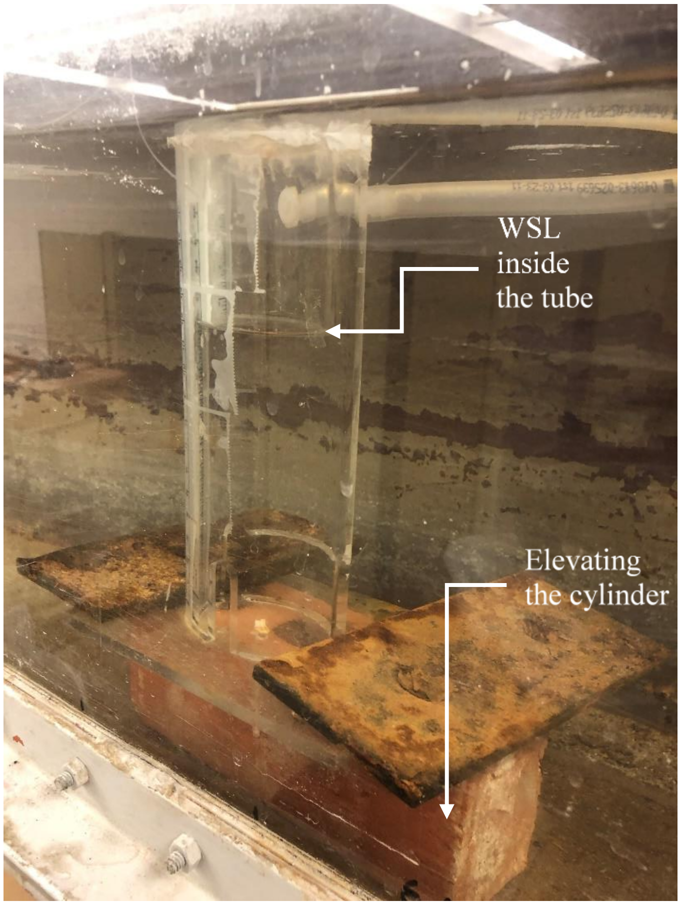

Figure 67: Elevating one cylinder

The results and comparison are shown in Table 8. The results show that the wave height inside the tube is increased by elevating the cylinder. In general, there is a one- or two-millimeter difference that makes a 5-10% improvement. Elevating one cylinder and locating it at a higher place exposes it to higher fluctuations in dynamic velocity. It verifies that an entrance closer to the surface changes the depth more than in deep water.

Table 8: Results for elevating one cylinder

d (cm)	T (sec)	H (cm)	d/gT^2	H_{inside}-elevated (cm)	H_{inside} (cm)	Difference
30.5	1.22	2.2	0.021	1.8	1.7	5.9%
30.5	1.62	2.1	0.012	2.0	1.9	5.3%
30.5	2.03	4.6	0.008	4.5	4.3	4.7%
30.5	1.58	3.7	0.012	3.0	2.9	3.4%
30.0	2.11	3.0	0.007	2.1	2.1	0.0%
30.0	1.65	1.8	0.011	1.5	1.4	7.1%
30.0	1.37	2.6	0.016	1.5	1.4	7.1%
31.0	1.60	6.1	0.012	3.8	3.5	8.6%
31.0	1.86	1.8	0.009	1.7	1.5	13.3%
31.5	2.00	5.3	0.008	4.9	4.8	2.1%
31.5	1.60	1.9	0.013	1.5	1.4	7.1%

The second experiment was placing a long tube (pipe) inside the flume from the bottom to the top above the water surface. A wave sensor was placed inside the pipe to capture surface movements inside it. Several tests were carried out by changing the draft. The draft is the distance from the bottom of the pipe to the bed of the flume. Seven different drafts were selected and the tube was held on those elevations. For each elevation, the test was repeated to find the conversion rate.

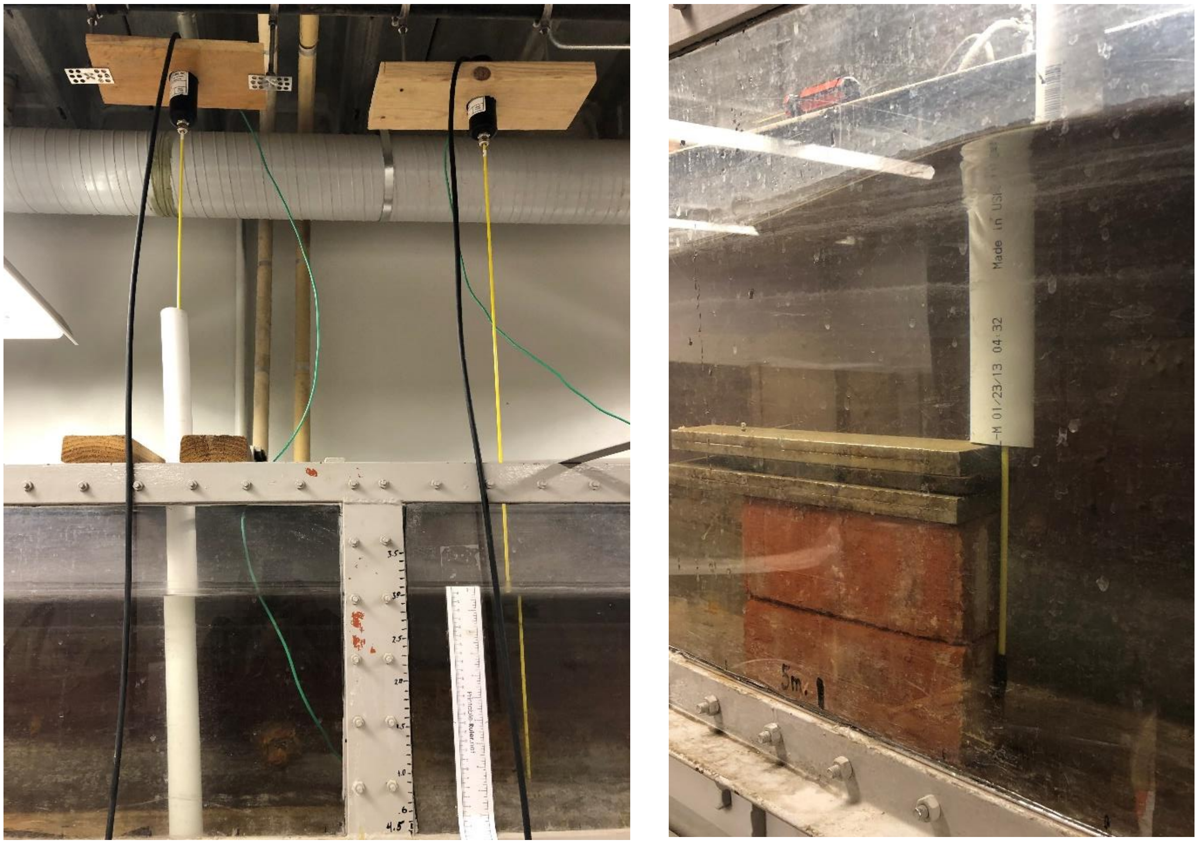

Figure 68: WSL in PVC pipe in different drafts

Interestingly it demonstrated that oscillation inside the tube can be significantly higher than the waves. Figure 68 shows the setup for the test in different elevations. Figure 69 shows the ratio of water surface oscillation inside the tube over the wave height in a different draft. Oscillation inside the tube, by increasing the draft, increases significantly and at the draft of 2.5 cm, it experienced over 13 cm amplitude, which is two times more than wave height. After that point, oscillation in the tube starts to decrease and eventually at higher drafts it reaches wave height.

The experiments were also repeated for 7.62 cm (3-inch) clear PVC pipe. The reason for the experiment was to see the effect of different diameters. Results showed the diameter plays a role and different diameters can have different oscillation amplitudes.

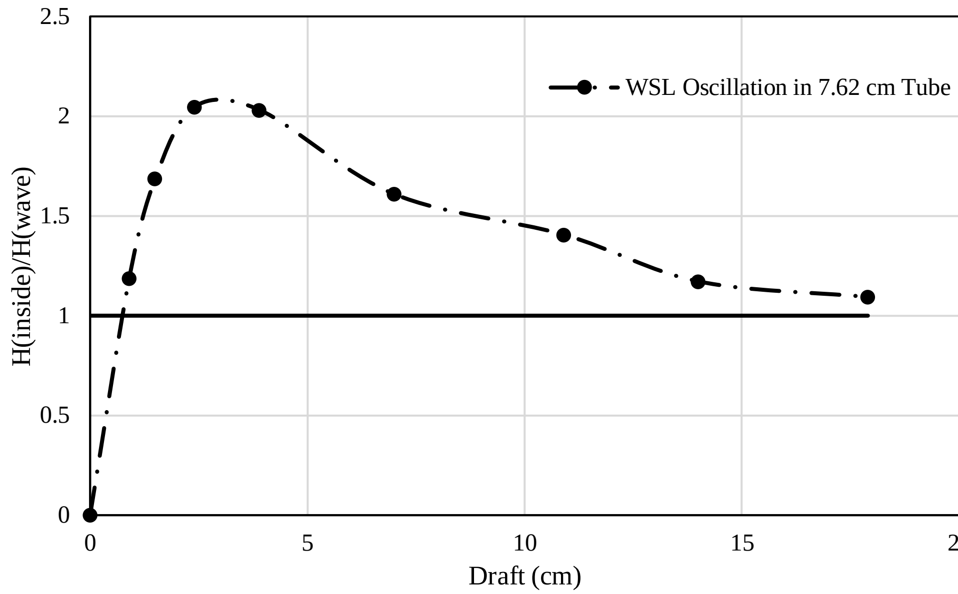

Figure 69: Wave height versus oscillation in the tube

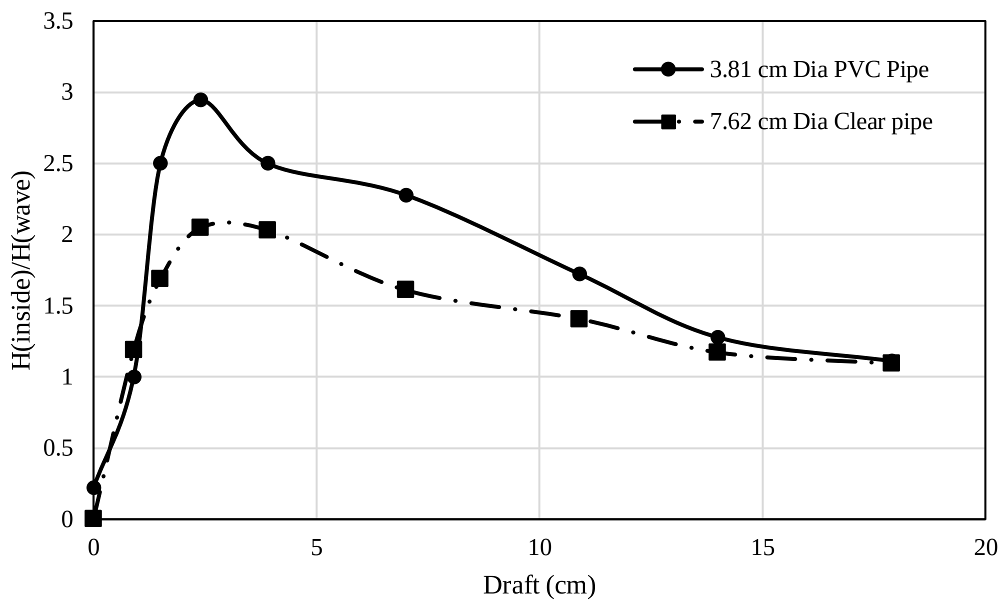

Figure 70: Comparing two different pipes

Figure 70 compares the results of 3.81 cm (1.5 inch) and 7.62 cm (3-inch) pipes. The Y-axis is dimensionless and shows the ratio of water surface oscillation in the pipe over the wave height. The ratio of one, indicates the oscillation inside the pipe is the same as wave height. As it is observable, the ratio starts from zero, and by increasing the draft it significantly goes up. After the peak, it descends and gets closer to one. For a smaller diameter, the peak is higher.

The motion inside the tube can be simulated with a rigid piston model equation (34), which is the application of Newton's second law in the vertical direction (Clappi et al, 2020).

$$m_w \ddot{z} + B\dot{z} + Cz = f_{exc} + f_{add} \tag{34}$$

Where m_w is the mass of the water column inside the tube, z is the free surface level inside the tube relative to the still water. C is the hydrostatic restoring coefficient, B is the damping coefficient. Two external forces are added mass force (f_{add}) and excitation force due to hydrodynamic pressure (f_{exc}) exerted by waves hitting the bottom of the water column (Clappi et al, 2020).

This experiment showed that different elevations can change the amplitude inside the tube. And the reason is not only the dynamic pressure but also added mass and excitation forces from harmonic effects.

The other parameter that affects the conversion rate are the losses, including headloss and entrance loss. The headloss can be calculated using the Darcy-Weisbach equation for the connecting hose and the cylinders. Equation (35) and (36) shows the Darcy-Weisbach headloss and the minor loss (entrance loss) equations that are used for entrance loss formula respectively.

$$f * L/D * V^2/2g \tag{35}$$

$$K * V^2/2g \tag{36}$$

Where f is the friction factor and can be obtained from the Moody diagram, L is the length of the pipe that the fluid moves through. V is the velocity of the fluid and g is the gravity. K is the entrance coefficient and is considered 0.5. The power in an ideal system can be found with equation (37). Where P is the power, γ is the specific weight of water, Q is the flow rate and h is driving head.

$$P = \gamma Q h \tag{37}$$

Considering all the losses for the experimental tests using the equation (35) and (36), dividing over ideal power (P) shows the losses are between 0.71% to 2.92%, which is insignificant in this system.

6.1 Comparing Numerical and Experimental

In order to compare numerical and experimental data, cylinders were drawn in AutoCAD as the same as the prototype. Cylinders were imported as STL files in Flow-3D and modeled numerically. Figure 71 to Figure 73 show how 5.08, 7.62 and 10.16 cm (2, 3- and 4-inch) cylinder drawings exactly match the prototype. After simulations, the graphs comparing numerical and experimental data were drawn. Figure 74 to Figure 76 compare numerical and experimental data for each cylinder.

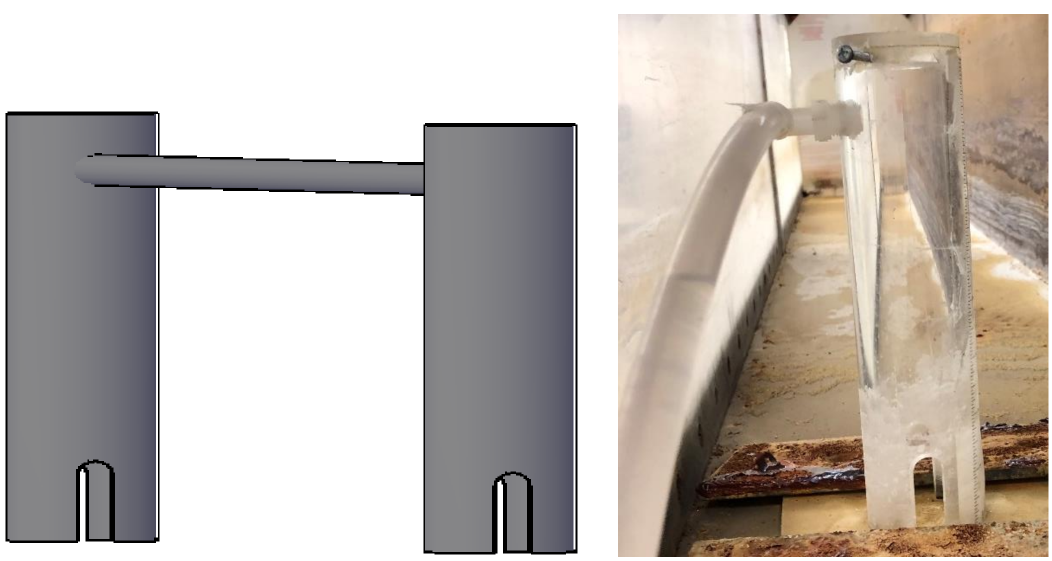

Figure 71: 5.08 cm (2-inch) numerical and physical model cylinders

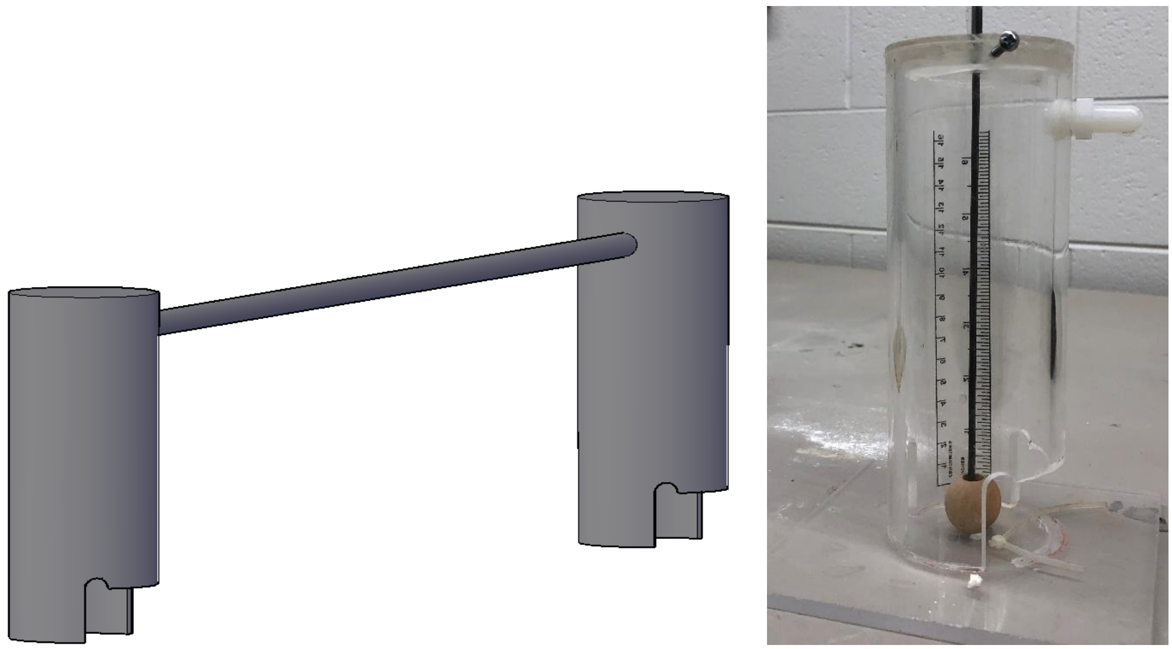

Figure 72: 7.62 cm (3-inch) numerical and physical model cylinders

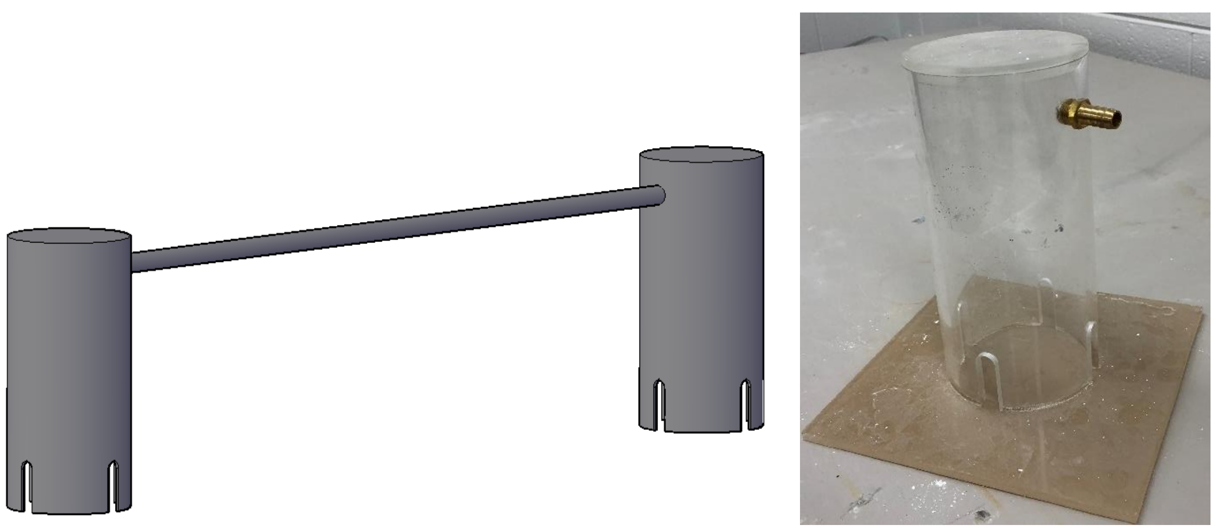

Figure 73: 10.16 cm (4-inch) numerical and physical model cylinders

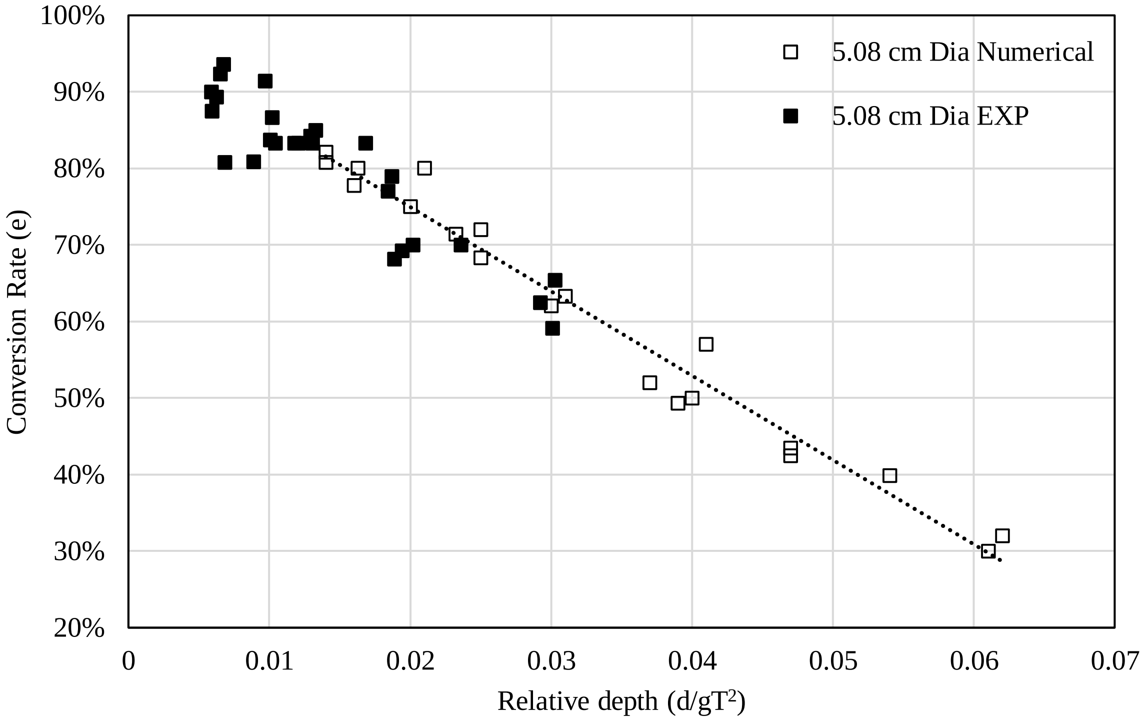

Figure 74: Comparison of numerical and physical model results for 5.08 cm (2-inch) diameter SOWC

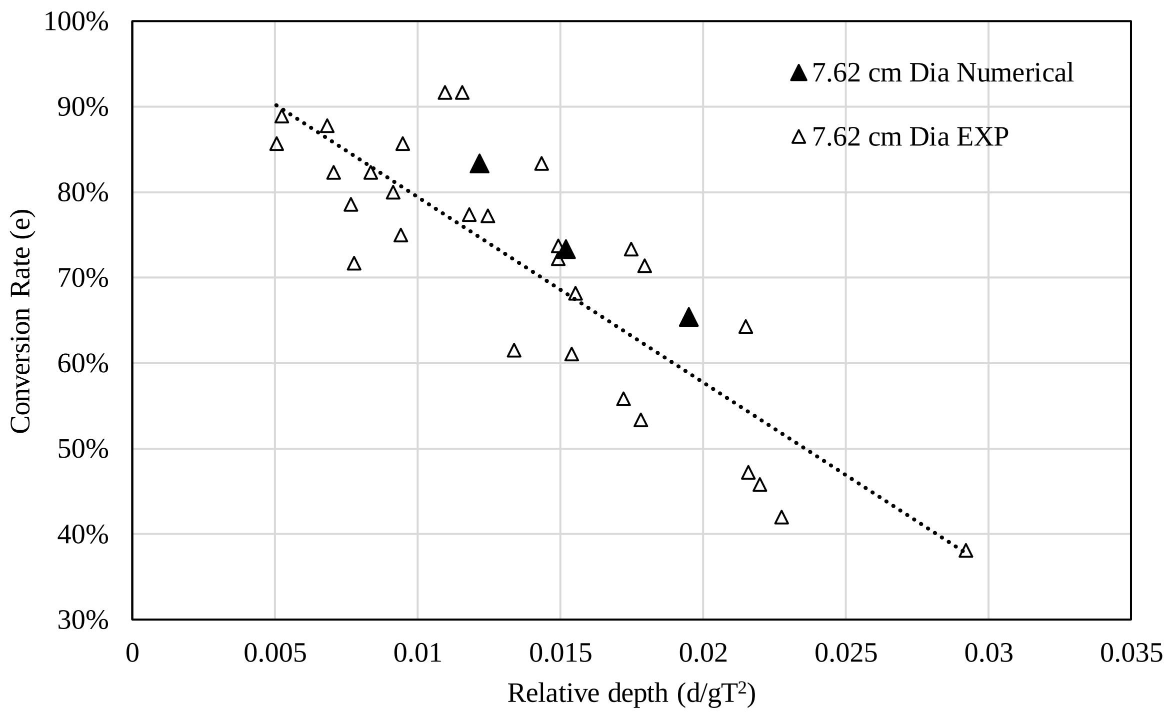

Figure 75: Comparison of numerical and physical model results for 7.62 cm (3-inch) diameter SOWC

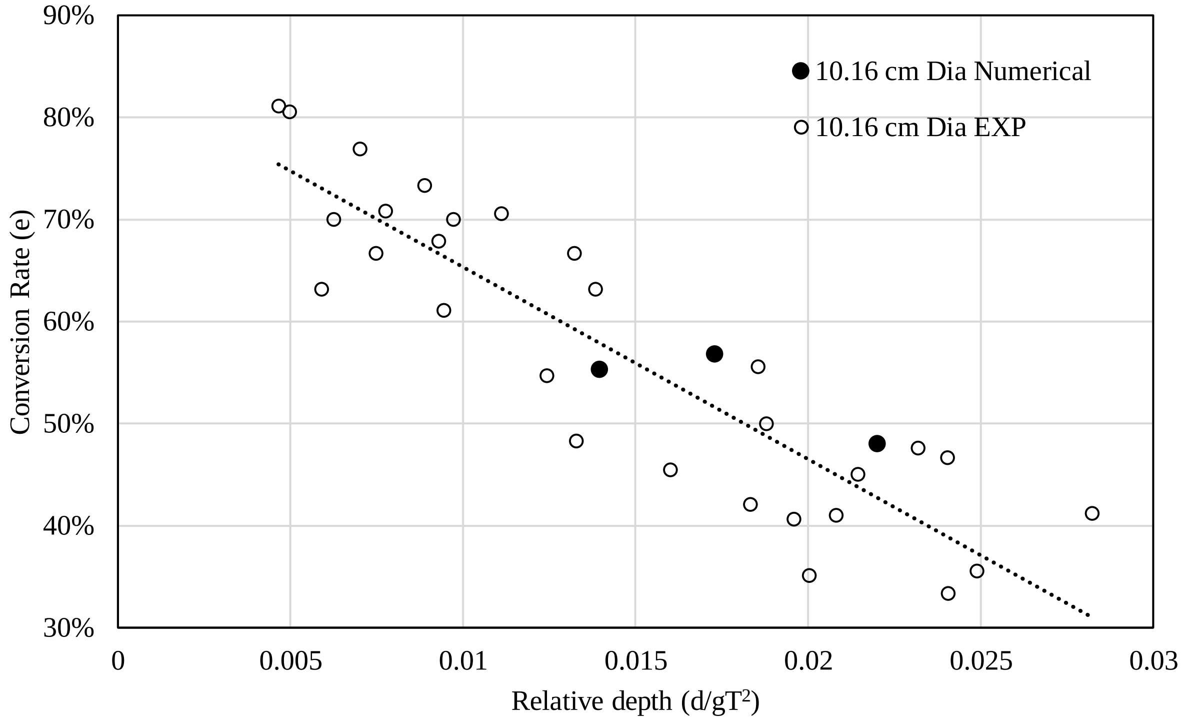

Figure 76: Comparison of numerical and physical model results for 10.16 cm (4-inch) diameter SOWC

Figure 74 shows that the trend of the numerical data for 5.08 cm (2-inch) diameter SOWCs follows the experimental data trendline. Previous numerical simulations were also added and compared in this graph since the cylinder had the same geometry size ratio of 1:4. The diameter of the original numerical cylinder was 15.24 cm (0.5 ft) and the height of the cylinder was 60.96 cm (2 ft). Thus, the ratio of the diameter to height of the cylinder was 0.25; the same as the 5.08 cm (2-inch) cylinder in experimental tests. Physical model cylinders were 20.32 cm (8-inch) tall with a diameter of 5.08 cm, 7.62 cm, 10.16 cm (2, 3, 4-inch, respectively). Therefore, previous numerical data (Figure 41) can be compared with 5.08 cm (2-inch) diameter experimental cylinder data (Figure 74).

Figure 74 shows that numerical and experimental results track for the 5.08 cm (2-inch) diameter cylinder. For each of the 7.62 cm (3-inch) and 10.16 cm (4-inch) diameter cylinders, three numerical tests were simulated to verify that the results are within the same range as shown in Figure 75 and Figure 76. The opening for 7.62 cm cylinder was more widely open compare to other cylinders which the numerical model was the exact same for purpose of comparison (Figure 72).

A numerical comparison was also completed using the same setup for the single open tube experiment shown in as Figure 69. The numerical wave matched the wave used in the flume and the draft was modified similarly to the physical experiment. Figure 77 shows the numerical results plotted again the physical results from Figure 69. The results from the numerical model have reasonably good agreement with the physical results. This provides additional confidence in the numerical technique.

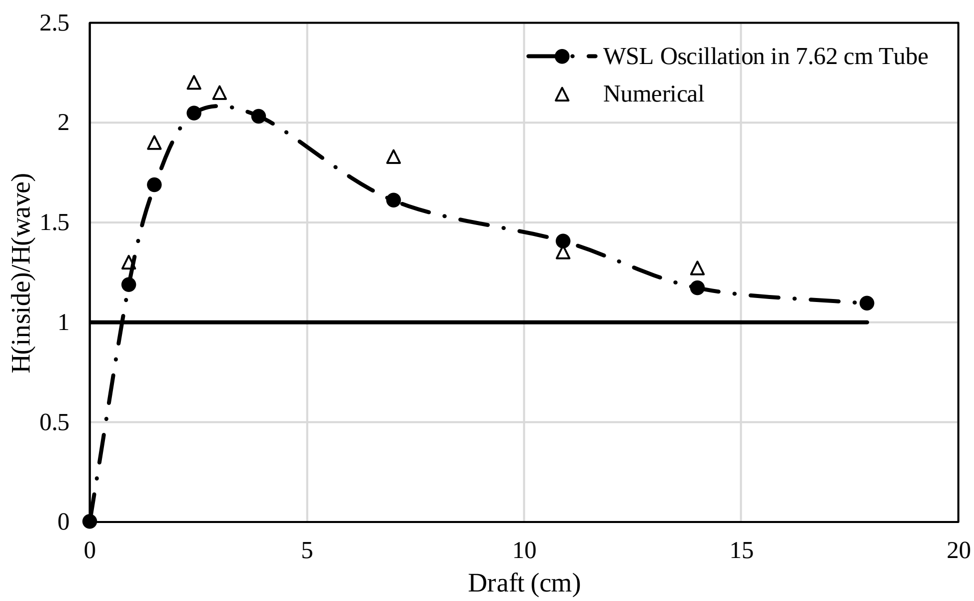

Figure 77: Numerical and experimental results for a single tube in different elevation

6.2 Accuracy of Measurements

Experimental data can contain error both due to instrumentation limitations and human error. Human error can occur when a value is read from the instrumentation and/or when it is recorded. While recording errors generally result in an outlier, slight variations in reading the instrumentation will also produce variations. The resulting analysis of errors is called "uncertainty analysis". This analysis provides upper and lower bounds for the estimation of the parameters. For instance, if the conversion rate (ε) is a measured value for efficiency, uncertainty analysis provides an estimated error U_ε of the efficiency. Then the efficiency would be reported az $\varepsilon \pm U_\varepsilon$

The estimated error is not directly measured, it calculated from other independent variables. For example, in this research, the efficiency is dependent on wave period (T), depth (d), wave height (H) and water oscillation inside (H_{inside}). Consider a general form as equation (38) (Elger et al., 2020).

$$X = f\,(y_1, y_2, \ldots, y_n) \tag{38}$$

Where x is the dependent parameter of interest and y_1 to y_n are the independent variables. Thus, the uncertainty (U_x) can be calculated as equation (39).

$$U_x = \left[\left(\frac{\partial x}{\partial y_1} U_{y_1} \right)^2 + \left(\frac{\partial x}{\partial y_2} U_{y_2} \right)^2 + \ldots + \left(\frac{\partial x}{\partial y_n} U_{y_n} \right)^2 \right]^{0.5} \tag{39}$$

Where U_{yi} is the uncertainty in the variable y_i

This research includes both human errors and device errors. The human error was for measuring water depth and the frequency of the paddle. A scale was used for measuring the depth which has an accuracy of 1 mm. However, since the scale was in the water and lights bends in the water, a safety factor is required for this error. So, the depth reading error is considered 3 mm. The other error was for measuring the frequency of the wave paddle motion. A timer was used to measure the period of the paddle. To increase the accuracy, the frequency was measured five times and averaged. The timer has an accuracy of a hundredth of a second but since human control and reads the timer, an error of 0.1 sec is considered.

Equation (39) is used to find the error for the relative depth ($d_r = d/gT^2$). Depth (d) and period (T) are the independent variables in the relative depth (d_r) formula. By plugging the relative depth into the Eqn (39) and simplifying it, the Eqn (40) can be achieved. Where U_{dr} is the error of relative depth, U_d is the error of depth and U_T is the error of period. As it is mentioned before U_d is 0.003 and U_T is 0.1 and by inserting these numbers Eqn (40) simplifies to Eqn (41).

$$\left(\frac{U_{d_r}}{d_r}\right)^2 = \left(\frac{U_d}{d}\right)^2 + \left(\frac{2U_T}{T}\right)^2 \tag{40}$$

$$U_{d_r} = \left(\frac{1}{gT^2}\right)\sqrt{0.003^2 + \left(\frac{0.2d}{T}\right)^2} \tag{41}$$

The same process is done to find the error of conversion rate ε (H_{inside}/H_{wave}), where H_{inside} is the water oscillation inside the cylinders measured with the sensors and H_{wave} is the wave height. Equation (42) shows the error of conversion rate (Cr). Where U_c shows the total error, for example, U_{cr} shows the error of relative depth. Since the accuracy of the sensors are 0.01 cm, that is the value for $U_{H(inside)}$ and $U_{H(wave)}$. Eqn (42) simplifies to Eqn (43).

$$\left(\frac{U_{C_r}}{C_r}\right)^2 = \left(\frac{U_{H_{inside}}}{H_{inside}}\right)^2 + \left(\frac{U_{H_{wave}}}{H_{wave}}\right)^2 \tag{42}$$

$$U_{C_r} = 0.01\sqrt{\frac{\left[1+{C_r}^2\right]}{H_{inside} * H_{wave}}} \tag{43}$$

Figure 78 to Figure 80 shows the error analysis for the 5.08, 7.62 and 10.16 cm (2, 3 and 4-inch) cylinders, respectively. Equation (41) is used to show the error in the x-direction and equation (43) is used for the error in the y-direction. As the graphs show, the error in the x-direction is relatively higher than the y-direction. The reason is that the amount of human error is higher compared to the device errors.

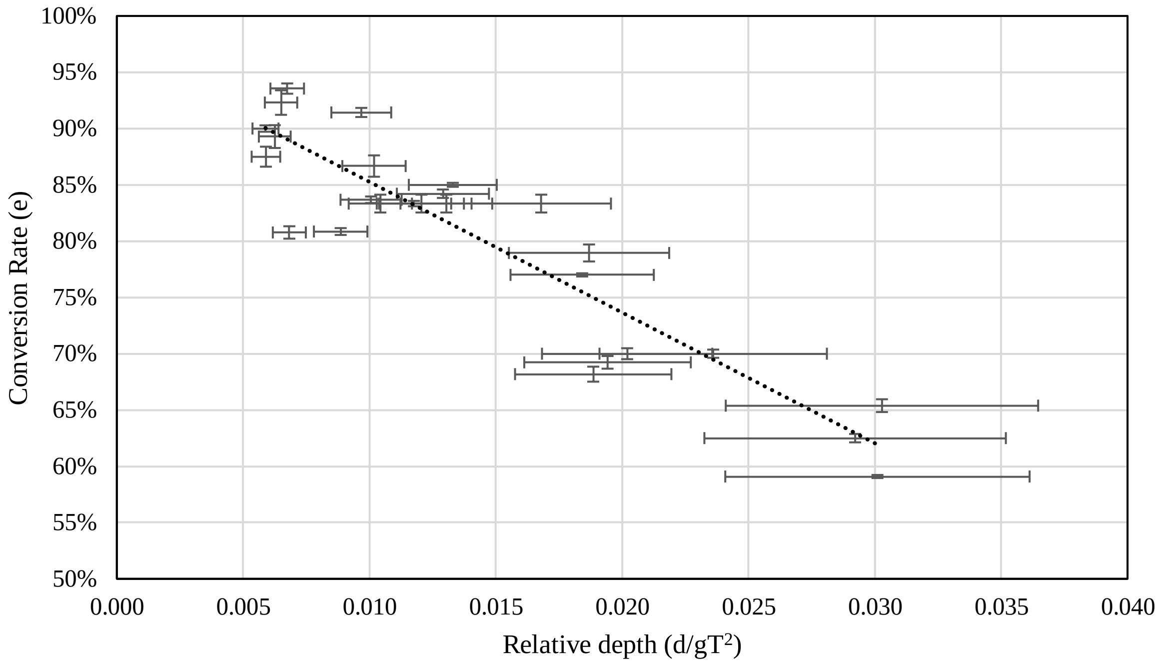

Figure 78: Error analysis for 5.08 cm (2-inch) cylinder

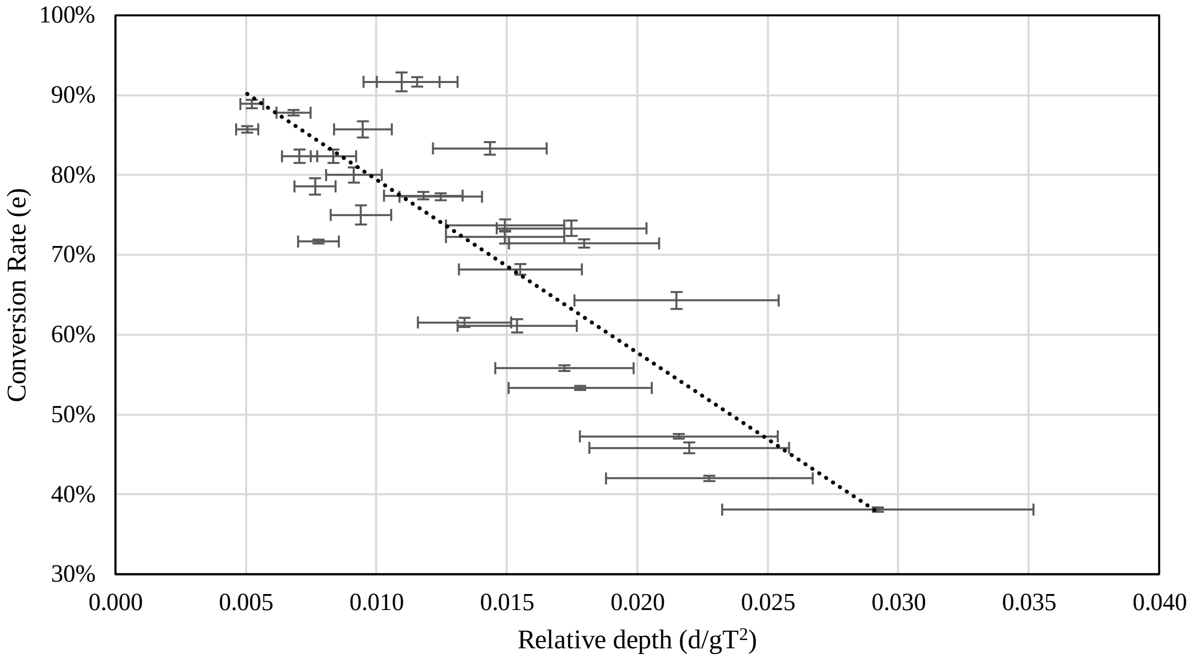

Figure 79: Error analysis for 7.62 cm (3-inch) diameter cylinder

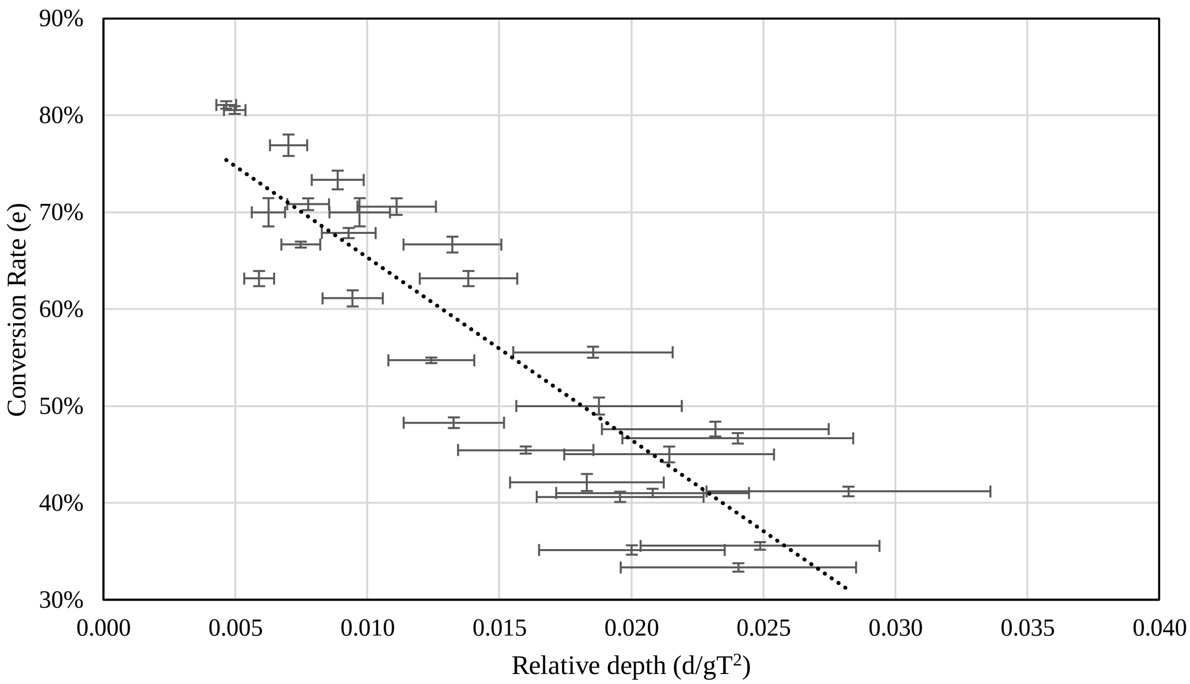

Figure 80: Error analysis for 10.16 cm (4-inch) diameter cylinder

CHAPTER 7. SUMMARY

This dissertation introduced a new conceptual submerged oscillating wave energy converter device. The proposed device is a combination of a pressure differential device and an oscillating water column device. The SOWC device includes two hollow one-end capped cylinders connected via a hose at the top of each cylinder. The cylinders are attached to the bottom and have openings to let the flow in and out. An air pocket is maintained and entrapped at the top part of the cylinders. As waves move over the SOWCs, the pressure fluctuates causing the air to travel back and forth between cylinders. From the movement of the air and the oscillation of water inside the cylinders, the energy can be obtained by using a hydraulic PTO. A Power Take-Off (PTO) system is defined as the mechanism which transforms the absorbed energy by the converter into useable electricity. One advantage of this system is by being placed on the ocean floor; it is relatively protected from the destructive storm forces. The protection can be improved if the device can be hinged to lay on the seabed floor during a storm. Additionally, by placing the device under the water surface, no visual obstructions are created, maintaining the shoreline view that is valued.

In this research, different variations of the SOWC device were numerically and physically tested and compared. The primary variable of interest is the conversion ratio; the efficiency of the device to convert the wave oscillations into oscillations inside of the SOWC. Also, five different openings on cylinders were tested numerically and discussed in Chapter 4, section 4.8.1 to see the effect of openings on efficiency. Results showed half bottom opened cylinder has higher conversion rate, if it is placed in the direction of waves. Experimental test results showed a good agreement between the conversion rate and relative depth. Numerical tests for 5.08, 7.62

and 10.16 cm (2, 3 and 4-inch) cylinders have been done and compared with experimental results. The number of tests and the range of conversion rate for all the compared experimental and numerical tests are shown in Table 9.

Table 9: Summary of compared numerical and experimental tests

Dia (cm)	Numerical		Experimental	
	# of tests	Conversion Rate (e) Range	# of tests	Conversion Rate (e) Range
5.08	20	30% – 81%	26	59% – 93%
7.62	3	65% – 83%	29	38% – 89%
10.16	3	48% – 57%	29	33% –93%

The R^2 of the experimental for correlation between conversion rate and relative depth was 0.72 to 0.84, and the R^2 for numerical tests for 5.08 cm (2-inch) cylinder were 0.94. Both results of experimental and numerical showed the following results:

- With the same wave period, an increasing depth decreases the conversion rate.
- Longer wave periods increase the conversion rate.
- An increasing relative depth decreases the conversion rate.
- Longer wavelengths increase the conversion rate.
- Smaller SOWC diameters increase the conversion rate.

Another observation was the different amplitude inside the cylinder with different amount of entrapped air. Experiments showed when the water surface level is in higher elevation the amplitude is greater. Different experiments were designed to understand this behavior. First, the amount of entrapped air changed to see if the air is the reason for this issue or not. Since putting a solid object inside the cylinder interpret as less amount of entrapped air, it was a suitable test. In this regard, a Styrofoam is cut and placed inside the cylinder to see if it can affect the amplitude of water oscillation inside the cylinder. 28 tests without Styrofoam and 37 with Styrofoam was tested and compared. Results showed that the amount of entrapped air cannot affect the amplitude.

The second assumption was the hydrodynamic pressure. Two tests were designed to prove the validity of the assumption. The first designed test was elevating one cylinder with the same amount of entrapped air to see if the amplitude of oscillation inside the cylinder can change. The result showed that elevating one SOWC can improve the conversion rate because by getting closer to the surface, dynamic velocity increases. The results are shown in Table 8. The second test was using an open-end pipe to see how elevating the pipe and increasing the draft can change the oscillation inside the tube.

In this regard, when a solitary open pipe was placed in the flume, the draft (distance between the bottom and bed) was changed and the conversion rate was measured. It showed the oscillation inside the tube does not follow wave heights. Results showed the conversion rate can be even more than two. The conversion rate of unity indicates the oscillation inside the tube is the same as the wave height. By increasing the draft, oscillation increases two times more than wave height and then decreases and leaned toward the wave height. The reason for this behavior is hydrodynamic pressure and excitation forces from harmonic effects. This behavior numerically and experimentally tested and the results were in good agreement (Figure 77). These two experiments proved that the assumption was correct and the tendency to oscillate more is because of the hydrodynamic pressure and harmonic effect.

While the implementation of a PTO is not part of this study, a suggested PTO system is hydraulic PTO which consists of a dual pump that can transmit high-pressure water to a shoreline turbine. The implementation of a PTO system is recommended for future studies. Other suggestions for future research can be the change in the location of the openings, it can be at the top (Figure 81-a) or bottom (Figure 81-b) similar to. The advantage of these devices can be the ability to capture more dynamic pressure.

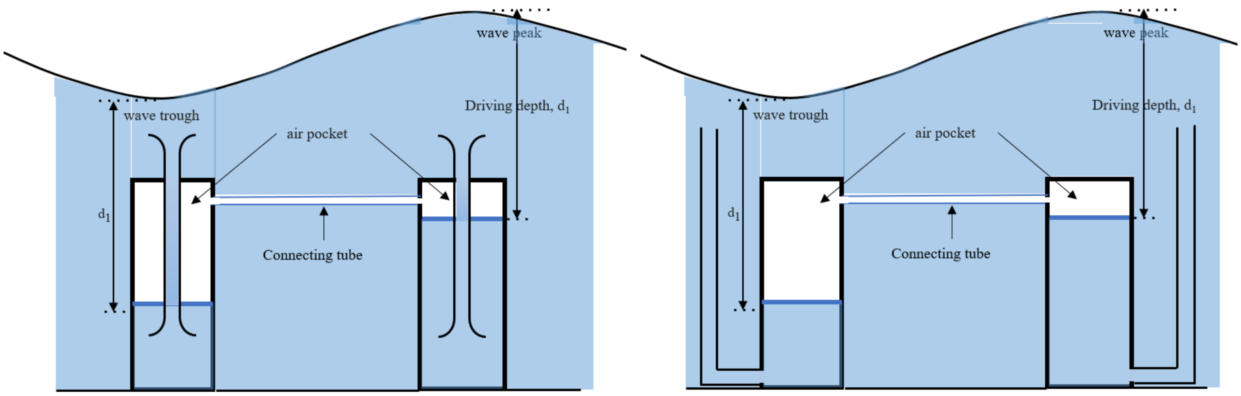

(a) (b)

Figure 81: Suggested device with different openings

The other future work can be analyzing a farm of the SOWCs to see the efficiency and probably the harmonic effect of them on each other that improve the efficiency. Figure 82 shows the proposed SOWC farm. The distance between SOWC cylinders need to be determined based on the wavelength. By getting closer to shore line the wavelength decreases so the cylinders distance needs to be shortened. All of the cylinders can be connected to a main hub and transmit the high pressure to the shoreline.

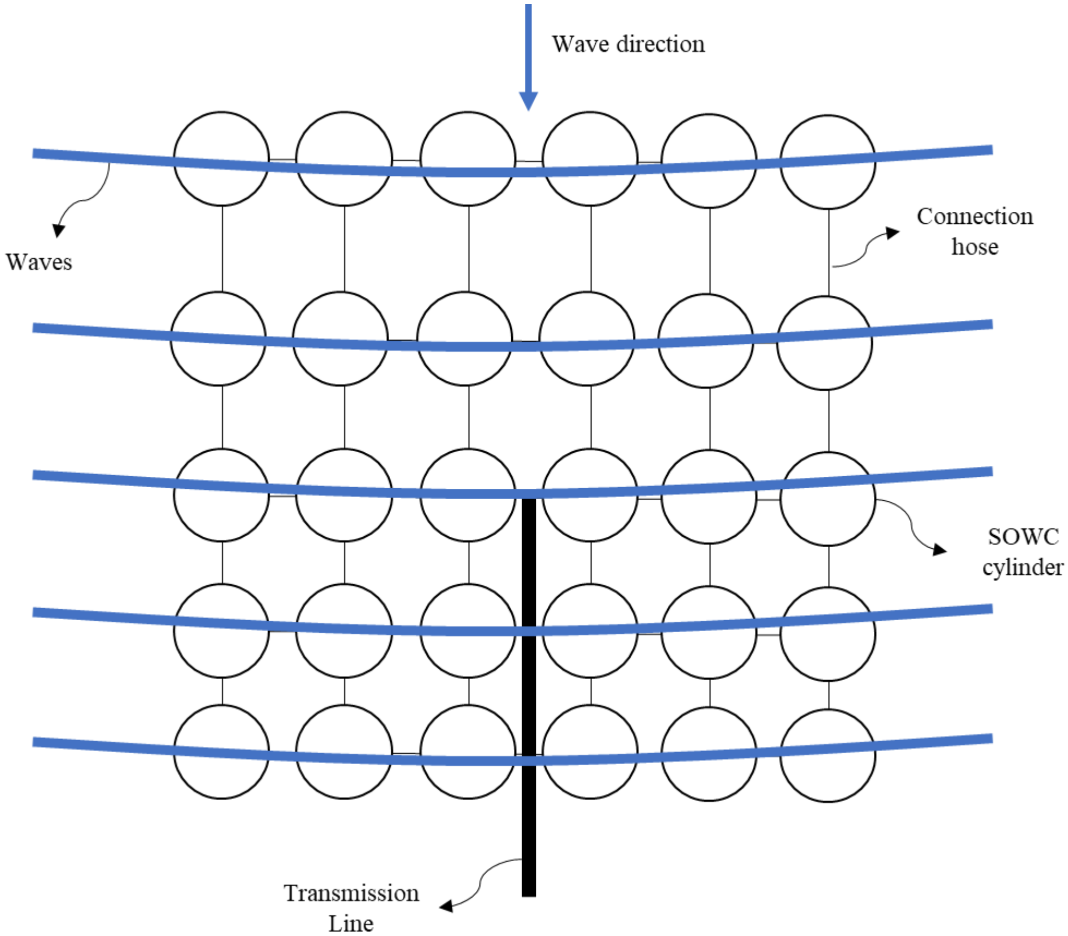

Figure 82: Proposed SOWCs farm

REFERENCES

Antonio, F. D. O. (2010). Wave energy utilization: A review of the technologies. Renewable and sustainable energy reviews, 14(3), 899-918.

Awang, N. A., Anuar, N. M., & Sidek, F. J. (2018). Potential Multi-Function Cylinder as Wave Attenuator. J Coast Zone Manag, 21(460), 2.

Babarit, A., Wendt, F., Yu, Y. H., & Weber, J. (2017). Investigation on the energy absorption performance of a fixed-bottom pressure-differential wave energy converter. *Applied Ocean Research*, *65*, 90-101.

Barbosa, D. V. E., Santos, A. L. G., dos Santos, E. D., & Souza, J. A. (2019). Overtopping device numerical study: Openfoam solution verification and evaluation of curved ramps performances. International Journal of Heat and Mass Transfer, 131, 411-423.

Beatty, S. J., Bocking, B., Bubbar, K., Buckham, B. J., & Wild, P. (2019). Experimental and numerical comparisons of self-reacting point absorber wave energy converters in irregular waves. Ocean Engineering, 173, 716-731.

Bevilacqua, Giovanna, and Barbara Zanuttigh. "Overtopping Wave Energy Converters: General Aspects and Stage of Development." (2011): n. pag. University of Bologna, 2011. Web. 24 July 2012.

Brekken, T. Fundamentals of ocean wave energy conversion, modeling, and control. in Industrial Electronics (ISIE), 2010 IEEE International Symposium on. 2010. IEEE.

Brekken, T. K. (2011, June). On model predictive control for a point absorber wave energy converter. In 2011 IEEE Trondheim PowerTech (pp. 1-8). IEEE.

Burman, K., Walker, A. (2009) “Ocean Energy Technology Overview," US National Renewable Energy Laboratory, DOE/GO-102009-2823.

Cappietti, L., Simonetti, I., Penchev, V., & Penchev, P. (2019). Laboratory tests on an original wave energy converter combining oscillating water column and overtopping devices.

Cebeci, T., & Cousteix, J. (2005). Conservation Equations for Mass and Momentum for Incompressible Flows. Modeling and Computation of Boundary-Layer Flows: Laminar, Turbulent and Transitional Boundary Layers in Incompressible and Compressible Flows, 17-25.

Cerveira, F., Fonseca, N., & Pascoal, R. (2013). Mooring system influence on the efficiency of wave energy converters. International Journal of Marine Energy, 3, 65-81.

Chatzigiannakou, M.A., Ulvgård, L., Temiz, I. et al. Offshore deployments of wave energy converters by Uppsala University, Sweden. Mar Syst Ocean Technol 14, 67–74 (2019). https://doi.org/10.1007/s40868-019-00055-2

Chen, F., Duan, D., Han, Q., Yang, X., & Zhao, F. (2019). Study on force and wave energy conversion efficiency of buoys in low wave energy density seas. Energy conversion and management, 182, 191-200.

Ciappi, L., Cheli, L., Simonetti, I., Bianchini, A., Manfrida, G., & Cappietti, L. (2020). Wave-to-Wire Model of an Oscillating-Water-Column Wave Energy Converter and Its Application to Mediterranean Energy Hot-Spots. Energies, 13(21), 5582.

Clément, A., McCullen, P., Falcão, A., Fiorentino, A., Gardner, F., Hammarlund, K., ... & Pontes, M. T. (2002). Wave energy in Europe: current status and perspectives. Renewable and sustainable energy reviews, 6(5), 405-431.

Cordonnier, J., et al., *SEAREV: Case study of the development of a wave energy converter*. Renewable Energy, 2015. **80**: p. 40-52.

Connell, K. O., Thiebaut, F., Kelly, G., & Cashman, A. (2018). Development of a free heaving OWC model with non-linear PTO interaction. Renewable energy, 117, 108-115.

Devolder, B., Stratigaki, V., Troch, P., & Rauwoens, P. (2018). CFD simulations of floating point absorber wave energy converter arrays subjected to regular waves. *Energies*, *11*(3), 641.

Dufera, H., PB500, 500 KW UTILITY-SCALE POWERBUOY PROJECT. 2016, Ocean Power Technologies Inc.

Elger, D. F., LeBret, B. A., Crowe, C. T., & Roberson, J. A. (2020). Engineering fluid mechanics. John Wiley & Sons.

Finavera Point Absorber. Available from: http://nnmrec.oregonstate.edu/finavera-point-absorber.

FLOW-3D user manual; excellence in flow modeling software, v 12. (2021). FLOW-3D. Flow Science, Inc., Santa FE, NM.

FLOW-3D Cast FAQ, (2009). Available from: http://www.easysimulation.com/public/flow3dcast/documentation/FLOW3D-Cast_FAQ.pdf

Folley, M., Whittaker, T., & Osterried, M. (2004, January). The oscillating wave surge converter. In The Fourteenth International Offshore and Polar Engineering Conference. International Society of Offshore and Polar Engineers.

Gilbert, G., Thompson, D. M., & Brewer, A. J. (1971). Design curves for regular and random wave generators. Journal of Hydraulic Research, 9(2), 163-196.

Gunawardane, S. D. G. S. P., Folley, M., & Kankanamge, C. J. (2019). Analysis of the hydrodynamics of four different oscillating wave surge converter concepts. Renewable energy, 130, 843-852.

Heath, T. V. (2012). A review of oscillating water columns. Philosophical Transactions of the Royal Society A: Mathematical, Physical and Engineering Sciences, 370(1959), 235-245.

Henry, A., Folley, M., & Whittaker, T. (2018). A conceptual model of the hydrodynamics of an oscillating wave surge converter. Renewable Energy, 118, 965-972.

Holmberg, P., Andersson, M., Bolund, B., & Strandanger, K. (2011). Wave power-Surveillance study of the development. Elforsk Rapp, 11, 47.

Holmes, B. (2015). Best Practice Manual for Wave Simulation. Tech. rep.

Hübner, r. G., oleinik, p. H., marques, w. C., gomes, m. N., dos santos, e. D., machado, b. N., & isoldi, l. A. (2019). Numerical study comparing the incidence influence between realistic wave and regular wave over an overtopping device. Revista de engenharia térmica, 18(1), 46-49.

Jarocki, D., & Wilson, J. H. (2010, January). Wave energy converter performance modeling and cost of electricity assessment. In ASME International Mechanical Engineering Congress and Exposition (Vol. 44298, pp. 333-342).

Karadeniz, H., Saka, M. P., & Togan, V. (2013). Water Wave Theories and Wave Loads. In Stochastic Analysis of Offshore Steel Structures (pp. 177-252). Springer, London.

Kilcher, Levi, Michelle Fogarty, and Michael Lawson. (2021). Marine Energy in the United States: An Overview of Opportunities. Golden, CO: National Renewable Energy Laboratory. NREL/TP-5700-78773. https://www.nrel.gov/docs/fy21osti/78773.pdf.

Koca, K., Kortenhaus, A., Oumeraci, H., Zanuttigh, B., Angelelli, E., Cantu, M., ... & Franceschi, G. (2013, September). Recent advances in the development of wave energy converters. In 9th European Wave and Tidal Energy Conference (EWTEC) (pp. 2-5).

Lehmann, M., Elandt, R., Shakeri, M., & Alam, R. (2014). The wave carpet: development of a submerged pressure differential wave energy converter. In *30th Symposium on Naval Hydrodynamics* (pp. 2-7).

Lewis, M., Neill, S. P., Robins, P. E., & Hashemi, M. R. (2015). Resource assessment for future generations of tidal-stream energy arrays. Energy, 83, 403-415.

Loh, T., & Young, T. (2018). Assessments of Wave-Structure Interactions for an Oscillating Wave Surge Converter using CFD (Doctoral dissertation, University of Plymouth).

Lomonaco, p., bosma, b., delos-reyes, m. I. K. E., gillespie, a., maddux, t., morrow, m., & özkan-haller, t. U. B. A. Physical model testing of the scour induced by apex, a submerged pressure differential wave energy converter.

López, I., & Iglesias, G. (2014). Efficiency of OWC wave energy converters: A virtual laboratory. *Applied Ocean Research*, *44*, 63-70.

Maloney, P. (2019). Performance assessment of a 3-body self-reacting point absorber type wave energy converter (Doctoral dissertation).

"Marine and Hydrokinetic Resource Assessment and Characterization", (2021), Energy.gov, www.energy.gov/eere/water/marine-and-hydrokinetic-resource-assessment-and-characterization

Wikipedia contributors. (2019, December 12).

Moreno, E. C., & Stansby, P. K. (2018, October). Experimental assessment of a 6-float M4 wave energy converter. In Advances in Renewable Energies Offshore: Proceedings of the 3rd International Conference on Renewable Energies Offshore (RENEW 2018), October 8-10, 2018, Lisbon, Portugal (p. 401). CRC Press.

NOAA, National Ocean Service, (2021); National Ocean and Atmospheric Administration, U.S. Department of Commerce. https://oceanservice.noaa.gov/facts/population.html

Ning, D., Wang, R., Teng, B., & Zou, Q. (2019, February). Experimental and numerical investigations on wave dynamics of a dual-chamber OWC wave energy device. In 38th International Conference on Ocean, Offshore and Arctic Engineering 2019 (pp. OMAE2019-95165). American Society of Mechanical Engineers.

Ocean sensor systems (2020). http://www.oceansensorsystems.com/PDF/WS-UserManual.pdf

Offshore technology research center, OTRC Wave Basin, https://otrc.tamu.edu/otrc-wave-basin/

Orer, G., & Ozdamar, A. (2007). An experimental study on the efficiency of the submerged plate wave energy converter. *Renewable Energy*, *32*(8), 1317-1327.

Prado, M., & Polinder, H. (2013). Case study of the Archimedes Wave Swing (AWS) direct drive wave energy pilot plant. In Electrical Drives for Direct Drive Renewable Energy Systems (pp. 195-218). Woodhead Publishing.

Rhinefrank, K., et al. Numerical and experimental analysis of a novel wave energy converter. in ASME 2010 29th International Conference on Ocean, Offshore and Arctic Engineering. 2010. American Society of Mechanical Engineers.

Roberts, G. D. (2017). Research and development of a wave impact simulation device for the Idaho State University Component Flooding Evaluation Laboratory.

Rusu, E., & Onea, F. (2018). A review of the technologies for wave energy extraction. Clean Energy, 2(1), 10-19.

Rusu, E. (2014). Evaluation of the wave energy conversion efficiency in various coastal environments. *Energies*, *7*(6), 4002-4018.

Salter's duck. In Wikipedia, The Free Encyclopedia. Retrieved 16:05, January 22, 2020, from https://en.wikipedia.org/w/index.php?title=Salter%27s_duck&oldid=930379883

Shadman, M., Estefen, S. F., Rodriguez, C. A., & Nogueira, I. C. (2018). A geometrical optimization method applied to a heaving point absorber wave energy converter. *Renewable energy*, *115*, 533-546.

So, R., Bosma, B., Ruehl, K., & Brekken, T. (2019). Modeling of a Wave Energy Oscillating Water Column as a Point Absorber Using WEC-Sim. *IEEE Transactions on Sustainable Energy*.

Mcwilliams, B. (2000). The Bassist Haggis and the Salter's Duck. The Irish Times, The Irish Times, www.irishtimes.com/news/the-bassist-haggis-and-the-salter-s-duck-1.297902.

Sorensen, R. M. (2005). Basic coastal engineering (Vol. 10). Springer Science & Business Media.

Taniguchi, T., Matsui, R., Shimozato, K., Fujiwara, T., & Inoue, S. (2018). Motions and Load Characteristics of an Attenuator Type Wave Energy Converter in Longitudinal Waves. Journal of the Japan Society of Naval Architects and Ocean Engineers, 27.

Titah-Benbouzid, H. and M. Benbouzid. *Ocean wave energy extraction: Up-to-date technologies review and evaluation*. in *Power Electronics and Application Conference and Exposition (PEAC), 2014 International*. 2014. IEEE.

Torabi, M., & Savage, B. (2019). Modeling of a Novel Submerged Oscillating Water Column (SOWC) Energy Harvester. In 7th IAHR International Junior Researcher and Engineer Workshop on Hydraulic Structures.

Torabi, M., & Savage, B. (2020, May). Efficiency Improvement of a Novel Submerged Oscillating Water Column (SOWC) Energy Harvester. In World Environmental and Water Resources Congress 2020: Emerging and Innovative Technologies and International Perspectives (pp. 23-30). Reston, VA: American Society of Civil Engineers.

Thorpe, T. W. (1999). A brief review of wave energy. London: Harwell Laboratory, Energy Technology Support Unit.

Ulvgård, L. (2017). Wave Energy Converters: An experimental approach to onshore testing, deployments and offshore monitoring (Doctoral dissertation, Acta Universitatis Upsaliensis).

Valério, D., Beirao, P., & Da Costa, J. S. (2007, January). Reactive control and phase and amplitude control applied to the Archimedes Wave Swing. In The Seventeenth International Offshore and Polar Engineering Conference. International Society of Offshore and Polar Engineers.

Vertechy, R., Fontana, M., Papini, G. R., & Bergamasco, M. (2013, April). Oscillating-water-column wave-energy-converter based on dielectric elastomer generator. In Electroactive Polymer Actuators and Devices (EAPAD) 2013 (Vol. 8687, p. 86870I). International Society for Optics and Photonics.

Wave devices, 2019: EMEC: European Marine Energy Centre. Available from: http://www.emec.org.uk/marine-energy/wave-devices/.

Weber, J., et al. *Wavebob—research & development network and tools in the context of systems engineering*. in *Proc. Eighth European Wave and Tidal Energy Conference, Uppsala, Sweden*. 2009.

Wei, Y., Rafiee, A., Henry, A., & Dias, F. (2015). Wave interaction with an oscillating wave surge converter, part I: Viscous effects. Ocean Engineering, 104, 185-203.

Whittaker, T., & Folley, M. (2012). Nearshore oscillating wave surge converters and the development of Oyster. Philosophical Transactions of the Royal Society A: Mathematical, Physical and Engineering Sciences, 370(1959), 345-364.

Yakhot, V. and Orszag, S.A., 1986, Renormalization group analysis of turbulence I. Basic theory, Journal of Scientific Computing (1), 3-51.

Yakhot, V. and Smith, L.M., 1992, The renormalization group, the e-expansion and derivation of turbulence models, Journal of Scientific Computing (7), 35-61.

Yang, L., Lyu, Z., Yang, P., Pavlidis, D., Fang, F., Xiang, J., ... & Pain, C. (2018, July). Numerical Simulation of Attenuator Wave Energy Converter Using one-fluid formulation. In The 28th International Ocean and Polar Engineering Conference. International Society of Offshore and Polar Engineers.

Zhang, D. H., Shi, Y. X., Huang, C., Si, Y. L., Huang, B., & Li, W. (2018). SPH method with applications of oscillating wave surge converter. Ocean Engineering, 152, 273-285.

Zuo, W. (2005). Introduction of computational fluid dynamics. Joint Advanced Student School (JASS).

Appendix A

Calculating Pressure on Piston Paddle

Piston Motion:

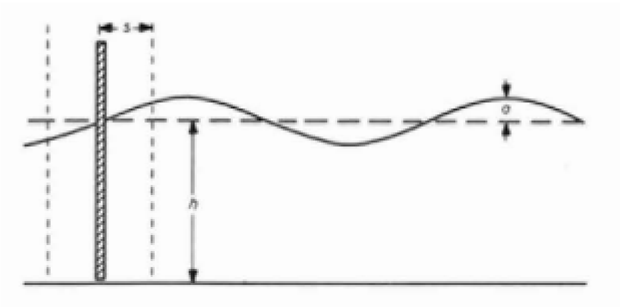

1b.

Depth of water (h): 3' = 0.914 m

Wave period (T): 1.5 sec

Wave length (λ): 10.8 ft= 3.3 m

Amplitude of wave (a=H/2):0.5 ft

Amplitude of paddle(S): 0.328 ft= 0.1 m

$$S = H * \frac{\left(sinh\left(2kd\right) + 2kd\right)}{2\left(cosh\left(2kd\right) - 1\right)}$$

$a/s = G_2(\eta)$

By assuming $M = 100kg$

$$E = \rho g h s = 897 N/m$$

$$\eta = \frac{h}{gT^2} = \frac{3}{32.2*9} = 0.041$$

$$G_2(\eta) = 1$$

$$F_R / E = G_3(\eta) = 0.85$$

$$F_I / E = G_4(\eta) = 0.06$$

$$F_{RR} = 2EG_3 = 1525 \quad N/m$$

$$F_{II} = 2EG_4 + \frac{4\pi^2 sM}{T^2} = 283 \quad N/m$$

$$F = \sqrt{F_{RR}^2 + F_{II}^2} = 1551 \quad N/m$$

$$\boxed{F_{paddle(4')} = 6.2\ kN}$$

Flap Motion

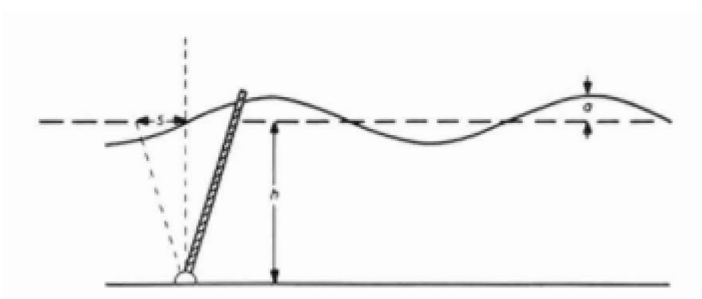

Depth of water (h): 3’ = 0.914 m

Wave period (T): 1.5 sec

Wave length (λ): 10.8 ft= 3.3 m

Amplitude of wave (a=H/2):0.5 ft

Amplitude of paddle(S): 0.53 ft= 0.162 m

$$S = H * \frac{kd\left(sinh(2kd) + 2kd\right)}{4\sinh(kd)\left(kd*\sinh(kd) - \cosh(kd) + 1\right)}$$

By assuming $M = 100kg$

$$E = \rho ghs = 1453 N/m$$

$$\eta = \frac{h}{gT^2} = \frac{3}{32.2*1.5^2} = 0.04$$

$$G_2(\eta) = 1$$

$$F_R / E = G_3(\eta) = 0.3$$

$$F_I / E = G_4(\eta) = 0.009$$

$$F_{RR} = 2EG_3 = 872 \quad N/m$$

$$F_{II} = 2EG_4 + \frac{4\pi^2 sM}{T^2} = 310.4 \quad N/m$$

$$F = \sqrt{F_{RR}{}^2 + F_{II}{}^2} = 926 \quad N/m$$

$$\boxed{F_{paddle(4')} = 3.7\ kN}$$

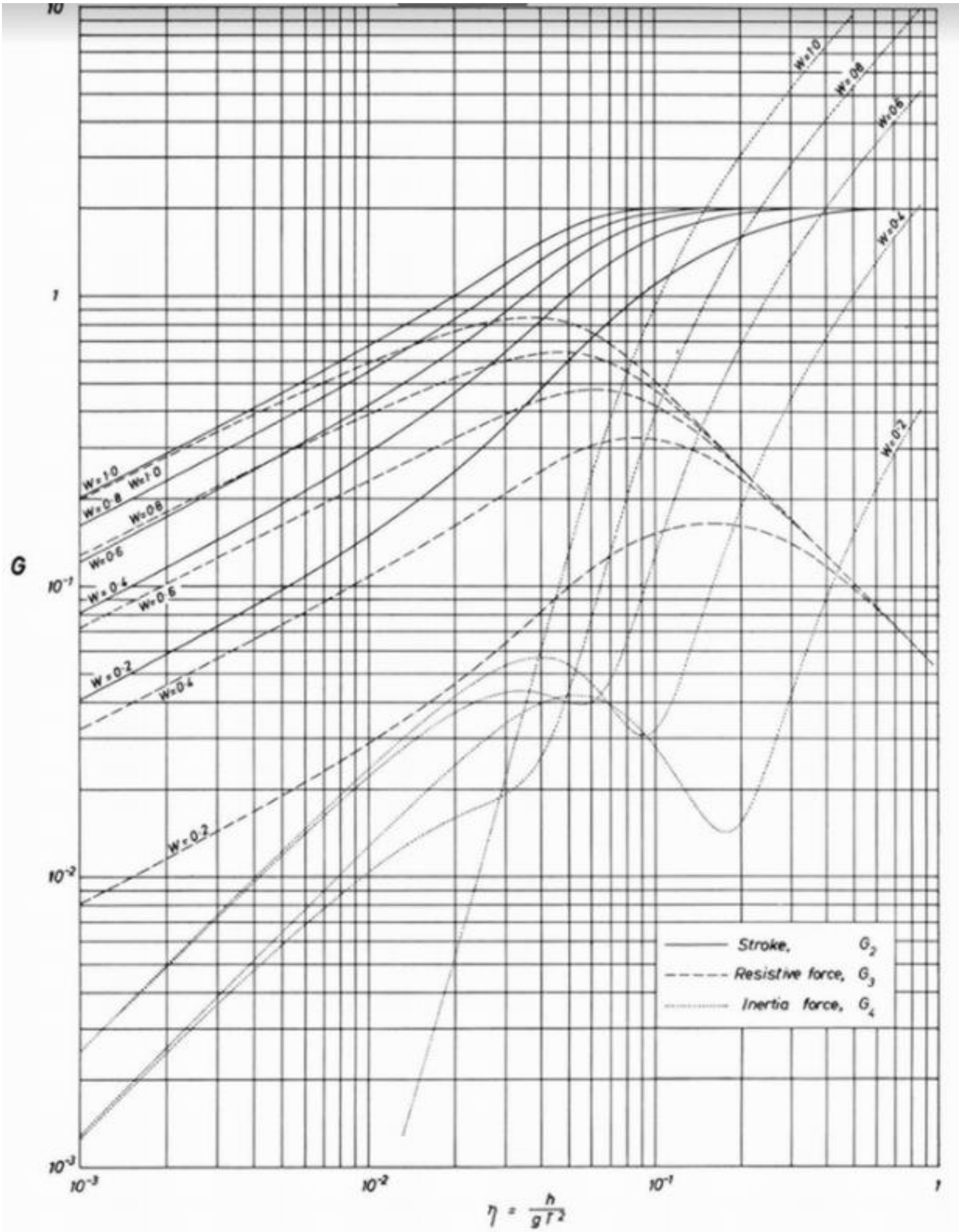

Figure 83: Piston motion (Gilbert et al. 1971)

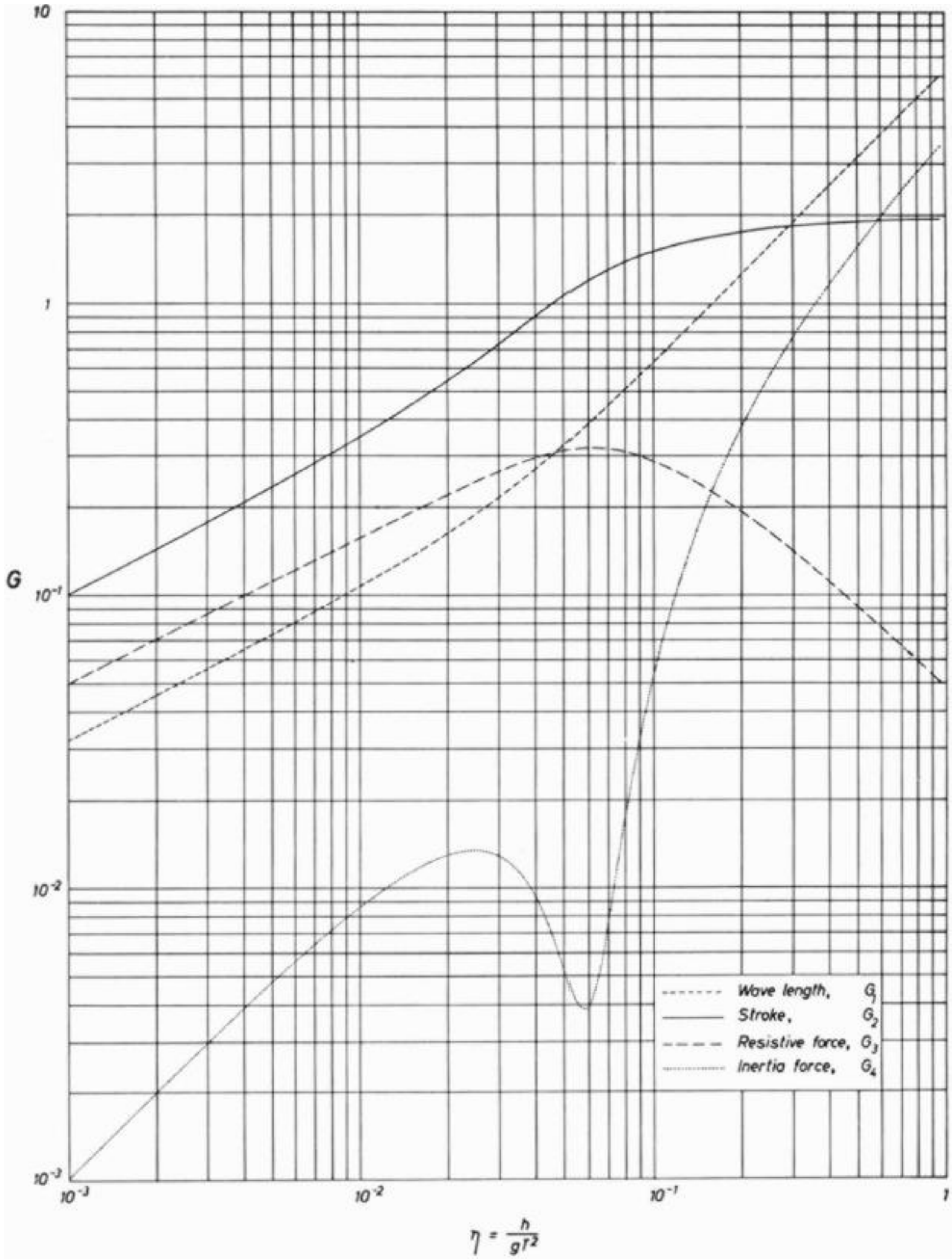

Figure 84: Flap motion (Gilbert et al. 1971)

Appendix B

Design Bracing for Flume

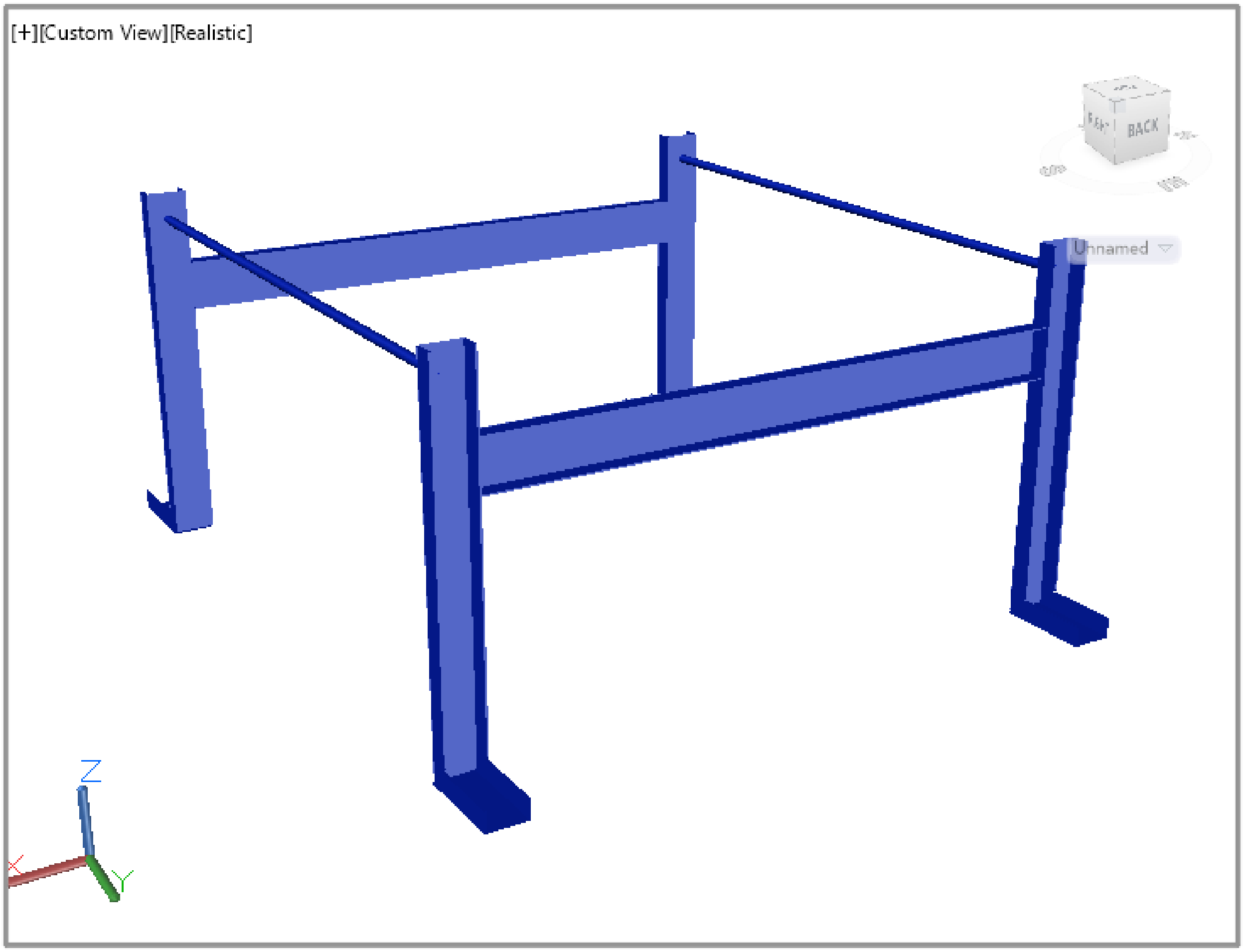

Rebar

$$\gamma = 62.4 \quad lbf\ /\ ft^3$$
$$h = 4 \quad ft$$
$$l = 8 \quad ft$$
$$w = \gamma h^2 \big/ 6 = 166.4 \quad lbf\ /\ ft$$
$$\sigma_{ys} = yield\ stress = 53700 \quad psi$$
$$F = w * l = 1331.2 \quad lbf$$
$$0.6\sigma_{ys} = \frac{F}{A} \rightarrow A = \frac{1331.2 \ \ lbf}{32220 \quad psi} = 0.04$$
$$d = 0.23\, in$$
$$smallest\ available\ rebar$$

Horizontal C-shape:

$$\gamma = 62.4 \quad lbf\ /\ ft^3$$
$$h = 4 \quad ft$$
$$l = 8 \quad ft$$
$$w = \gamma h^2 \big/ 6 = 166.4 \quad lbf\ /\ ft$$
$$\sigma_{ys} = yield\ stress = 53700 \quad psi$$
$$M_{\max} = \frac{wl^2}{8} = 1331.2 \quad lb.ft$$
$$\Delta_{\max} = \frac{5wl^4}{384EI}$$
$$M_R = 0.6\sigma_{ys} Z_x$$
$$required\ \ Z_x = \frac{M}{0.6\sigma_{ys}} = \frac{1.67M}{\sigma_{ys}} = \frac{2223.1\, lb.ft}{53700\ psi} * 12 \frac{in}{ft} = 0.497\ in^3$$

Vertical C-shape:

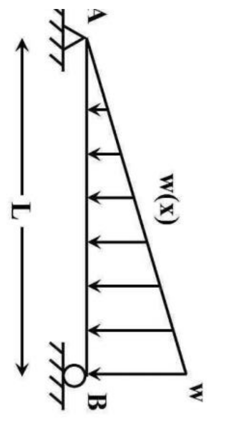

$$\gamma = 62.4 \quad lbf\ /\ ft^3$$
$$h = 35\, in = 2.9\ ft$$
$$w = \gamma h = 181 \quad psf$$
$$\sigma_{ys} = yield\ stress = 53700 \quad psi$$
$$M_{\max} = \frac{wh^2}{9\sqrt{3}} = 97.6 \quad lb.ft$$
$$M_R = 0.6\sigma_{ys} Z_x$$
$$required\ Z_x = \frac{M}{0.6\sigma_{ys}} = \frac{1.67M}{\sigma_{ys}} = \frac{2223.1\, lb.ft}{53700\ psi} * 12\frac{in}{ft} = 0.036\, in^3$$

Appendix C

Torque Calculations

	Torque calc		
torque	T	234.6243	lb-in
total force	FT	3370	lb
Lead	L	0.3937	in
efficiency	e	0.9	

26.50898 N-m

speed		
V	10.33426	in/s
Vm	1574.944	RPM

	Load inertia		
	m	300	lb
	g	386	in/s
	ρ (steel)	0.28	lb/in^3
inrtia of load	Jl	0.003051	lb-in.-sec^2
inertia od screw	Jls	0.021035	lb-in.-sec^2
	J=Jl+Jls	0.024086	lb-in.-sec^2
acc. Time	t	0.2	sec
angular acc.	ω	824.6387	rad/sec^2
acc. Torque	Ta	19.86228	lb.in

Total Torque 254.4865 lb.in

Torque Calculations:

$$T = F_T \bullet \frac{L}{2\pi e}$$

where: F_T = Total Force (lbs)
L = Lead (inches)
e = efficiency (no units, use 0.9 for Ball screws assemblies.)

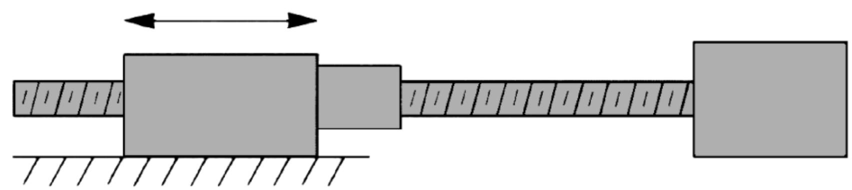

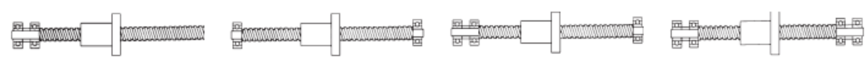

$$\text{rpm} = \frac{\text{linear velocity (in/min)}}{\text{lead (in/rev)}} \qquad (4)$$

Maximum Speed:

$$C_s = F\,(4.76 \times 10^6)\,\frac{d}{L^2} \qquad (5)$$

where:
C_s = critical speed (rpm)
d = root diameter of screw (inches)
L = length between supports (inches)
F = end support factor (see diagram)
case **A.**: 0.36
case **B.**: 1.00
case **C.**: 1.47
case **D.**: 2.23

Maximum Load

$$P = F\,(14.03 \times 10^6)\,\frac{d^4}{L^2} \qquad (6)$$

where:
P = maximum load (lbs) (critical load)
d = root diameter of screw (inches)
L = maximum distance between nut and load carrying bearing
F = end support factor (see diagram)
case **A.**: 0.25
case **B.**: 1.00
case **C.**: 2.00
case **D.**: 4.00

Appendix D

Nook Ball Screw

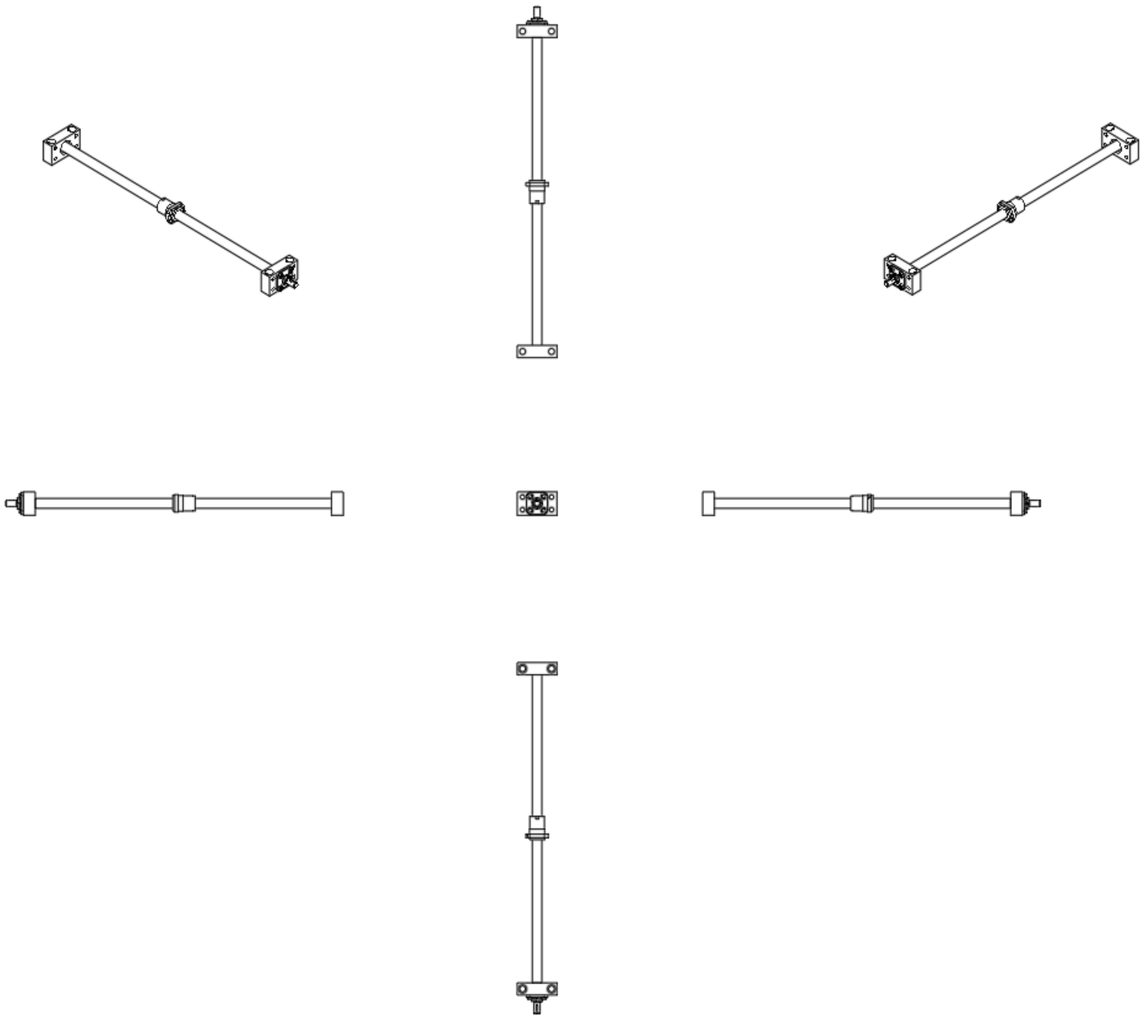

Product Specification Sheet

MBN40x10R-4FW

Call 800-321-7800 or visit us online at www.nookindustries.com to configure and order your MBN40x10R-4FW today!

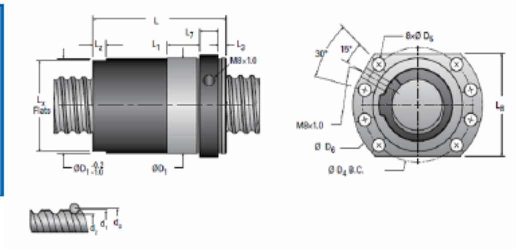

Product Info	
Nominal Rod Diameter [mm]	40
Material	Alloy
Thread Direction	RH
Details	
Lead [mm]	10
Active Turns	4
Nominal Ball Dia. [mm]	7.144
Screw Weight [kg/m]	8.65
Nut Weight [kg]	1.31
Lube Hole Locaton	-
End Code for Types 1,2, and 3	30
End Code for Types 4	19
End Code for Types 5	25
End Code for Types 6	30
End Code for Types 7	30
Performance Specifications	
Dynamic Load Ca [N]	56770
Static Load [N]	116070
Linear Speed (Based on DN Values) [mm/min]	16700
Screw Dimensions	
d0 [mm]	42.1
d1 [mm]	40.00
d2 [mm]	34.81
Nut Dimensions	
D1 (g6) [mm]	63
L [mm]	93
L1 [mm]	20
Lx [mm]	60
Lz [mm]	10
L3 (min) [mm]	8.5
L7 [mm]	14
L8 [mm]	70
D4 [mm]	78
D5 [mm]	8 × 9
D6 [mm]	93

Appendix E

MATLAB Code

```
    clear all;
    clc;

    %dont read header

    %open data file
    fid = fopen('h2d5D1T2,2.csv');

    %read data from csv
    readData = textscan(fid, '%f %f %f %f
%f','Headerlines',1,'delimiter',',');

    %extract data from read data
    xData = readData{1,1}(:,1);
    LB = readData{1,2}(:,1);
    RT = readData{1,3}(:,1);
    RB = readData{1,4}(:,1);
    LT = readData{1,5}(:,1);

    f(:,1) = 0;

    %finding minimum
    % [fmin,imin] = min(LB);
    % xmin = xData(imin);



    %plot Data
    f1 = figure(1);
    cla;hold on;grid on;
    p1=plot(xData,LB,'k-');
    p2=plot(xData,RT,'r-');
    p3=plot(xData,RB,'b-');
    p4=plot(xData,LT,'g-');
    title('all bouy motion');
    xlabel('Time');ylabel('water surface motion');

    %% LEFT BOTTOM
    %finding the slope for LB
    for i=1 : length(LB)-1
    f(i) = (LB(i+1)-LB(i))/(xData(i+1)-xData(i));
    end
    %
    t=1;
    for i=1 : length(LB)-2
        if f(i)*f(i+1)<0
        plot(xData(i+1),LB(i+1),'*');
        g(t)=LB(i+1);
        t=t+1;
```

```
    end
if f(i)==0
    plot(xData(i),LB(i),'*');
    g(t)=LB(i);
    t=t+1;
end
end
%finding local max and min
t=1;
p=1;
for j=1:length(g)
    if g(j)>mean(g)
        locmaxLB(t)=g(j);
        t=t+1;
    else
        locminLB(p)=g(j);
        p=p+1;
    end
end
%% LEFT TOP
%finding the slope for LT
for i=1 : length(LT)-1
f(i) = (LT(i+1)-LT(i))/(xData(i+1)-xData(i));

end

tt=1;
for i=1 : length(LT)-2
    if f(i)*f(i+1)<0
    plot(xData(i+1),LT(i+1),'*');
    g(tt)=LT(i+1);
    tt=tt+1;
    end
if f(i)==0
    plot(xData(i),LT(i),'*');
    g(tt)=LT(i);
    tt=tt+1;
end
end
tt=1;
pp=1;
for j=1:length(g)
    if g(j)>mean(g)
        locmaxLT(tt)=g(j);
        tt=tt+1;
    else
        locminLT(pp)=g(j);
        pp=pp+1;
    end
end
%%

x1 = min(length(locmaxLT),length(locminLT));
x2 = min(length(locmaxLB),length(locminLB));
x = min(x1,x2);

locLTsubtract = locmaxLT(1:min(x))-locminLT(1:min(x))
```

```
locLBsubtract = locmaxLB(1:min(x))-locminLB(1:min(x))

locdivL = locLBsubtract./locLTsubtract;

%%
% f2 = figure(2);hold on;grid on;
% plot(xData,RT,'r-');
% plot(xData,RB,'b-');


%% RIGHT BOTTOM
%finding the slope for LB
for i=1 : length(RB)-1
f(i) = (RB(i+1)-RB(i))/(xData(i+1)-xData(i));

end

t=1;
for i=1 : length(RB)-2
    if f(i)*f(i+1)<0
    plot(xData(i+1),RB(i+1),'*');
    g(t)=RB(i+1);
    t=t+1;
    end
if f(i)==0
    plot(xData(i),RB(i),'*');
    g(t)=RB(i);
    t=t+1;
end
end
t=1;
p=1;
for j=1:length(g)
    if g(j)>mean(g)
        locmaxRB(t)=g(j);
        t=t+1;
    else
        locminRB(p)=g(j);
        p=p+1;
    end
end
%% RIGHT TOP
%finding the slope for LT
for i=1 : length(RT)-1
f(i) = (RT(i+1)-RT(i))/(xData(i+1)-xData(i));

end

tt=1;
for i=1 : length(RT)-2
    if f(i)*f(i+1)<0
    plot(xData(i+1),RT(i+1),'*');
    g(tt)=RT(i+1);
    tt=tt+1;
    end
if f(i)==0
    plot(xData(i),RT(i),'*');
```

```
    g(tt)=RT(i);
    tt=tt+1;
end
end
tt=1;
pp=1;
for j=1:length(g)
    if g(j)>mean(g)
        locmaxRT(tt)=g(j);
        tt=tt+1;
    else
        locminRT(pp)=g(j);
        pp=pp+1;
    end
end
%%


x1 = min(length(locmaxRT),length(locminRT));
x2 = min(length(locmaxRB),length(locminRB));
x = min(x1,x2);

locRTsubtract = locmaxRT(1:min(x))-locminRT(1:min(x))
locRBsubtract = locmaxRB(1:min(x))-locminRB(1:min(x))

locdivR = locRBsubtract./locRTsubtract
locdivL = locLBsubtract./locLTsubtract

mean(locRBsubtract);
meanL = mean(locdivL)
meanR = mean(locdivR)
legend([p1 p2 p3 p4],'LB','RT','RB','LT');
mean(locRTsubtract)
mean(locLTsubtract)
```

Appendix F

Flow3D Code

```
 Title
 This is a sample input file

&xput
   remark='!! Remarks beginning with "!! " are automatically added and
removed by FLOW-3D.',
   remark='!! Do not begin any user added remarks with with "!! ". They
will be removed',
   twfin=30,
   itb=1,
   ifenrg=0,
   ifvisc=1,
   ifvis=4,
   imobs=1,
   impmob=1,
   imphtc=0,
   ifdynconv=1,
   iphchg=3,
   gz=-32.2,
   iclid=1,
   ipdis=1,
   idpth=1,
   iorder=3,
/

&limits
/

&props
   units='eng',
   tunits='f',
   munits='slug',
   lunits='ft',
   timunits='s',
   cunits='coul',
   gamma=1,
   pcav=0,
   mu1=2.0885434e-05,
   cangle=-90,
   pgasmp=0,
   fluid1='Water at 20 C',
   muc1=0,
   muctst=0.001,
   mutmp2=32,
   cv1=25008.1722282,
```

```
   tl1=32.18,
   ts1=32,
   clht1=3.607240805e+06,
   cvs1=12557.90571,
   thcs1=0.2766994834,
   rhofs=1.7792737151,
   tsdrg=1,
   fscr=1,
   fsco=0,
   rhof=1.9403203,
   sigma=0.005002088918,
   yieldt1=0,
   mus=0,
   thc1=0.07457769372,
   yield1=-0.020885434,
   ipgauge=1,
/

&scalar
/

&CHM
/

&BCDATA
   remark='!! Boundary condition X Min',
   ibct(1)=1,
   iwavebc(1)=1,
   waveh(1)=6,
   inwave(1)=1,
   ihpbct(1)=1,
   flhtbct(1, 1)=6,
   waveamp(1, 1)=0.5,
   waveper(1, 1)=2,
   ihtbct(1)=0,

   remark='!! Boundary condition X Max',
   ibct(2)=1,
   ihpbct(2)=1,
   fbct(1, 2)=0,
   flhtbct(1, 2)=6,
   ihtbct(2)=0,

   remark='!! Boundary condition Y Min',
   ihtbct(3)=0,

   remark='!! Boundary condition Y Max',
   ihtbct(4)=0,

   remark='!! Boundary condition Z Min',
   ibct(5)=2,
   ihtbct(5)=0,
```

```
   remark='!! Boundary condition Z Max',
   ibct(6)=5,
   pbct(1, 6)=2116,
   fbct(1, 6)=0,
   ihtbct(6)=0,
/

&MESH
   MeshName='Mesh block 1',
   size=0.2,

   px(1)=-5,
   px(2)=18,

   py(1)=-2.5,
   py(2)=0.5,
   py(3)=3.5,

   pz(1)=0,
   pz(2)=12,
   if_mesh_enabled=1,
/

&BCDATA
   remark='!! Boundary condition X Min',
   iwavebc(1)=1,
   waveh(1)=3,
   inwave(1)=1,
   ihpbct(1)=1,
   flhtbct(1, 1)=3,
   waveamp(1, 1)=0.5,
   waveper(1, 1)=2,
   ihtbct(1)=0,

   remark='!! Boundary condition X Max',
   ihtbct(2)=0,

   remark='!! Boundary condition Y Min',
   ihtbct(3)=0,

   remark='!! Boundary condition Y Max',
   ihtbct(4)=0,

   remark='!! Boundary condition Z Min',
   ibct(5)=2,
   ihtbct(5)=0,

   remark='!! Boundary condition Z Max',
   ibct(6)=5,
   pbct(1, 6)=2116,
   fbct(1, 6)=0,
   ihtbct(6)=0,
/
```

```
&MESH
   MeshName='Mesh block 2',
   size=0.1,

   px(1)=-2,
   px(2)=17,

   py(1)=-0.7,
   py(2)=1.7,

   pz(1)=0,
   pz(2)=12,
/

&BCDATA
   remark='!! Boundary condition X Min',
   iwavebc(1)=1,
   waveh(1)=3,
   inwave(1)=1,
   ihpbct(1)=1,
   flhtbct(1, 1)=3,
   waveamp(1, 1)=0.5,
   waveper(1, 1)=2,
   ihtbct(1)=0,

   remark='!! Boundary condition X Max',
   ibct(2)=8,
   iobctp(2)=1,
   ihtbct(2)=0,

   remark='!! Boundary condition Y Min',
   ihtbct(3)=0,

   remark='!! Boundary condition Y Max',
   ihtbct(4)=0,

   remark='!! Boundary condition Z Min',
   ibct(5)=2,
   ihtbct(5)=0,

   remark='!! Boundary condition Z Max',
   ibct(6)=5,
   pbct(1, 6)=2116,
   fbct(1, 6)=0,
   ihtbct(6)=0,
/

&MESH
   MeshName='Mesh block 3',
   size=0.4,

   px(1)=18,
```

```
   px(2)=66,

   py(1)=-2.5,
   py(2)=3.5,

   pz(1)=0,
   pz(2)=12,
   if_mesh_enabled=1,
/

&BCDATA
   remark='!! Boundary condition X Min',
   ibct(1)=10,
   iwavebc(1)=1,
   waveh(1)=10,
   inwave(1)=1,
   lnwave(1)=29.87,
   hnwave(1)=1,
   ihpbct(1)=1,
   flhtbct(1, 1)=10,
   waveamp(1, 1)=0.5,
   waveper(1, 1)=2.46,
   ihtbct(1)=0,

   remark='!! Boundary condition X Max',
   ihtbct(2)=0,

   remark='!! Boundary condition Y Min',
   ihtbct(3)=0,

   remark='!! Boundary condition Y Max',
   ihtbct(4)=0,

   remark='!! Boundary condition Z Min',
   ibct(5)=2,
   ihtbct(5)=0,

   remark='!! Boundary condition Z Max',
   ibct(6)=5,
   pbct(1, 6)=2116,
   fbct(1, 6)=0,
   ihtbct(6)=0,
/

&MESH
   MeshName='Mesh block 4',
   ntotal=1000,
   size=0.4,

   px(1)=-25,
   px(2)=-5,

   py(1)=-2.5,
```

```
   py(2)=3.5,

   pz(1)=0,
   pz(2)=12,
   if_mesh_enabled=1,
/

&obs
   nobs=5,

   remark='!! Component 1',
   obsid(1)='LB',

   remark='!! Subcomponent 1',
   iob(1)=1,
   subcmpid(1)='Subcomponent 1',
   igen(1)=3,
   fstl(1)='bouyLB.stl',
   rhosub(1)=0.9,
   trnx(1)=0,
   trny(1)=0.3,
   trnz(1)=1.3,
   if_sub_pin(1)=0,

   remark='!! Component 1 properties',
   imo(1)=4,
   ilthobs(1)=0,
   dxmcmin(1)=0,
   dymcmin(1)=0,
   dxmcmax(1)=0,
   dymcmax(1)=0,
   rhomvb(1)=0.9,
   tjmvb(1, 2, 1)=0,
   tjmvb(1, 3, 1)=0,
   tjmvb(1, 3, 2)=0,
   iumcal(1)=0,
   ivmcal(1)=0,
   iomxcal(1)=0,
   iomycal(1)=0,
   iomzcal(1)=0,
   omxtobs(1, 1)=0,
   omytobs(1, 1)=0,
   omztobs(1, 1)=0,
   utobs(1, 1)=0,
   vtobs(1, 1)=0,
   wtobs(1, 1)=0,

   remark='!! Component 2',
   obsid(2)='RT',
   ifCompEnabled(2)=1,

   remark='!! Subcomponent 2',
   iob(2)=2,
```

```
subcmpid(2)='Subcomponent 2',
igen(2)=3,
fstl(2)='bouyRT.stl',
rhosub(2)=0.9,
trnx(2)=5.7,
trny(2)=0.3,
trnz(2)=7,
if_sub_pin(2)=0,

remark='!! Component 2 properties',
imo(2)=4,
ilthobs(2)=0,
dxmcmin(2)=0,
dymcmin(2)=0,
dzmcmin(2)=-1.7,
dxmcmax(2)=0,
dymcmax(2)=0,
dzmcmax(2)=1.8,
rhomvb(2)=0.9,
tjmvb(2, 2, 1)=0,
tjmvb(2, 3, 1)=0,
tjmvb(2, 3, 2)=0,
iumcal(2)=0,
ivmcal(2)=0,
iomxcal(2)=0,
iomycal(2)=0,
iomzcal(2)=0,
omxtobs(1, 2)=0,
omytobs(1, 2)=0,
omztobs(1, 2)=0,
utobs(1, 2)=0,
vtobs(1, 2)=0,
wtobs(1, 2)=0,

remark='!! Component 3',
obsid(3)='RB',

remark='!! Subcomponent 3',
iob(3)=3,
subcmpid(3)='Subcomponent 3',
igen(3)=3,
fstl(3)='bouyRB.stl',
rhosub(3)=0.9,
trnx(3)=5.7,
trny(3)=0.3,
trnz(3)=1.3,
if_sub_pin(3)=0,

remark='!! Component 3 properties',
imo(3)=4,
ilthobs(3)=0,
dxmcmin(3)=0,
dymcmin(3)=0,
```

```
dxmcmax(3)=0,
dymcmax(3)=0,
rhomvb(3)=0.9,
tjmvb(3, 2, 1)=0,
tjmvb(3, 3, 1)=0,
tjmvb(3, 3, 2)=0,
iumcal(3)=0,
ivmcal(3)=0,
iomxcal(3)=0,
iomycal(3)=0,
iomzcal(3)=0,
omxtobs(1, 3)=0,
omytobs(1, 3)=0,
omztobs(1, 3)=0,
utobs(1, 3)=0,
vtobs(1, 3)=0,
wtobs(1, 3)=0,

remark='!! Component 4',
obsid(4)='LT',
ifCompEnabled(4)=1,

remark='!! Subcomponent 4',
iob(4)=4,
subcmpid(4)='Subcomponent 4',
igen(4)=3,
fstl(4)='bouyLT.stl',
rhosub(4)=0.9,
trnx(4)=0,
trny(4)=0.3,
trnz(4)=7,
if_sub_pin(4)=0,

remark='!! Component 4 properties',
imo(4)=4,
ilthobs(4)=0,
dxmcmin(4)=0,
dymcmin(4)=0,
dzmcmin(4)=-1.7,
dxmcmax(4)=0,
dymcmax(4)=0,
dzmcmax(4)=1.8,
rhomvb(4)=0.9,
tjmvb(4, 2, 1)=0,
tjmvb(4, 3, 1)=0,
tjmvb(4, 3, 2)=0,
iumcal(4)=0,
ivmcal(4)=0,
iomxcal(4)=0,
iomycal(4)=0,
iomzcal(4)=0,
omxtobs(1, 4)=0,
omytobs(1, 4)=0,
```

```
   omztobs(1, 4)=0,
   utobs(1, 4)=0,
   vtobs(1, 4)=0,
   wtobs(1, 4)=0,

   remark='!! Component 5',
   ifob(5)=10,
   obsid(5)='Component 5',

   remark='!! Subcomponent 5',
   iob(5)=5,
   subcmpid(5)='Subcomponent 5',
   xl(5)=36,
   xh(5)=66,
   yl(5)=-1.5,
   yh(5)=2.5,
   zl(5)=0,
   zh(5)=10,
   if_sub_pin(5)=0,

   remark='!! Component 5 properties',
   ilthobs(5)=0,
   xspng(5)=47,
   yspng(5)=2,
   zspng(5)=0,
   xdspng(5)=1,
   ydspng(5)=1,
   zdspng(5)=1,

   remark='!! Component common parameters',
   avrck=-3.1,
/

&fl
   nfls=1,

   remark='!! FluidRegion 1',
   fluidRegionName(1)='Region 1',
   fioh(1)=0,
   ifdis(1)=-1,
   ftrnx(1)=-10.5,
   ftrny(1)=-25.7,
   ftrnz(1)=0,
   ffstl(1)='thesis frawing 2 inside.stl',

   remark='!! Region Pointer common parameters',
   pvoid=2597,
   flht=10,
   iflinittyp=1,
/

&bf
   nbafs=1,
```

```
   remark='!! Baffle 1',
   fptitl(1)='Baffle 2',
   baffleRegionName(1)='Region 1',
   ibaf(1)=1,
   btrnx(1)=-10.5,
   btrny(1)=-25.7,
   istlbf(1)=1,
   fstlbf(1)='thesis frawing 2.stl',
/

&motn
/

&grafic
   anmtyp(1)='dpth',
   anmtyp(2)='p',
/

&RENDERSPACE
   iff3d(1)=1,
   iff3d(3)=1,
/

&HEADER
   project='Copy of OWC- h=4 - D=2 - d=7_ Sept',
   version='double',
   nprocs=0,
   runser=0,
   use_parallel_token=0,
/

&parts
/

&DETAILS
   f3d_product_name='FLOW-3D',
   f3d_version_number='12.0.1',
   created='2020 Sep 24 15:20',
   modified='2020 Sep 29 09:51',
/
   Documentation: general comments, background, expectations, etc.
```

Appendix G

Tests Results for Styrofoam

NO#	d (cm)	T (sec)	L/2 (cm)	H (cm)	d/L	H/L	d/gT^2	H_{inside} (cm)	Conversion Rate
1	26.5	1.17	86	8.5	0.154	0.198	0.020	2.7	31.8%
2	26.5	1.05	80	4.0	0.166	0.100	0.025	1.5	37.5%
3	26.5	1.22	88	3.7	0.151	0.084	0.018	1.5	40.5%
4	26.5	1.61	126	2.0	0.105	0.032	0.010	1.4	70.0%
5	27.5	1.50	96	1.4	0.143	0.029	0.012	1.1	78.6%
6	27.5	1.63	127	1.5	0.108	0.024	0.011	1.2	80.0%
7	27.5	1.00	70	3.0	0.196	0.086	0.028	0.9	30.0%
8	28.5	1.00	70	3.5	0.204	0.100	0.029	1.0	28.6%
9	28.5	1.73	119	1.4	0.120	0.024	0.010	1.0	71.4%
10	28.5	1.43	119	2.1	0.120	0.035	0.014	1.0	47.6%
11	29.5	1.43	119	2.9	0.124	0.049	0.015	1.5	51.7%
12	29.5	1.12	100	4.4	0.148	0.088	0.024	1.4	31.8%
13	29.5	1.74	135	1.8	0.109	0.027	0.010	1.0	55.6%
14	30.5	1.86	133	1.6	0.115	0.024	0.009	1.3	81.3%
15	30.5	1.24	110	3.5	0.139	0.064	0.020	1.2	34.3%
16	30.5	1.93	147	1.8	0.104	0.024	0.008	1.2	66.7%
17	30.5	2.01	176	3.4	0.087	0.039	0.008	2.1	61.8%
18	24.5	1.42	121	2.7	0.101	0.045	0.012	1.5	55.6%
19	24.5	1.74	141	1.4	0.087	0.020	0.008	1.1	78.6%
20	24.5	1.10	86	1.5	0.142	0.035	0.021	0.6	40.0%
21	25.5	2.02	130	1.4	0.098	0.022	0.006	1.0	71.4%
22	25.5	1.43	121	1.6	0.105	0.026	0.013	1.1	68.8%
23	25.5	1.14	96	1.8	0.133	0.038	0.020	0.7	38.9%
24	26.5	1.14	96	1.9	0.138	0.040	0.021	0.8	42.1%

NO#	d (cm)	T (sec)	L/2 (cm)	H (cm)	d/L	H/L	d/gT^2	H_{inside} (cm)	Conversion Rate
25	26.5	1.41	118	1.5	0.112	0.025	0.014	1.0	66.7%
26	26.5	1.72	133	1.1	0.100	0.017	0.009	0.9	81.8%
27	27.5	1.71	133	1.1	0.103	0.017	0.010	0.9	81.8%
28	27.5	1.42	98	1.9	0.140	0.039	0.014	1.3	68.4%
29	27.5	1.05	73	3.1	0.188	0.085	0.025	0.9	29.0%
30	28.5	1.65	111	2.1	0.128	0.038	0.011	1.4	66.7%
31	28.5	1.33	93	2.6	0.153	0.056	0.016	1.1	42.3%
32	28.5	1.12	85	2.4	0.168	0.056	0.023	0.9	37.5%
33	29.5	1.12	85	5.8	0.174	0.136	0.024	2.0	34.5%
34	29.5	1.22	80	10.0	0.184	0.250	0.020	3.6	36.0%
35	29.5	1.59	119	2.6	0.124	0.044	0.012	1.4	53.8%
36	30.5	1.59	119	1.8	0.128	0.030	0.012	1.2	66.7%
37	30.5	1.22	100	3.3	0.153	0.066	0.021	1.2	36.4%
38	30.5	1.22	107	2.2	0.143	0.041	0.021	1.8	81.8%
39	30.5	1.62	107	2.1	0.143	0.039	0.012	2.0	95.2%
40	30.5	2.03	154	4.6	0.099	0.060	0.008	4.5	97.8%
41	30.5	1.58	119	3.7	0.128	0.062	0.012	3.0	81.1%
42	30.0	2.11	160	3.0	0.094	0.038	0.007	2.1	70.0%
43	30.0	1.65	130	1.8	0.115	0.028	0.011	1.5	83.3%
44	30.0	1.37	103	2.6	0.146	0.050	0.016	1.5	57.7%
45	31.0	1.60	122	6.1	0.127	0.100	0.012	3.8	62.3%
46	31.0	1.86	138	1.8	0.112	0.026	0.009	1.7	94.4%
47	31.5	2.00	152	5.3	0.104	0.070	0.008	4.9	92.5%
48	31.5	1.60	147	1.9	0.107	0.026	0.013	1.5	78.9%